S-FACTOR MEASUREMENT OF THE ^{2}H$(\alpha,\gamma)^6$Li REACTION AT ENERGIES RELEVANT FOR BIG-BANG NUCLEOSYNTHESIS

Michael Anders

WISSENSCHAFTLICH-
TECHNISCHE BERICHTE

HZDR

HELMHOLTZ
ZENTRUM DRESDEN
ROSSENDORF

Michael Anders

S-FACTOR MEASUREMENT OF THE ^{2}H(α,γ)^{6}Li REACTION AT ENERGIES RELEVANT FOR BIG-BANG NUCLEOSYNTHESIS

HZDR

HELMHOLTZ
ZENTRUM DRESDEN
ROSSENDORF

S-factor measurement of the $^2\text{H}(\alpha,\gamma)^6\text{Li}$ reaction at energies relevant for Big-Bang nucleosynthesis

vorgelegt von

Michael Anders
geboren am 21. 08. 1983 in Großröhrsdorf

Institut für Kern- und Teilchenphysik
Technische Universität Dresden

und

Institut für Strahlenphysik
Helmholtz-Zentrum Dresden-Rossendorf

Eingereicht am 28. 06. 2013 und verteidigt am 30. 09. 2013.

Kurzdarstellung

Seit etwa 20 Jahren wird in mehreren alten, metallarmen Sternen im Halo unserer Galaxie auch ^{6}Li gefunden. Der Anteil an ^{6}Li ist von der Metallizität der Sterne weitgehend unabhängig und damit offenbar primordialen Ursprungs. Der beobachtete Wert überschreitet die Vorhersagen des Standardmodells der Urknall-Nukleosynthese allerdings um den Faktor 500. Im relevanten Energiebereich gab es für die bestimmende Erzeugungsreaktion ^{2}H$(\alpha,\gamma)^6$Li bislang keine direkt gemessenen S-Faktoren, und die verschiedenen theoretischen Abschätzungen haben eine Unsicherheit von bis zu zwei Größenordnungen. Der sehr kleine Wirkungsquerschnitt im Picobarn-Bereich ist mit einem Deuterium-Gastarget am LUNA-Beschleuniger (Laboratory for Underground Nuclear Astrophysics) gemessen worden, der sich untertage in den Laboratori Nazionali del Gran Sasso in Italien befindet. Dabei trat ein strahlinduzierter, neutronenflussbedingter Untergrund im γ-Detektor auf, der tiefgehend analysiert und geeignet abgezogen werden musste, um das schwache Signal der Reaktion herauszuarbeiten. Dazu wurde ein Verfahren zur Parametrisierung des Compton-Untergrundes entwickelt. Die gewonnenen Ergebnisse sind ein Beitrag zur Diskussion über die Belastbarkeit der bisherigen ^{6}Li-Beobachtungen, und für die Frage, ob neue Physik in das Standardmodell der Urknall-Nukleosynthese einbezogen werden muss.

Abstract

For about 20 years now, observations of ^{6}Li in several old metal-poor stars inside the halo of our galaxy have been reported, which are largely independent of the stars' metallicity, and which point to a possible primordial origin. The observations exceed the predictions of the Standard Big-Bang Nucleosynthesis model by a factor of 500. In the relevant energy range, no directly measured S-factors were available yet for the main production reaction ^{2}H$(\alpha,\gamma)^6$Li, while different theoretical estimations have an uncertainty of up to two orders of magnitude. The very small cross section in the picobarn range has been measured with a deuterium gas target at the LUNA accelerator (Laboratory for Underground Nuclear Astrophysics), located deep underground inside Laboratori Nazionali del Gran Sasso in Italy. A beam-induced, neutron-caused background in the γ-detector occurred which had to be analyzed carefully and subtracted in an appropriate way, to finally infer the weak signal of the reaction. For this purpose, a method to parameterize the Compton background has been developed. The results are a contribution to the discussion about the accuracy of the recent ^{6}Li observations, and to the question if it is necessary to include new physics into the Standard Big-Bang Nucleosynthesis model.

Parts of the present data in sections 3.2 - 3.4 as well as in sections 4.1 - 4.4 have already been published in a peer-reviewed journal:

Contents

List of Figures

List of Tables

1. Introduction

Lithium has always been a rare element.

Its abundance in the Earth's crust is only seven parts per million [1]. Lithium is widely distributed on Earth, but rarely enriched in minerals, and only a few and non-abundant deposits are known. The major part of the annual lithium production is extracted from salt lakes with a lithium content of up to 1 %. The name of the element is derived from the greek word "$\lambda\iota\theta o\varsigma$" (stone) and is reminiscent of its discovery among Swedish minerals in 1817.

However, the mentioned lithium concentrations, even of 7 ppm, can be regarded as strongly enriched, if one considers the abundance of lithium in the pre-galactic interstellar matter after Big-Bang, and before the first stars and galaxies were born. The Standard Big-Bang Nucleosynthesis (SBBN) model predicts, after the decay of ^{7}Be, a very low final ^{7}Li abundance level, being more than nine orders of magnitude below the abundance of hydrogen [2]. The predicted abundance of ^{6}Li is again about four orders of magnitude lower - at a level, where the detection in stars is impossible, even if it would have survived there until today. Nowadays, on Earth, natural lithium contains 7.5 % of ^{6}Li [1]. Something has changed the abundance pattern during the past billions of years, there must have been a chemical evolution of lithium.

Since 1982, when Monique and François Spite [3] discovered a constant ^{7}Li abundance in old metal-poor halo stars close to the center of our galaxy, the "lithium problem" has triggered many efforts by observers, theoreticians and experimentalists. The "Spite plateau" points to a primordial origin of the observed ^{7}Li, but measured and predicted abundances are in disagreement. In order to deliver credible predictions, Big-Bang nucleosynthesis models need reliable and precise nuclear data. The Big-Bang nucleosynthesis network contains a manageable number of nuclear reactions, and the only remaining input parameter, the baryon-to-photon ratio, has been measured in the past decade with high precision in observations of the cosmic microwave background. With this input, the SBBN model is very successful in predicting the primordial abundances of ^{2}H and ^{4}He (e.g. [2]). A wrong prediction by a factor of 3 in the case of ^{7}Li is a strong drawback. Cross section data of all related nuclear reactions are known for the relevant energies, with a sufficient precision to rule out remaining uncertainties as a reason for the discrepancies [2].

The disagreement seems to be even worse for ^{6}Li (by a factor of 500), which has been detected for the first time already 20 years ago in individual members

of the same group of stars [4], although updated analysis approaches could change the picture here. The largely metallicity-independent ^{6}Li abundance points to a primordial origin of this isotope as well. The main production during Big-Bang nucleosynthesis occurred via the ^{2}H(α,γ)^{6}Li reaction [5]. In the interesting energy range, no directly measured cross-sections are available: The values are too small for a direct measurement overground. However, direct measurements at higher energy have been undertaken as early as 1981, with the object of answering the question whether all cosmic ^{6}Li has been produced by cosmic-ray interactions, or if there is at least a partial primordial origin [6]. This question remains until today. All indirectly measured data and extrapolations to lower energies carry inevitable uncertainties due to the choice of theoretical models which have to be included in the data analysis [5]. This will be discussed in chapter 2.

Lithium in the Universe remains an exciting and fruitful field of research, and even more, since non-standard physics and exotic scenarious have been proposed to solve the "lithium problems" [7]. However, the production and depletion of lithium isotopes in stars, in explosive processes or by cosmic ray interactions is still under investigation. Research on nuclear reactions participating in the nucleosynthesis of lithium is part of these efforts. It became clear that, due to the low reaction rates in the relevant energy range, direct measurements of several reactions can be carried out only at an underground accelerator facility, well shielded from cosmic rays and other radiation sources. This has been the motivation to study the ^{2}H(α,γ)^{6}Li reaction deep underground at the LUNA2 accelerator, located inside Laboratori Nazionali del Gran Sasso in Italy. The basic principle of the measurement and the setup are described in chapter 3.

In the present study, several ancillary conditions and observed effects were new compared to previous LUNA experiments: Low target gas pressures and light interacting nuclei resulted in a very low beam energy loss inside the target - which is an advantage. The beam-induced neutron flux required different shielding measures and data analysis methods than usual for LUNA experiments (described in chapter 4). The main challenge was to understand and subtract the neutron-induced background in the γ-detector. Two directly measured (and two derived) S-factor values in the relevant energy range can be provided (see chapter 5) and are briefly discussed in chapter 6.

Lithium as an important material for high-capacity batteries may power electric mobility in the future. Especially ^{6}Li could become important for nuclear fusion power plants, as tritium can be produced via the ^{6}Li(n,^{3}H)^{4}He process. Its origin is still one of the most prominent questions of Nuclear Astrophysics. The answers to this question may open another door to new physics, and to a largely changed picture of the origin of our Universe. The results presented in this PhD thesis are one step towards a clarification.

2. Lithium in the Universe

In this chapter, the various processes of lithium production and depletion are illustrated, with a focus on the minor isotope ^{6}Li. The motivation to study the ^{2}H$(\alpha,\gamma)^6$Li reaction is exposed, and the nuclear physics behind is discussed.

2.1. Big-Bang nucleosynthesis

Only a few observables are still available today to infer information about the early phases of our Universe. The cosmic microwave background radiation is one of them and the most ancient signal ever detected [8]. It allows to look back to a time of about 380.000 years after Big Bang, corresponding to a temperature of 3000 K, when the photon energy became too low to disintegrate hydrogen atoms to protons and electrons. The astounding homogeneity of this radiation reveals the homogeneous distribution of the interstellar matter at this time.

A plasma temperature of 3000 K is by far to low to allow nucleosynthesis processes, which started again only when the first stars had evolved. The baryonic matter from which these stars were formed had been generated much earlier, during the first minutes of the Universe, at temperatures in the order of Gigakelvin.

Big-Bang nucleosynthesis is another observable and is believed to be the earliest reliable probe of the Universe [7]. The Standard Big-Bang Nucleosynthesis (SBBN) model is able to predict the primordial abundances of several light nuclides in very good agreement with the observations. This has been possible only with the precise knowledge of the baryon-to-photon ratio and other cosmological constants, one of the most important results of the observation of the cosmic microwave background. The success of the SBBN model is a strong hint that, during Big-Bang nucleosynthesis, the Universe was governed by the same physical laws of nature as today [9], and that the content of particles has been at least similar. Slight deviations from that would already cause different abundance predictions, so the agreement or disagreement between the observed and predicted abundances constrain the physics of the Universe during Big-Bang nucleosynthesis and especially non-standard scenarios.

In the hot, dense and expanding Universe, baryons and antibaryons were formed out of the quark-gluon plasma and annihilated. The asymmetry of baryogenesis caused a minimal excess of baryons which were left over, after the Universe became too cold to allow the production of baryons from photons. In the hot plasma, neutrons and protons remained and were converted into each other by weak interactions, until

the necessary temperature to allow $p + e^- \rightarrow n + \nu_e$, $Q = -780\,\text{keV}$ was underrun. At this time, when the age of the Universe was about one second, the proton-to-neutron ratio froze out to 6:1, and the remaining mixture constituted the basic material for Big-Bang nucleosynthesis. A process which began at this time and lasted about three minutes (see figure 2.1), and which can be regarded as a transition from a proton-neutron equilibrium to a Universe with a significant presence of helium [9], and with some traces of deuterium, lithium and beryllium (which decayed to lithium later).
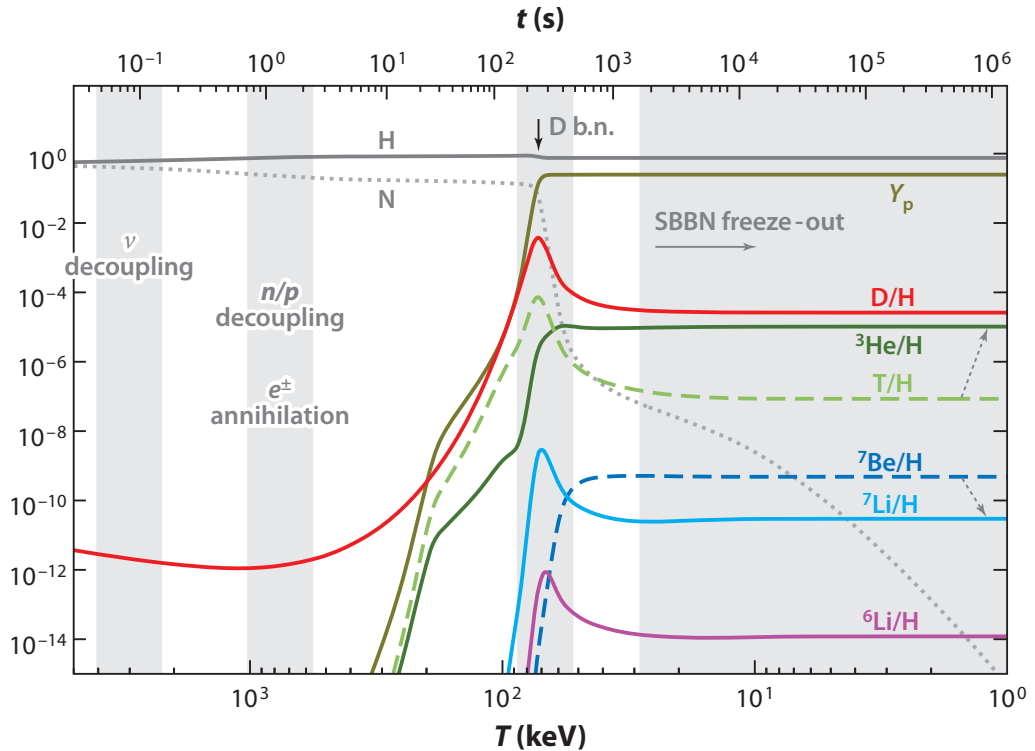
Figure 2.1.: Standard Big-Bang nucleosynthesis of the most abundant primordial nuclei, taken from [9].

The SBBN model relies on specific assumptions that are compiled e.g. in [9]:

- Following the cosmological principle, the Universe was spatially homogeneous and isotropic. It is furthermore assumed to have been dominated by radiation, and that the space-time geometry has been flat.

- At the time of the proton-neutron equilibrium, both species were equally abundant, in thermal equilibrium and distributed in perfect spatial homogeneity.

- The particle content and the interactions are given by the Standard Model. The properties of particles and nuclei (e.g. their masses, couplings, lifetimes) are the same as today.

- The energy density is dominated by photons and neutrinos. The baryon-to-photon ratio provides a measure of the nucleon content of the Universe during Big-Bang nucleosynthesis.

The evolution of nuclide abundances can be mathematically described by a set of coupled, first-order differential Boltzmann equations containing a temperature-dependent Hubble expansion rate [9]. This system of equations can be solved numerically using well-developed integration codes. This allows to calculate final abundance values after the freeze-out of Big-Bang nucleosynthesis.

Another input to the SBBN model is the knowlegde of the underlying network of nuclear reactions and related reaction data. In general, with only a few exceptions, the required data are abundantly available and of sufficient precision, which allows to provide very accurate predictions of the final SBBN abundances. Using the baryon-to-photon ratio provided by WMAP 2011, the observed primordial abundances of light nuclei are compared to the predicted ones in a recent publication [2]. For ^{2}H and ^{4}He, the agreement is impressive. In case of ^{7}Li, the disagreement amounts to about four standard deviations σ, well known as the "lithium problem". Recent measurements of the reaction ^{3}He$(\alpha,\gamma)^7$Be, in particular carried out deep underground at LUNA using prompt γ-rays as well as the activation technique, actually worsened the discrepancy [2]. This reaction contributes the major part of the final ^{7}Li abundance through the β-decay of ^{7}Be (see also figure 2.1). The predicted ^{7}Li abundance is $(5.14 \pm 0.50) \cdot 10^{-10}$ with respect to hydrogen, while the observed abundance, inferred from metal-poor halo stars, is $(1.58 \pm 0.31) \cdot 10^{-10}$ with respect to hydrogen.

As ^{7}Li is not the subject of the present work, reference is made to two comprehensive reviews on possible solutions to the "lithium problem" including non-standard physics or non-standard cosmology scenarios [7],[9]. For example, the recent progress in cosmology has revealed that the energy balance of the modern Universe is governed by dark energy and dark matter [9]. The question if and how these peculiar substances have influenced Big-Bang nucleosynthesis is not answered yet, and the related physics is still unknown. Hence it is investigated and debated whether its inclusion to Big-Bang nucleosynthesis can help to reduce or eliminate the "lithium problem".

Similar considerations can be applied in the case of ^{6}Li, where the discrepancy between predicted and observed primordial abundances is exceedingly big, between two and three orders of magnitude: the predicted abundance is in the order of 10^{-14} with respect to hydrogen [2], and the observations suggest an abundance level of about $6 \cdot 10^{-12}$ [4], or ^{6}Li/^{7}Li ≈ 0.05. The observations are debated, and the difficult task to extract a ^{6}Li/^{7}Li isotopic ratio from the spectra of old stars is discussed in section

2.3. But, even if only one of the claimed detections turns out to be significant, the question of a possible primordial origin of ^{6}Li will emerge again, as there is scarcely any noteworthy production of ^{6}Li in old halo stars that could lead to an observable abundance level. Possible production mechanisms of ^{6}Li during and after Big-Bang nucleosynthesis are discussed in the following section 2.2.

2.2. Nucleosynthesis of ^{6}Li

2.2.1. Sources and depletion of ^{6}Li

During Big-Bang nucleosynthesis, the production of ^{6}Li took place at temperatures between $90\,\mathrm{keV}$ and $40\,\mathrm{keV}$ ([5], see figure 2.2), when sufficient ^{2}H and ^{4}He nuclei became available for the ^{2}H$(\alpha,\gamma)^6$Li reaction (see also figure 2.1). Another, much less important contribution came from the ^{3}He$(^3$H$,\gamma)^6$Li and the ^{9}Be$($p$,\alpha)^6$Li reactions. Simultaneously with the production, the efficient destruction of ^{6}Li occcured via the ^{6}Li$($n$,^3$H$)^4$He process, and, as the abundance of neutrons had dropped, the ^{6}Li$($p$,^3$He$)^4$He reaction.

Production of ^{6}Li is not efficient at the relevant energies, since the ^{2}H$(\alpha,\gamma)^6$Li reaction occurs mainly via a weak quadrupole transition, in a radiative capture process below the Coulomb barrier. The low final abundance of ^{6}Li is moreover caused by the efficient destruction via several reaction channels. To study the primordial nucleosynthesis of ^{6}Li, the precise knowledge of only two reaction rates in the related energy range is necessary. The main destruction channel is the ^{6}Li$($p$,^3$He$)^4$He reaction, but the available data are abundant and accurate enough [5], which is not the case for the ^{2}H$(\alpha,\gamma)^6$Li reaction. The plot quoted in figure 2.2 is based on NACRE data. The NACRE evaluation of the ^{2}H$(\alpha,\gamma)^6$Li reaction rates is based on experimental data and theoretical estimations with an uncertainty of about one order of magnitude [10] in the interesting energy range. Hence, the calculated primordial abundance of ^{6}Li carries an uncertainty of $100\,\%$ in this model [5].

After Big-Bang nucleosynthesis, the remaining baryonic matter contained only a tiny fraction of lithium isotopes, conserved until the first stars were formed. Already in 1982 it was well known that both stable lithium isotopes can be easily depleted by proton capture in hot layers of stars (at a temperature of $> 2\,\mathrm{MK}$, [3]). Hence, lithium survives only in the relatively cool and thin atmosphere of a star, from where it can be detected if spectra of such stars are analyzed. In comparably cool stars with a large convection zone, which reaches the mentioned hot layers, lithium is burnt quickly [7]. ^{7}Li is converted into helium via ^{7}Li$($p$,\alpha)\alpha$, and ^{6}Li is depleted to ^{7}Li via the two-step process ^{6}Li$($p$,\gamma)^7$Be$(e^- \ \bar{\nu}_e)^7$Li. In more massive, hot stars (still being dwarfs) with a small convection zone, the atmospheric lithium abundance is believed to be preserved, and these stars, if very metal-poor, are used to infer the primordial lithium abundance.
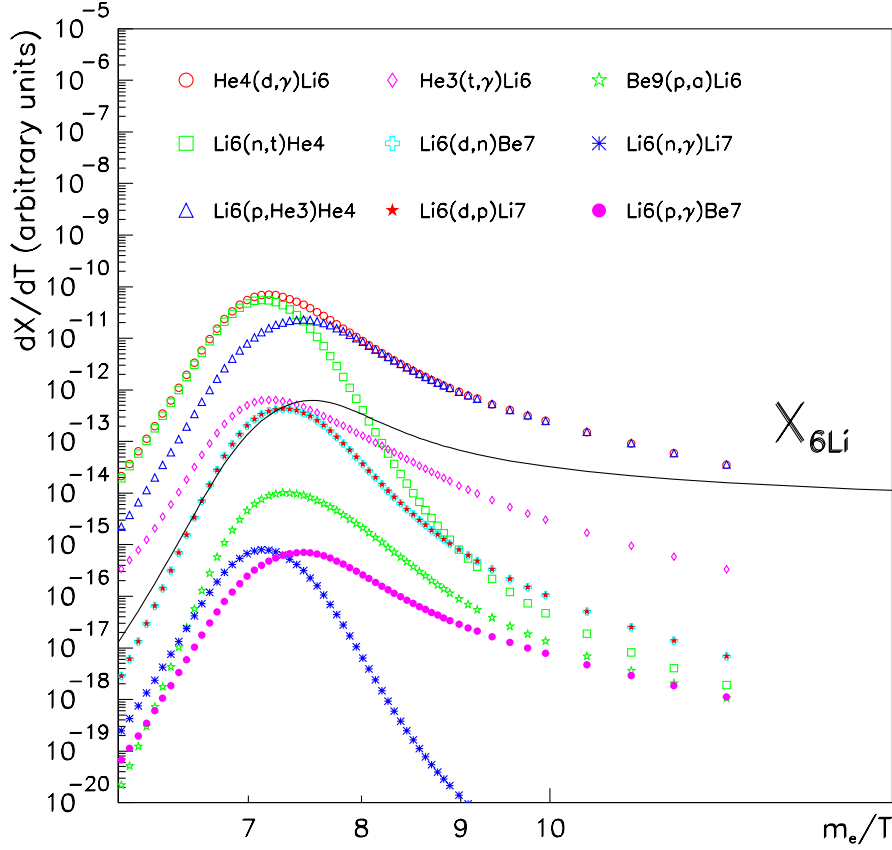
Figure 2.2.: Standard Big-Bang nucleosynthesis of ^{6}Li: Processes of production and destruction, taken from [5]. X_{6Li} is the ratio n_{6Li}/n_B, with n_B being the total number density of baryons.

A production of ^{6}Li in the considered group of stars is not known and even if there would be such a process, they remain to be net destroyers of this lithium isotope. If several additional, possible mixing processes are taken into account (e.g. rotational mixing, diffusion) that increase the depletion of ^{6}Li in stars, the initial content of this isotope would be even larger, worsening the contradiction to the SBBN predictions. Furthermore, attempts to solve the ^{7}Li problem by assuming certain processes of depletion usually worsen the ^{6}Li problem even more [4], as ^{6}Li is much easier depleted than ^{7}Li. Hence it can be concluded that stars with a small convection zone, as it is the case for hot metal-poor halo dwarfs, largely preserve their initial lithium abundance in their atmosphere.

Old metal-poor stars were formed from interstellar gas which was only a little

polluted by nuclei heavier than helium. The only significant process of ^{6}Li production since Big-Bang nucleosynthesis is the interaction of cosmic rays with the interstellar or intergalactic baryonic matter [11], although minor contributions may come from novae and supernovae of type II by neutrino spallation of carbon nuclei. Leading processes are the α-α-interaction (e.g. $\alpha(\alpha,\mathrm{d})^6$Li) and spallation involving protons, α-particles or CNO nuclei, but the α-α-fusion seems to be of much more importance [4]. In this process, lithium is produced with an isotopic ratio of ^{7}Li/^{6}Li $\approx$ 1...2 [12], slowly enriching the interstellar matter with lithium, and increasing the ^{6}Li/^{7}Li abundance ratio.

Still, the observed ^{6}Li abundances in metal-poor halo dwarfs are largely constant over a wide range of metallicity, which rules out that galactic sources of lithium gave significant contributions to the ^{6}Li content of these stars. Possible scenarios of a ^{6}Li production during the formation of our galaxy seem not to yield sufficient ^{6}Li to explain the observed abundances [4]. Other scenarios including new physics are part of the discussion, but there is no proposed model yet which is able to solve all problems at once, without worsening or creating other problems [7]. The question about a primordial origin of the observed ^{6}Li remains, and wether the observations are correct or not.

2.2.2. Nuclear physics of the ^{2}H(α,γ)^{6}Li reaction

As mentioned previously, the ^{2}H(α,γ)^{6}Li reaction occurs non-resonant during Big-Bang nucleosynthesis. It has a positive Q-value of 1473.8 keV (using data from [13]), and, as the first excited state (3+) of ^{6}Li is located at 2186 keV [14], a resonance is found at $E_{\mathrm{CMS}} = 711$ keV. The ground state (1+) is reached via an E2 transition, which dominates the radiative capture reaction also below the resonance, until very low energies are reached (see figure 2.3). In the energy range relevant for Big-Bang nucleosynthesis, the E1 contribution becomes dominant. It is suppressed by the isospin selection rule for $N = Z$ nuclei [6],[15],[16], but the p-waves are less affected by the centrifugal potential that contributes significantly to the potential barrier ([17]):

$$V_{\mathrm{cp}} = \frac{l(l+1)\hbar^2}{2\mu r^2} \approx 20.9\,(\mathrm{MeV\,fm^2})\frac{l(l+1)}{A_{\mathrm{red}}\,R_{\mathrm{n}}^2} \tag{2.1}$$

with R_{n} being the effective nuclear radius of the $d+\alpha$ system:

$$R_0 = 1.4\,\mathrm{fm} \times (A_1^{1/3} + A_2^{1/3}) = 4.0\,\mathrm{fm} \tag{2.2}$$

Hence, E2 transitions are suppressed at lower energies, since the transmission probability of d-waves drops much more rapidly with decreasing energy due to the higher potential barrier.
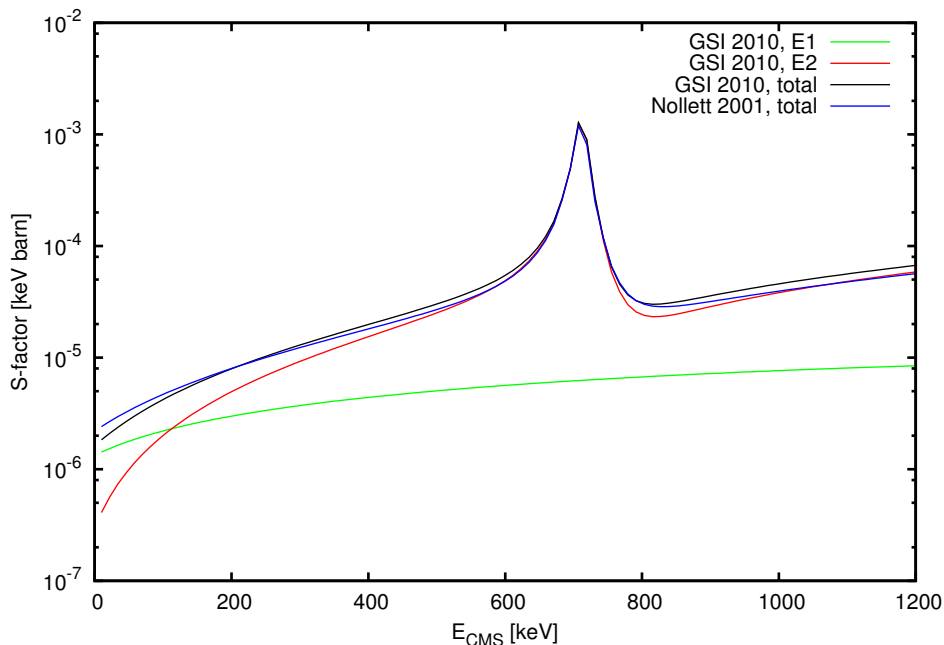
Figure 2.3.: Contributions to the total S-factor of the ^{2}H(α,γ)^{6}Li reaction at low
energies, using the theoretical curve from the GSI group [15], and
for a comparison an earlier work by Nollett et al. [18].

It has been shown that the ^{6}Li nucleus can be described very well by an interacting
system of d and α clusters without internal structure [15]. The radiative capture
below the 711 keV resonance is therefore essentially an extranuclear process.

Thermonuclear reactions in the astrophysical context are usually suppressed by the
Coulomb repulsion between positively charged nuclei. The height of the Coulomb
barrier and the kinetic energy in the center of mass system determine the probability
of quantum tunneling, which can be parameterized as [17]

$$P \propto \exp\left(\frac{-b}{\sqrt{E}}\right) \tag{2.3}$$

The cross section for a nuclear reaction at low energies will show a similar en-
ergy dependence, as such reactions occur only if the nuclei overcome the potential
barrier. In addition, the quantum-mechanical interaction between two particles is
proportional to $1/E$ [17]. The cross section can therefore be also written as

$$\sigma(E) \equiv \frac{S(E)}{E}\exp\left(\frac{-b}{\sqrt{E}}\right) \tag{2.4}$$

9

In this way, the strong non-nuclear energy dependences appear as factors, and the value $S(E)$ contains the nuclear physics content of the reaction probability. It is called the "astrophysical S-factor" [8] of the nuclear reaction.

Nuclear reaction rates are then obtained by folding the cross section with the Maxwell-Boltzmann distribution of kinetic energies inside the plasma, considering resonances if necessary. In the non-resonant case, the integrand is peak-shaped (the so-called "Gamow peak"). Nuclear reactions take place in this narrow energy window, and the knowledge of the S-factors at these energies is crucial to determine the reaction rates correctly. During Big-Bang nucleosynthesis, the Universe cooled down adiabatically, and the Gamow window moved downwards in energy until the vanishing probability of potential barrier penetration stopped the nuclear reactions.

2.2.3. Previous S-factor estimations and measurements

The ^{2}H(α,γ)^{6}Li reaction has attracted some interest in the past, as ^{6}Li is the only stable $A = 6$ nucleus, and the reaction includes $N = Z$ nuclei only. Hence it was studied both experimentally and theoretically (e.g. [19]). In an earlier review [20], the differences between the theoretical predictions available at this time were discussed, amounting up to a factor of ten. The lack of experimental data was a main reason for this issue.

Already in 1981, Robertson et al. [6] measured the cross section and angular distribution directly at energies above 1 MeV with a supersonic gas-jet target, detecting the ^{6}Li nuclei with a magnetic spectrograph instead of detecting the γ-rays. Their angular distribution was inferred from the slight deviations in the ^{6}Li momenta due to the γ-emission. In 1994, Mohr et al. [16] measured cross sections around the 711 keV resonance and its strength and width with a windowless, recirculating gas target, detecting the emitted γ-rays. These direct measurements provided valuable input for theoretical calculations, although extrapolations to lower energies remained uncertain. As reported [20], the asymptotic normalization of the ^{6}Li wave function in the α-d-channel was uncertain, and unexpectedly low dipole contributions in the Robertson data made an extrapolation to lower energies very difficult. Already at this time, a direct cross section measurement below the resonance appeared to be highly desirable. An attempt to measure the cross section directly at an energy of 53 keV provided an upper limit only [21], which has been disregarded by the NACRE collaboration [10] and in other evaluations as it turned out to be too far away from theoretical predictions.

However, as a direct measurement appeared to be impossible due to exceedingly small cross sections, attempts were made to measure them indirectly using the high energy Coulomb breakup method, with an energetic ^{6}Li beam scattered on a high-Z-target. The strong electric field gradient close to the target nuclei causes a disintegration of ^{6}Li nuclei into deuterons and α-particles. This process is treated as the
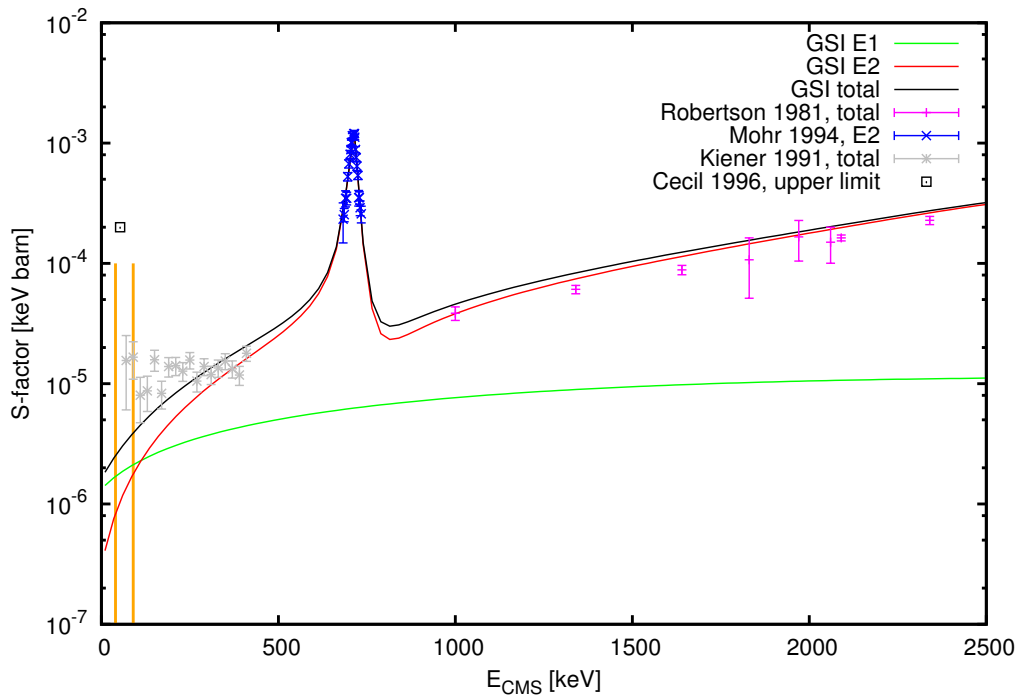
Figure 2.4.: Previous $^2H(\alpha,\gamma)^6Li$ S-factor measurements at low energies, using the NACRE compilation of S-factors [10] and the GSI data [15]. The energy range relevant for SBBN is marked by two orange lines.

absorption of a virtual photon [20], so the $^2H(\alpha,\gamma)^6Li$ reaction is studied as an inverse radiative capture, and the angles and the momenta of the ejected particles have to be measured. From the energy-differential Coulomb dissociation cross section, the radiative-capture cross section can be inferred easily, but nuclear contributions to the breakup and different multipolarities have to be taken into account [15].

In 1991, Kiener et al. [22] bombarded a lead target with a 156 MeV ^6Li beam and calculated a surprisingly constant S-factor below the resonance. A re-analysis by Hammache et al. found that these results are affected by highly dominating nuclear processes and have to be regarded as upper limits [15]. This group provided also the most recent indirect measurement in 2010 at the GSI, using the same technique but a 900 MeV ^6Li beam. Even at this energy, the nuclear breakup was found to be dominant. Furthermore, due to the weak flux of virtual E1 photons, this contribution could not be measured, but inferred from the theoretical model only. From the comparison between predicted and measured Coulomb dissociation cross sections with virtual E2 photons, the applied model could be largely confirmed, and S-factors could be provided for a broad energy range.

The publication of the NACRE evaluation of the ^{2}H$(\alpha,\gamma)^6$Li reaction rates in 1999 was based on several theoretical calculations and on the experimental data provided by Robertson, Kiener and Mohr. The indirectly measured data from Kiener were taken as an upper limit. There has been a revised evaluation in 2010 ([23],[24]) which is still unpublished. The new central value deviates only slightly from the previous estimation, but the uncertainty in the interesting range of $T_9 \approx 0.2$ could be strongly reduced to a level of 50 %. Still, the evaluation is not based on directly measured data there. The mentioned most recent SBBN model calculations [2] are already based on the NACRE II data, but the predicted abundance values were provided without a statement about the remaining uncertainty.

2.3. Lithium dectection in stars

The abundance of lithium in the atmosphere of stars is inferred from the spectral analysis of their emitted light. Every element leaves a characteristic signature of absorption lines in the spectrum. For a precise determination of abundances, high-resolution spectra with high signal-to-noise-ratios are necessary to properly fit the lines. To reliably understand the relation between their shape and the corresponding abundance, sufficient knowledge about parameters like distance, space motion and the galactic orbit of the star, and atmosphere parameters (radial velocity, effective temperature, gravity and relative metal deficiency [Fe/H]) is necessary [3].

This technique has been available already in 1982, about 30 years ago, when F. and M. Spite reported a plateau of observed ^{7}Li abundances in metal-poor halo dwarfs over a wide range of metallicity (a factor of 12 to 250 lower with respect to the sun) [3]. Observations were anyway difficult due to the faintness of the interesting stars, which made a long integration time necessary, and the faintness of the observed lithium resonance line at $\lambda = 670.7$ nm. The presence of ^{6}Li introduces additional width and asymmetry to this line [4], but the resolution did not allow to determine the ^{6}Li/^{7}Li ratio at this time. Owing to the position of the line and the low expected primordial ^{6}Li production, the predominance of ^{7}Li over ^{6}Li had been presumed. For the analysis, a local thermal equilibrium (LTE) model of the star's atmosphere was employed. As reported, the largest contribution to the uncertainty of the abundance came from the difficulty to precisely determine the temperature of the star, which is necessary to correct for the amount of ionized lithium in the star's atmosphere [7]. Nevertheless, the existence of a ^{7}Li abundance plateau was evident, and, apart from new constraints of the baryon-to-photon ratio, questions about the possible primordial origin of lithium in the observed stars, and the expected depletion in stars arised.

Following publications confirmed the existence and the position of the ^{7}Li abundance plateau. Observations of ^{6}Li in single stars have been reported since 1993 [25].

More than twenty years after the publication of Spite and Spite, Asplund et al. [4] analyzed high-quality spectra of 24 metal-poor halo dwarfs and subgiants, with signal-to-noise-ratios being typically more than ten times higher than available in 1982, with the possibility to infer ^{6}Li/^{7}Li abundance ratios. ^{6}Li has been detected in nine of the observed stars with a significance of more than $2\,\sigma$ and at the same abundance level (^{6}Li/^{7}Li ≈ 0.05), indicating a second plateau of ^{6}Li abundances below the ^{7}Li plateau.
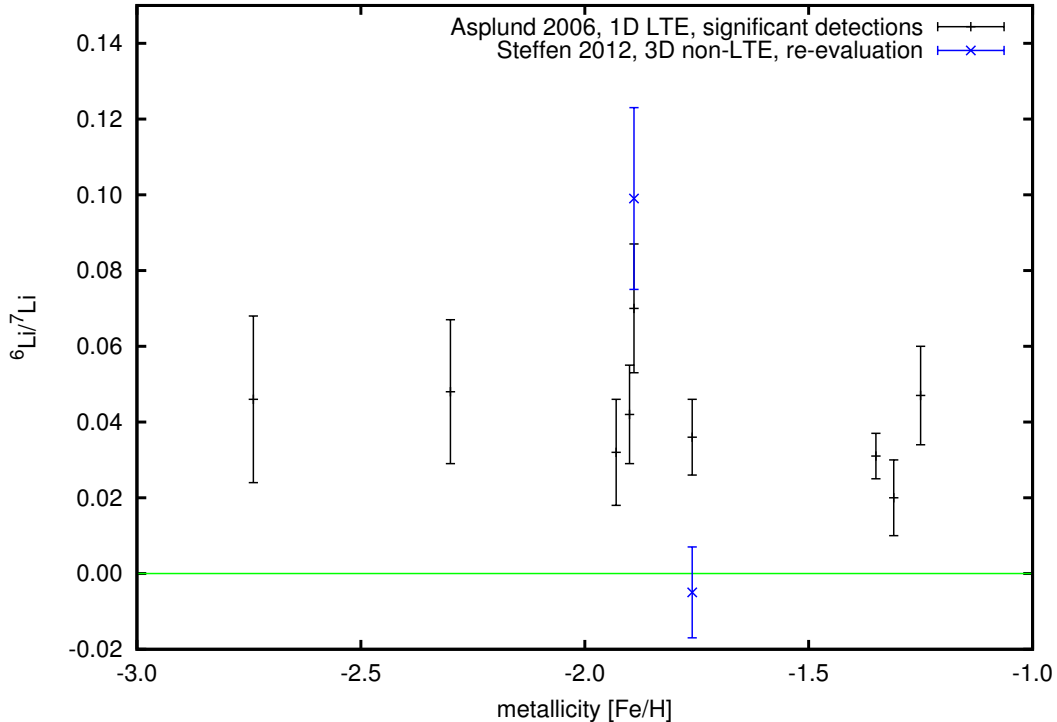
Figure 2.5.: Significant ^{6}Li detections in the Asplund et al. survey 2006, with data from [4]. Two of these stars were subject of the re-evaluation by Steffen et al. [26], the new ^{6}Li/^{7}Li ratios are shown in blue.

The stars for this survey were chosen conveniently: Having a metallicity of -3.0 < [Fe/H] < -1.0 and being in the turnoff region of the Hertzsprung-Russell diagram. There, the destruction of ^{7}Li is suppressed, because the upper convection zones are too thin to transport lithium to the hot core. Furthermore, relatively bright stars were chosen to increase the signal-to-noise ratio, and double-lined binary star systems were avoided [4].

The shape of the Li absorption line depends not only on the lithium isotopic ratio, but is strongly influenced by several features of the star's atmosphere which have to

be well known and modeled to make sure that a presence of ^{6}Li is not mimicked by the convective motion of the gas or by an inadequate modeling of the atmosphere. Hence thermal, pressure, radiative, rotational and Doppler broadening have to be considered, and in addition, the instrumental line broadening has to be taken into account [4]. The Doppler broadening is introduced by velocity fields from convection, wave motion and turbulences. To describe the star's atmosphere, a 1D local thermal equilibrium (LTE) model of the atmosphere was employed in the 2006 survey [4].
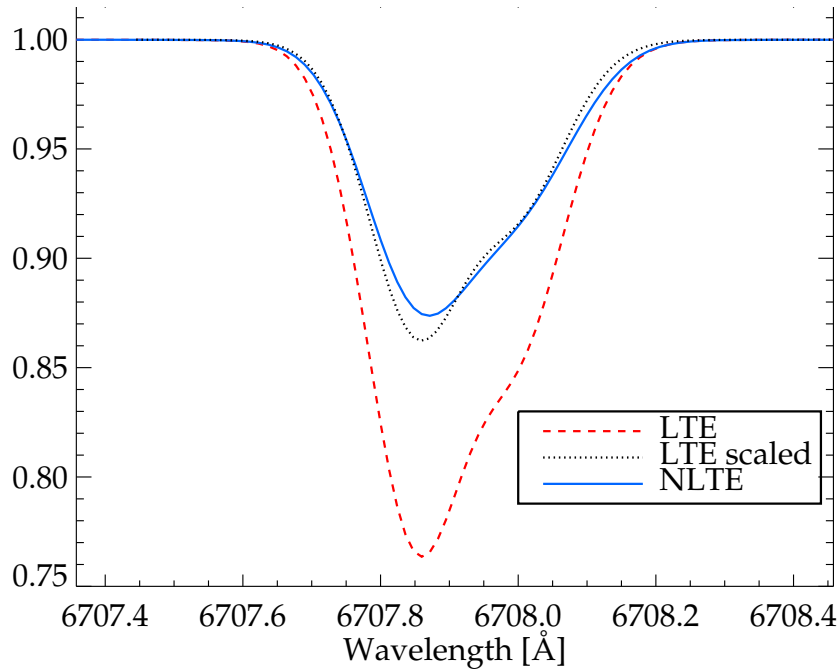
Figure 2.6.: Synthetic profiles of the Li resonance line in star spectra, taken from [27] with an assumed ^{7}Li abundance of $\log(N_{^7\mathrm{Li}}/N_\mathrm{H}) = -10$ and ^{6}Li/^{7}Li $= 0$.

The measured ^{6}Li abundances attracted much interest and triggered many efforts to better understand the data analysis. In 2007 it was argued by the Paris group that the minimal asymmetry due to the presence of ^{6}Li could have been mimicked by convective motions in the star's atmosphere, and that a 3D non-LTE model could solve this issue, converting the previous significant detections of ^{6}Li into upper limits [28]. Already in 2006 it was doubted that LTE assumptions can always be readily applied in certain metal-poor stars [4]. In 2012, with the availability of more computation power, Steffen et al. in collaboration with the Paris group were able to quantify the effect of the convective line asymmetry on the previously measured ^{6}Li abundances

by comparing 1D LTE and 3D non-LTE line profiles ([26], see also figure 2.6). The number of the significant ^{6}Li detections had to be strongly reduced in this way, but notably two stars remained having a ^{6}Li detection with a confidence level of $3\,\sigma$.

The very recent evaluation of four very metal-poor stars by Lind et al. [27] using a combined 3D, non-LTE modeling technique for several calibration lines showed that the observed intrinsic asymmetry of the 670.8 nm lithium line does not require the presence of ^{6}Li. In none of the considered stars, a significant detection of ^{6}Li remained (see also table 2.1 for two examples).

Star	Reference	^{6}Li/^{7}Li [%]
HD 84937	Smith et al. 1993 [25]	5 ± 2
	Steffen et al. 2012 [26]	5.1 ± 2.3
	Lind et al. 2013 [27]	$1.7 \pm 0.7 \pm 0.6$
G64-12	Asplund et al. 2008 [29]	5.9 ± 2.1
	Steffen et al. 2012 [26]	0.8 ± 2.7
	Lind et al. 2013 [27]	$-0.2 \pm 1.3 \pm 0.6$

Table 2.1.: Two examples for the revision of observed ^{6}Li abundances when introducing 3D non-LTE models to the analysis.

2.4. The status of the discussion

If the results of the recent analysis by Lind et al. [27] can be extended to all other old stars in which ^{6}Li was detected before, there would be no more "^{6}Li-problem". The predicted extremely low final abundance of ^{6}Li in SBBN can not be observed in stars with currently available methods, and a vanishing of the ^{6}Li abundance plateau introduced by Asplund et al. in 2006 would therefore match the predictions. Furthermore, proposed solutions of the ^{7}Li problem which include depletion by stars would become more interesting, as the models would not have to explain anymore how ^{7}Li can be depleted while a comparably high abundance of ^{6}Li remains. Cosmic ray spallation processes provide enough ^{6}Li to explain its abundance e.g. on the Earth today.

However, if significant detections of ^{6}Li in old metal-poor stars remain [26], the question about the origin of this isotope arises again, and a primordial origin is one of the possible answers. A wrong prediction by the parameter-free Standard Big-Bang Nucleosynthesis model is most likely either due to inadequate nuclear data or due to wrong assumptions about the laws of physics during Big-Bang Nucleosynthesis. Many calls for directly measured ^{2}H(α,γ)^{6}Li cross section data in the relevant energy range have been published, to improve the credibility of the adopted reaction rates, to reduce their uncertainty, and to constrain exotic scenarios.

3. The LUNA gas target setup

The S-factor of the ^{2}H$(\alpha,\gamma)^6$Li reaction was measured by observation of specific emitted γ-rays when a beam of ^{4}He$^+$ ions was incident on a deuterium gas target. The experiment was carried out deep underground at the Laboratory for Underground Nuclear Astrophysics (LUNA) [30], located inside Laboratori Nazionali del Gran Sasso in Italy. In the following sections, the LUNA gas target setup is described, as well as its development and how the final parameters for the measurements were found.

3.1. The LUNA2 accelerator

The 400 kV electrostatic ion accelerator is embedded in a steel tank. It is filled with a mixture of several dry gases (about 75% N_2, 15% SF_6 and 10% CO_2) at a pressure of 20 bars to prevent sparkovers at high electrical field intensities. The high voltage is provided by an Inline-Cockroft-Walton power supply [31]. It is stabilized by a RC-filter and an active feedback loop. This is of certain importance, as the cross section to be measured depends exponentially on the beam energy. Using a proton beam, it has been shown that the long-term energy stability is given within $\pm\,2\,$eV, and an energy calibration has been obtained, which was also used to determine the precise energy of α-particles incident on the deuterium gas target.

The radio-frequency ion source can provide beams of protons or α-particles, the former reaching intensities up to $500\,\mu$A according to [31]. In the case of the ^{2}H$(\alpha,\gamma)^6$Li measurement, intensities between 150 and more than $400\,\mu$A on target were reached. Beam currents above a value of $380\,\mu$A at a beam energy of 400 keV already exceeded the measuring range of the beam calorimeter, hence beam currents above $370\,\mu$A were usually avoided. As an attempt to reproduce the beam induced background obtained with the α-beam, some short measurements using a ^{3}He beam from the same machine were obtained as well.

To enter the gas target beam line, the beam is bent by $45°$ by a highly stable, water cooled electromagnet. A vertical steerer is located right before it. After having passed a Faraday cup and the gate valve, the beam is collimated by the first aperture ($d = 25\,$mm, see also figure 3.2) behind the third pumping stage. A second aperture ($d = 15\,$mm) collimates the beam further, before it finally enters the gas target via the long, narrow target collimator ($l = 40\,$mm; $d = 7\,$mm). All apertures are connected with ampere meters, to help adjust and focus the beam properly.
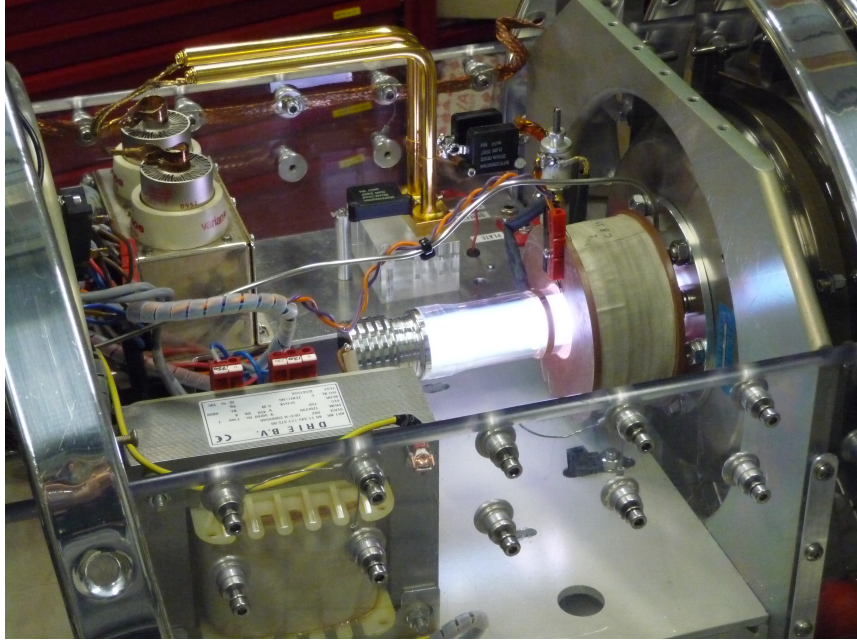
Figure 3.1.: The RF ion source running with helium gas.

The beam is finally stopped at a calorimeter made of massive copper. On its front side, towards the beam, it is evenly heated by several resistors. The power supply is controlled by a feedback system which permanently reads the temperatures measured by several PT100 resistors inside the calorimeter head. Usually, the temperature of the hot side has been kept at 70°C. The other side of the calorimeter was constantly cooled to a temperature of 0°C, and heating and cooling were in an equilibrium. If the calorimeter is hit by the beam, less power is necessary to keep the temperature set point, and a new equilibrium is found by the feedback system within about one minute. From the difference in power the beam current can be precisely measured if the beam energy is known:

$$I_{\text{beam}}[\text{mA}] = \frac{P_{\text{w/o beam}} - P_{\text{with beam}}}{E_{\text{beam}} - \Delta E} \frac{[\text{W}]}{[\text{keV}]} \tag{3.1}$$

The correction ΔE allows for the energy loss of incident α particles in the target gas and amounts 2...4 keV depending on the gas pressure and the beam energy, which is discussed in detail in section 3.2.2. All power values and temperatures were permanently logged to allow the calculation of the integrated beam charge.

3.2. The windowless gas target

3.2.1. Design

The gas target is windowless, so any energy straggling due to a solid object in the beam path is avoided. Because of the absence of a physical barrier between the gas target and the ultra high vacuum in the accelerator, a system of powerful vacuum pumps is necessary to remove the target gas completely. Pressures of up to 1 mbar have been reached inside the target chamber while always keeping the accelerator vacuum in the order of 10^{-7} mbar.
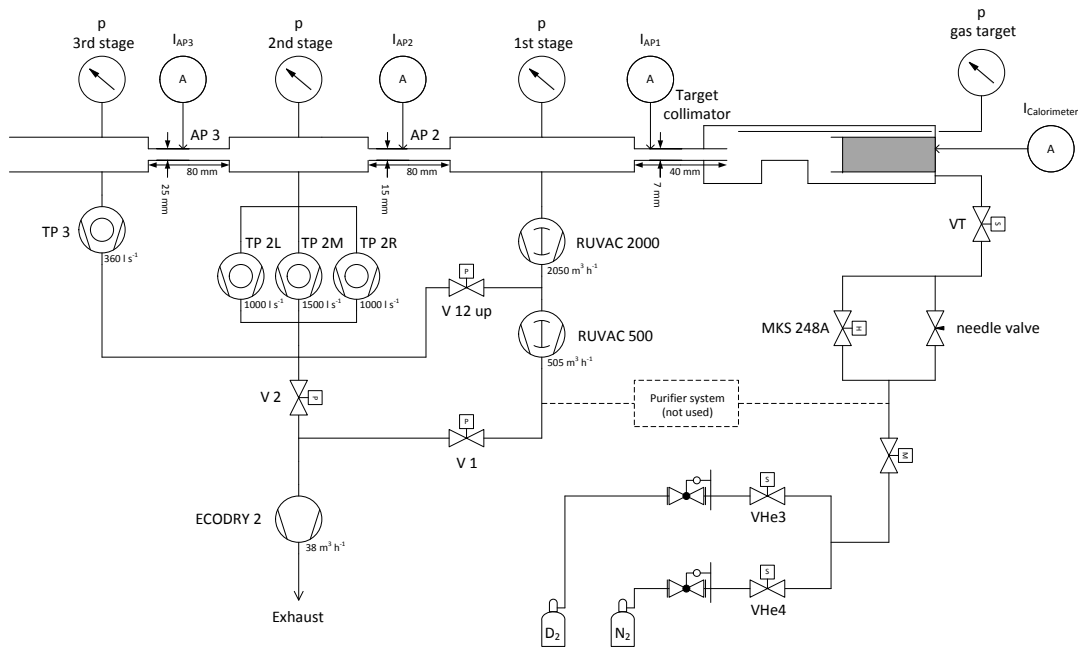
Figure 3.2.: Layout of the windowless gas target. The valves are marked as follows: M - manually, S - Labview controlled and electric driven, P - Labview controlled and pneumatic driven, H - thermal leak

The gas is inserted in the target chamber by a pipe connected to the end flange. The pressure inside the chamber is measured close to the target collimator, by a long copper tube which is fed through the end flange as well, and connected to a high precision Baratron capacitive pressure gauge (see figures 3.3 and 3.2). In a previous LUNA experiment, using a similar target chamber, it was shown that the gas pressure along the target range is constant [32]. The target collimator (7 mm diameter, 40 mm length) serves as the main gas flow resistance, hence the gas flux is low enough to ensure a reasonable deuterium consumption and a sufficient gas
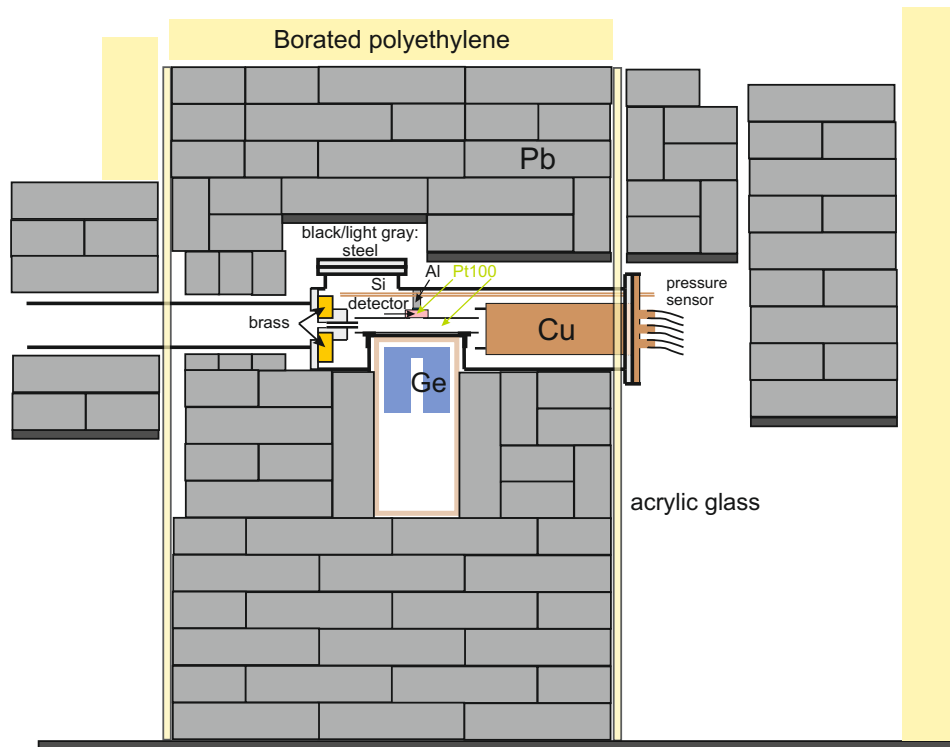
Figure 3.3.: Cut of the complete setup through the center, along the beam axis. Drawn to scale.

removal by the vacuum pumps. The deuterium was provided by a bottle outside the LUNA box, with a pressure of 1 bar behind the pressure reducer. The gas had a composition of 99.8 mol% of D_2 and 0.2 mol% of N_2.

The pressure inside the gas target is controlled by an analog feedback system and logged permanently by a Labview application. The primary contribution to the gas flow is delivered by a needle valve, while the amount needed to reach the final pressure is maintained through a second path. Its gas flow is regulated through a thermal leak valve, driven by the gauge controller unit. The target pressure never deviated by more than 3 % from the desired value.

The length of the gas target was 192 mm. This value includes the nozzle of the target collimator and the entire length of the beam path until the surface of the calorimeter. A precise drawing of the inner components of the target chamber is given in figure 4.6, a photo is shown in figure 3.10. 172 mm of the beam path were surrounded by a steel tube (with a wall thickness of 1 mm). Its intention was to stop scattered deuterons and to hold the silicon detector. Due to the precise alignment and good collimation, the beam never touched the tube.
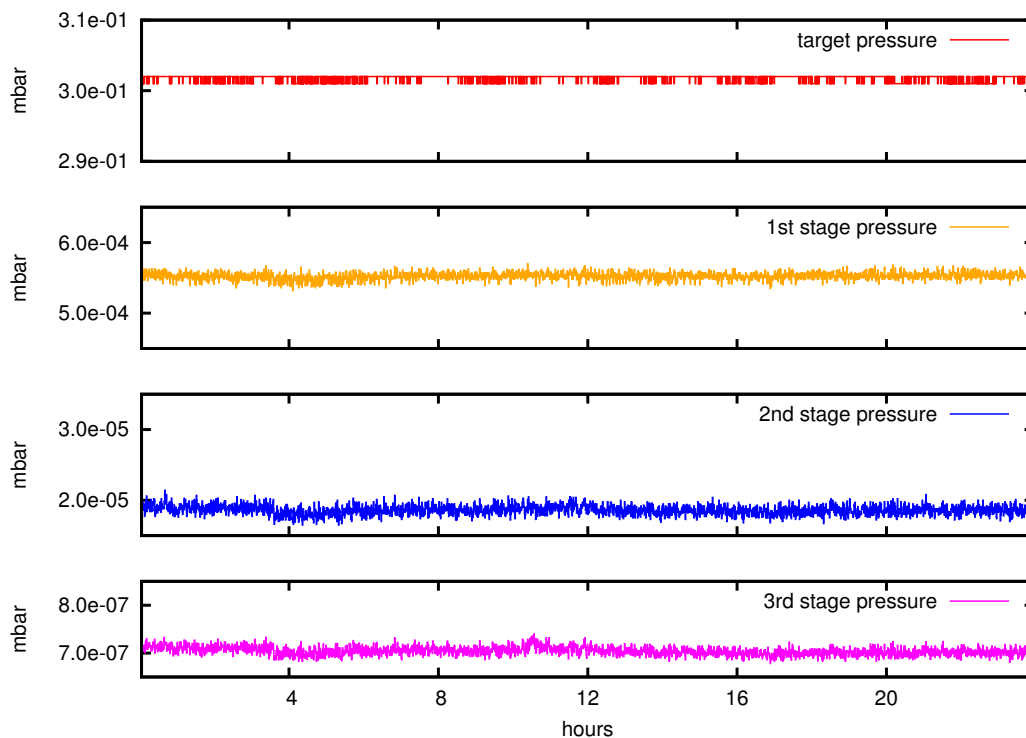
Figure 3.4.: Long-term stability of the gas target and pressures at the different pumping stages within one day and with incident ion beam. Data from a run at October 1st, 2011, at 400 keV beam energy and 0.3 mbar nominal target pressure.

3.2.2. Parameters

To calculate a cross section, the target density must be known and hence the gas temperature along the beam path. The gas inlet is well below the cold side of the calorimeter, which has a temperature of about 0 °C. The gas flow passes the hot side of the calorimeter (70 °C) and leaves the target chamber via the target collimator, which is water cooled. The gas temperature along the beam path is mainly influenced by the temperature of the steel tube and the beam heating.

To measure the temperature profile along the steel tube, a PT100 sensor has been mounted at various positions (see figure 3.5, the configuration during data taking). The temperatures were obtained with a working gas target at several target pressures and without the beam. The results are shown in figure 3.6 with an attempted interpolation. Towards the target collimator, the gas temperature does not depend on the pressure. A noticable difference has been measured towards the calorimeter, some heat was carried by the gas flow from its hot side.
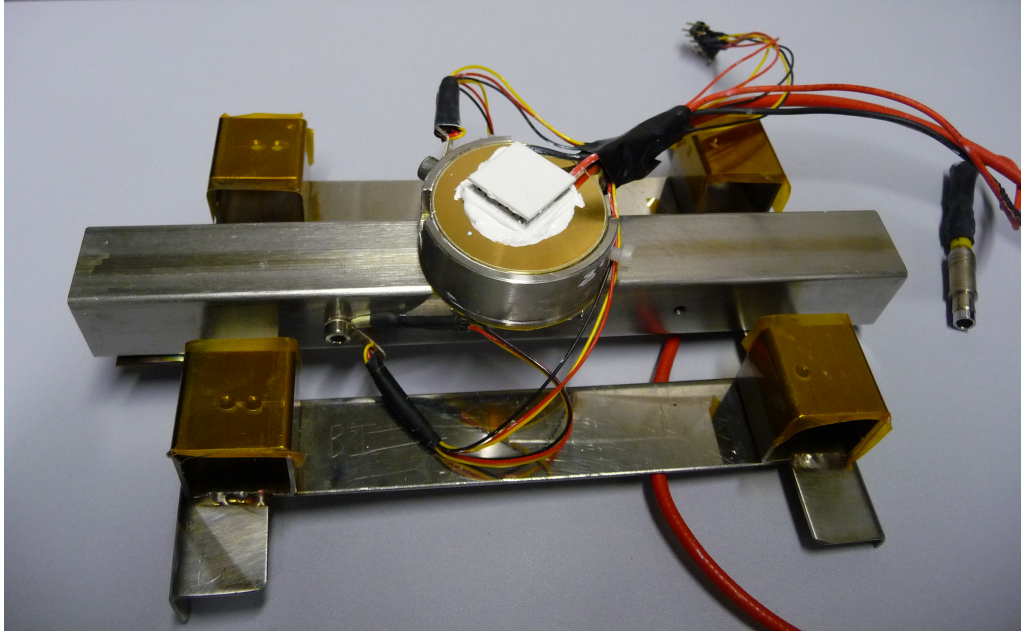
Figure 3.5.: The PT100 sensors and the silicon detector mounted on the steel tube. The Peltier element is attached on the top of the detector case. The beam enters from the left side.

With the beam, a temperature-related correction to the gas pressure is necessary to avoid an overestimation of the target density. The temperatures of the actively tempered components (collimator and calorimeter) do not change, but some power is dissipated to the gas along the beam through stopping of incident alpha particles. The temperature of the steel tube rises until a new equilibrium is established. Nevertheless, right inside the beam the gas temperature is the highest.

To estimate the temperature profile of the steel tube with beam on target, the values of the PT100 sensor attached to a fixed position (as in figure 3.5) are compared with values obtained without beam. The difference is about $10\,\text{K}$. It is assumed that this difference is the same for all other positions along the steel tube. The typical measurement parameters were a beam energy of $400\,\text{keV}$, a beam intensity of $300\,\mu\text{A}$ and a target pressure of $0.3\,\text{mbar}$. For a beam energy of $280\,\text{keV}$, very similar temperatures were observed. The major influence is given by the beam intensity, but a deviation of $50\,\mu\text{A}$ changed the temperature level by a few Kelvin only.

Defining the tip of the target collimator as the position $x = 0$, the temperature curve can be approximated by

$$T(x) = (30.3 + 8.20 \times 10^{-3}x + 6.00 \times 10^{-4}x^2)\,^\circ\text{C} \tag{3.2}$$
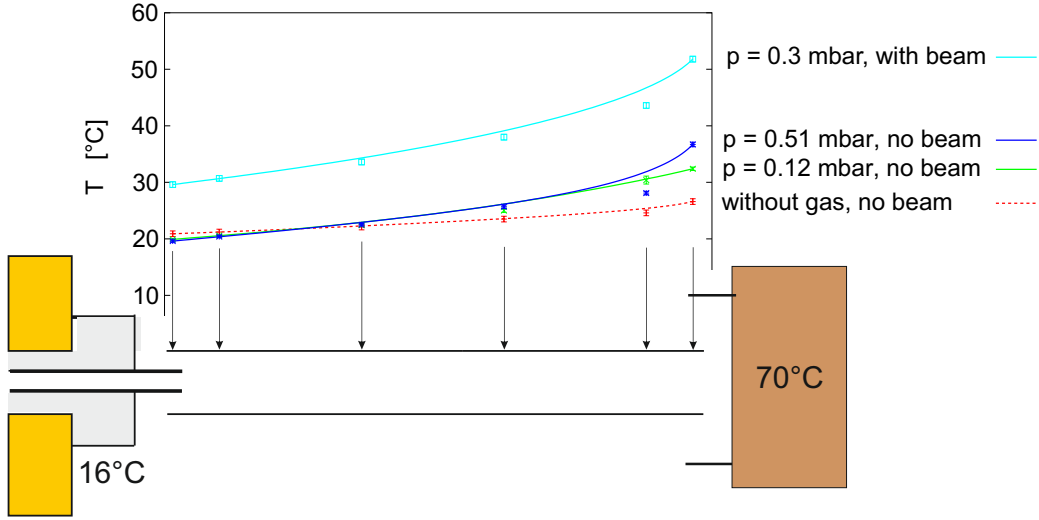
Figure 3.6.: The temperature profile of the gas target with and without beam at several gas pressures. The beam intensity is about $300\,\mu\text{A}$.

The average temperature is

$$\overline{T} = \frac{1}{L} \int_0^L T(x)dx = 37\,°\text{C} = 310\,\text{K} \tag{3.3}$$

with $L = 177\,\text{mm}$ as the distance between the tip of the collimator and the beam stop.

Assuming a thermal equilibrium $T(x) = const.$ and applying $V = const.$ and $p = const.$, the gas density is inversely proportional to the absolute temperature, because $NT = const.$ and $\rho \propto N$ in our case. The gas density ρ_1 at a temperature T_1 is given by

$$\rho(T_1) = \frac{T_0\,\rho(T_0)}{T_1} \tag{3.4}$$

assuming deuterium to behave like an ideal gas at lower pressures. According to literature, $\rho_0(T_0 = 288\,\text{K}) = 0.168\,\text{kg m}^{-3}$ [33]. A good first estimation for the beam heating correction is $8\,\text{K}$ (see below for a justification of this assumption), so the standard gas density is determined to $\rho(318\,\text{K}) = 1.52 \times 10^{-4}\,\text{g cm}^{-3}$.

To estimate the energy loss of α-particles and the power dissipation in the deuterium gas, the stopping power is calculated using SRIM 2013 [34]. The value $\rho(318\,\text{K})$ is used as input for the gas density. In order to understand the influence of changing temperatures on the stopping power, the calculation was repeated

four times with different temperatures, the results are shown in figures 3.7 and 3.8, along with second-order polynomial fits. From the results, the stopping power can be expressed with a good approximation by

$$\frac{dE}{dx}\left[\frac{\text{keV}}{\text{cm}}\right] = (4.11 \times 10^{-2} + 5.79 \times 10^{-4} E_{\text{beam}} - 5.81 \times 10^{-7} E_{\text{beam}}^2)$$

$$- 5.23 \times 10^{-4} \left(T - T_0\right) \tag{3.5}$$
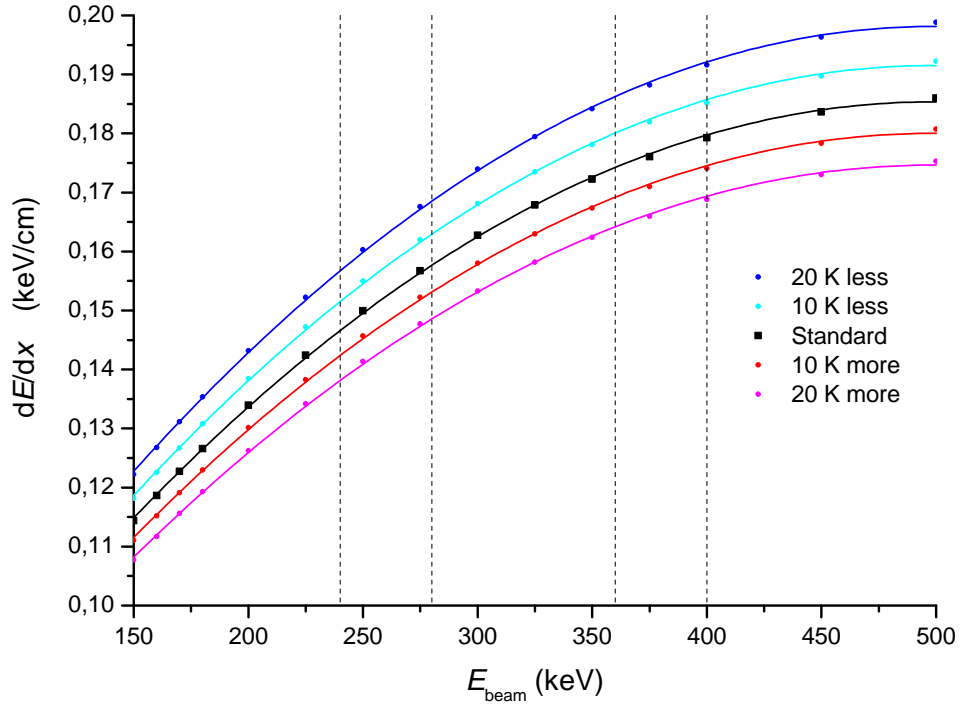
Figure 3.7.: Stopping power of incident α-particles for various beam energies, obtained with SRIM 2013. The four measurement beam energies are marked with dashed lines.

The power dissipation can be determined with the beam current via

$$H = \hat{I}\,\frac{dE}{dx} \tag{3.6}$$

$\hat{I}$ is the number of incident particles per second, obtained with

$$\hat{I} = \frac{I_{\text{beam}}}{e} \tag{3.7}$$

With standard parameters, $\hat{I} = 1.87 \times 10^{15}\,\text{s}^{-1}$ and $H = 54\,\text{mW}\,\text{cm}^{-1}$ at $400\,\text{keV}$ beam energy.
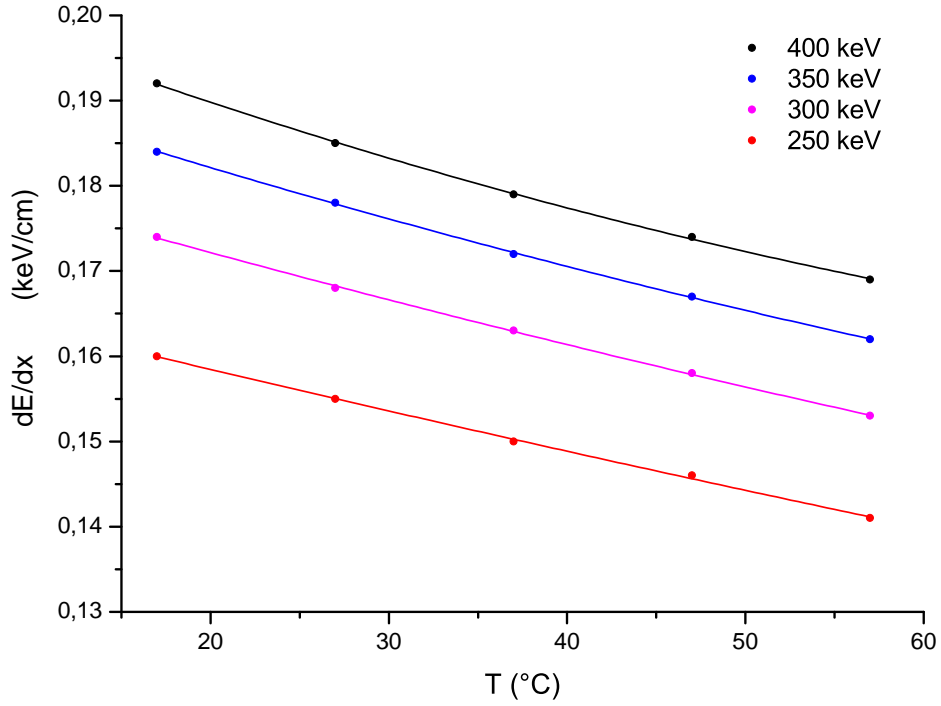
Figure 3.8.: Stopping power of incident α-particles for various gas temperatures, obtained with SRIM 2013.

Using this heat flow, the temperature difference ΔT can be estimated according to [35] via

$$\Delta T = \frac{H}{2\pi\lambda}\,\ln\frac{b}{a} \tag{3.8}$$

where λ is the thermal conductivity of deuterium ($131\,\text{mW}\,\text{m}^{-1}\,\text{K}^{-1}$, [33]), b is the inner radius of the steel tube (assumed to be $11\,\text{mm}$) and a is the radius of the beam

(3.5 mm). Using these values, in case of 400 keV beam energy and standard measurement parameters, the correction is $\Delta T = 7.5$ K, and the previous estimation is justified. Table (3.1) summarizes the gas target parameters for several beam energies.

Beam energy (keV)	dE/dx (keV/cm)	H (mW/cm)	ΔT (K)	n 10^{16} cm^{-3}
400	0.180	54	7.5	1.37
360	0.174	52	7.3	1.37
280	0.158	47	6.6	1.37
240	0.147	44	6.1	1.37

Table 3.1.: The gas target parameters for several beam energies. The target pressure is 0.3 mbar, and the beam current is assumed to be 300 μA.

In the end, the target density inside the beam is slightly reduced by beam heating effects. A second order correction, taking into account the reduced density, the reduced stopping and hence a reduced beam heating is negligible. Still, the adopted values for beam heating and target density have to be determined from the actual beam current, which usually deviates from the assumed 300 μA.

Assuming deuterium to behave like an ideal gas at lower pressures, the target density is finally given by

$$n = \frac{N}{V} = \frac{2p}{k(\overline{T} + \Delta T)} \tag{3.9}$$

With beam on target, in the standard case, $n = 1.4 \times 10^{16}$ cm^{-3} and is nearly independent from the beam energy, because the differences in the beam heating corrections are small compared to the absolute temperature.

3.2.3. Safety features

The entire setup (including the accelerator) was designed to run continuously and without permanent surveillance, so several safety precautions were implemented, to avoid serious damages to the equipment.

- Failure of vacuum pumps. In this case, or in case of a sudden pressure surge, a fast gate valve closed the beam line, and the beam was stopped by a Faraday cup in front of the gate valve. Both devices were driven by pressurized air. A failure of the compressor unit stopped the accelerator.

- Failure of the cooling machine. In this case, the beam power could not be transported away, causing a serious overheating of the calorimeter. To avoid

this, the control of the Faraday cup was connected to a relay in the cooling machine. Every error status interrupted the beam.

- Accelerator interlocks. The beam was stopped immediately in case of terminal sparks or people entering the accelerator room during the measurement.

- Explosive gas mixtures. Several gas sensors are installed inside the accelerator room to measure the hydrogen content of the air.

- Remote control. The gas target, the calorimeter and the Faraday cup could be controlled from outside the underground lab, to quickly intervene (such as stopping the D_2 supply) in case of dangerous situations.

3.3. The detectors

3.3.1. Description and position

γ-rays from the ^{2}H$(\alpha,\gamma)^6$Li reaction were detected by an ultra-low background high-purity germanium detector (Canberra GC15024) with a high relative efficiency of 136.6 % (as stated in the data sheet). The detector was located as close as possible to the beam to maximize the detection efficiency. The distance between the beam center and the surface of the detector window was about 15 mm. The germanium crystal has a coaxial open end geometry, where the closed end pointed towards the beam, with a nominal distance between crystal and window surface of 5 mm. In table 3.2, measured and quoted detector specifications are compared.

Parameter	1332 keV γ-rays from ^{60}Co		HPGe crystal	
	FWHM	Peak/Compton	diameter	distance
data sheet	2.16 keV	86.0:1	91 mm	5 mm
measured	2.7 keV	65:1	85 mm*	12 mm*

Table 3.2.: Specification and performance data of the HPGe detector.
* These values were found empirically by adjusting the setup geometry in Geant4 to reproduce the measured efficiency curves.

The detector was cooled by liquid nitrogen in a Dewar vessel and operated at +5.0 kV bias voltage with an emergency bias shutdown feature. It stood on a rack with rubber foots to attenuate microphonics from the vacuum pumps. The detector head was surrounded by a massive lead shielding with a thickness of at least 20 cm. Further details about the measured efficiency and γ-energy resolution are written in section 3.4.

Figure 3.9.: The HPGe detector inside the surrounding lead shielding during construction. The small pipe below the cold finger conducted nitrogen gas inside the setup, to remove ^{222}Rn.

A partially depleted silicon surface barrier detector was located on top of the steel tube to detect charged particles (especially protons) from the ^{2}H(^{2}H,p)^{3}H reaction, to have an indirect measure of the neutron flux originating from the ^{2}H(^{2}H,n)^{3}He reaction. It has an active area of $450\,\mathrm{mm}^2$ and a sensitive thickness of $>1500\,\mu$m. To allow the protons reaching the detector, a window was machined into the steel tube. To protect the detector from the flow of scattered particles, a $25\,\mu$m thick layer of aluminum foil was placed between the window and the detector. Scattered deuterons and α-particles were stopped after a few μm already, but protons with an energy of more than $1.5\,\mathrm{MeV}$ could pass. The detector was housed in a steel case and connected to the preamplifier outside the target chamber via a microdot plug. The optimal bias voltage was found to be $+160\,\mathrm{V}$. In table 3.3, measured and quoted specifications are compared.
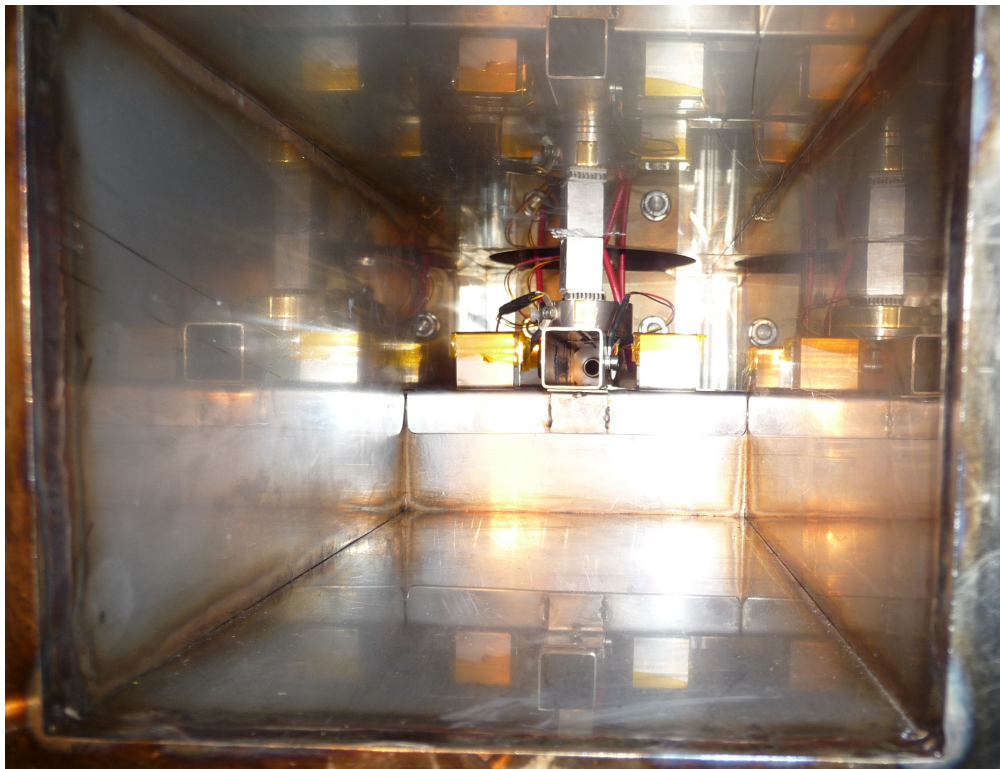
Figure 3.10.: A view inside the target chamber. The collimator is visible at the end of the steel tube. The case of the Silicon detector is cooled by a Peltier element, its hot side covered by an aluminum bar.

Parameter	Serial no.	Operating bias	5.5 MeV FWHM
data sheet	49-152 A	+160 V	20 keV
data sheet	49-152 B	+150 V	21 keV
measured	49-152 B	+160 V	$\geq$25 keV

Table 3.3.: Specification and measured energy resolution data of the silicon detectors using a ^{241}Am α-source.

The measured energy resolution of 25 keV was reached with optimal conditions and in a different vacuum chamber only. In the ^{2}H(α,γ)^{6}Li setup, an energy resolution of about 100 keV was measured. Reasons for this difference were a noisy environment (see also the following section) and non-removable mass loops. The energy calibration of the detector was usually done with a ^{241}Am source and a pulser (Ortec 419) connected to the test input of the preamplifier. The data points needed to calculate a calibration function were gained by changing the attenuation factor of the pulser

output. The particle detection efficiency could be obtained from a Monte Carlo simulation only, because the proton field had a broad energy distribution, additionally affected by the aluminum foil, and the proton source a large volume.

According to the provided quality assurance data sheet, an energy resolution of 26 keV FWHM (5.486 MeV α-particles) is warranted for temperatures of 22 °C only. During operation, the PT100 temperature sensor attached to the case of the silicon detector measured temperatures above 40 °C without any added cooling mechanism. To avoid additional noise problems and hence a further loss of energy resolution, an active cooling was necessary. The transport of heat just by convection is too small in an environment of low gas pressure, and the silicon detector had a thermal connection to the steel tube, which was heated both by the beam and the calorimeter. To provide an active cooling, the upper surface of the detector was partially covered by the cold side of a Peltier element and thermally connected using a vacuum-proof heat conducting paste (see figure 3.5). The hot side was thermally connected likewise to the target chamber via an aluminum bar (see figure 3.10). In order to prevent electronic noise due to an additional mass loop, the power supply of the Peltier element was fed in without any electrical connection to the setup. With an operating current of about 500 mA and an additional power dissipation of 650 mW, the measured temperature at the PT100 sensor was always kept at or below 23 °C during operation.

3.3.2. The data acquisition system

Three (later two) NIM crates in the accelerator room, close to the target, contained the electronic instrumentation to supply the detectors and to process the signals coming from their preamplifiers. The complete electronic chain is shown in figure 3.11. Two data aquisition systems ran in parallel: An analog branch concluded by an Ortec 919E multichannel analyzer, and a digital branch with a Caen1728B digitizer module in list mode. The output of the silicon detector was connected to the analog branch only, the output of the γ-detector was used by both branches.

The digital Caen module was connected to the energy output of the HPGe preamplifier. The fast timing signal was used for the analog branch and looped through to a fast timing filter amplifier (Ortec 474). Together with a constant fraction discriminator, a digital signal was generated to start a longer inspection interval during which the event was analyzed. If a second event occurred within this interval, distortion through pile up was likely, and both events were discarded. The time stamp and number of these incidents was logged. Due to the low counting rate, this number was always very small compared to the total amount of events. The Caen module also allowed to visualize and store the shape of incoming signals, which has been done usually, to extract additional information (e.g. for a separation of neutron or γ-induced events) later if needed.
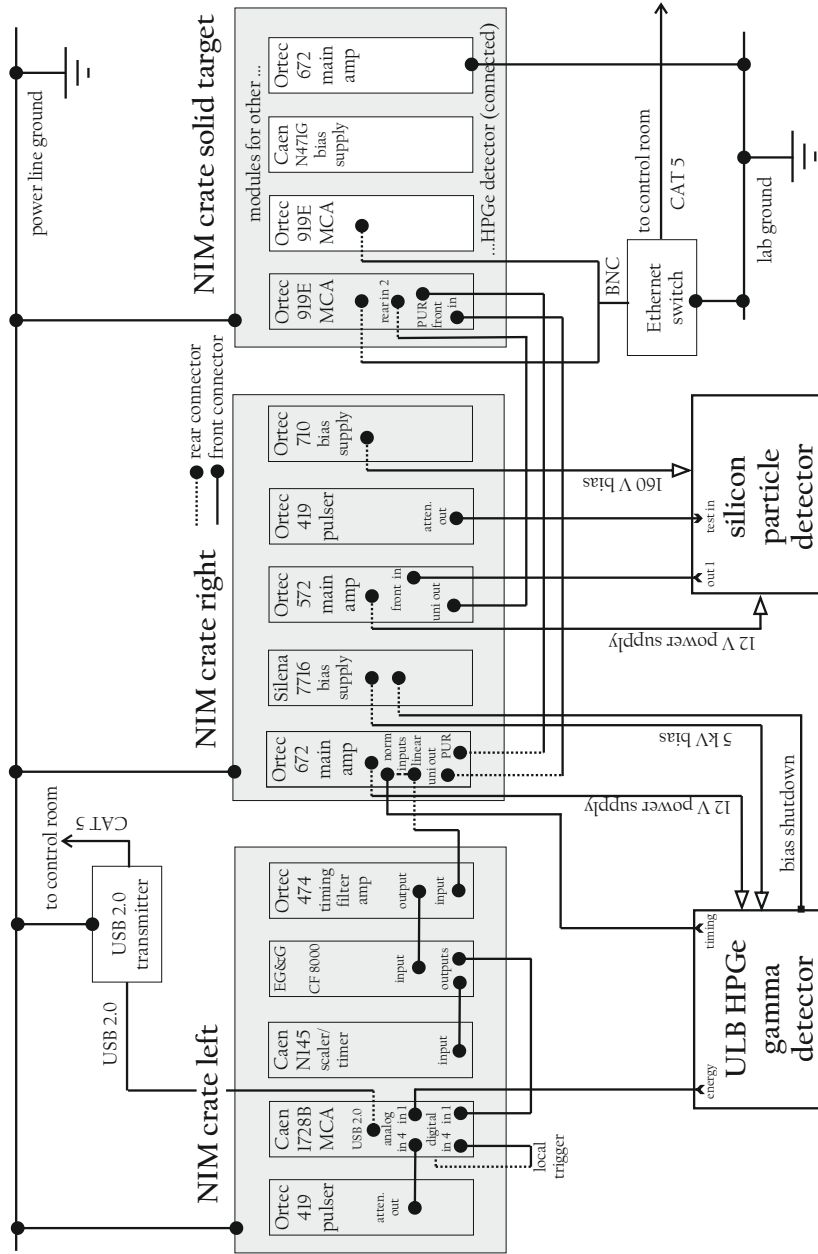
Figure 3.11.: The electronic chain in operation for obtaining data set 1. For the data sets 2 and 3, the Ortec 919E module was moved to the right NIM crate, and the NIM crate of the solid target setup was taken out. The Silena 7716 module was replaced by a Caen bias supply. The BNC-to-Ethernet switch was connected to the common power line ground then, to remove a potential source of electronic noise.

In the analog branch, pile up rejection signals were provided by the Ortec 672 main amplifier and passed to the Ortec 919E MCA. The spectra were saved hourly by running a job script on the Maestro software.

All crates were electrically isolated from their support and connected to the same power line ground to avoid mass loops. Anyway, some mass loops remained. The Caen module was connected via USB 2.0-to-Ethernet-converters to the PCs in the control room, which were supplied by a different power line. Similarly, a second converter connected the Ortec 919E BNC-network with the laboratory ethernet. Hence, contact with different ground potentials could not be avoided. In addition, several times high frequency noise (in the MHz range) or white noise has been observed, affecting the trigger rate and the dead time. Strong noise on the power line (or on its grounding) is believed to be the reason for these effects, because it appeared randomly in time and length.

Under normal conditions, the γ-event rate was low even at high beam intensities, about 2.2 counts/s in average at $360\,\mu$A of beam current and at a gas target pressure of 0.3 mbar. From this, a negligible dead time can be expected, but was nevertheless measured to exclude unforeseeable effects. Ortec 419 modules delivering pulses with a well-calibrated frequency of 70 Hz were connected to the test inputs of the preamplifiers. In case of the HPGe γ-detector, the measured dead time has been $0.0\,\%$ when any noise was absent. The spectra obtained from the silicon detector had a typical dead time of about $10\,\%$ under optimal conditions, already affected by electronic noise which was always present.

3.3.3. Definition of the ^{2}H(α,γ)^{6}Li regions of interest

It is now necessary to define the ^{2}H(α,γ)^{6}Li regions of interest for all used beam energies. The expected γ-energy is given by

$$E_\gamma = Q + \frac{m_d}{m_\alpha + m_d}E_\alpha - \frac{E_\gamma^2}{2\,m_{^6\mathrm{Li}}\,c^2} + \frac{v_{^6\mathrm{Li}}}{c}E_\gamma\,cos\theta \qquad (3.10)$$

according to [8]. The first term is the Q-value of the ^{2}H(α,γ)^{6}Li reaction, $Q = 1473.8$ keV (using data from [13]). The second term represents the reaction kinematics, accessorily corrected by the third term which represents energy carried away by the recoiled ^{6}Li nucleus. This correction is small ($0.22...0.23$ keV), and in order to simplify the calculation, a value for E_γ, calculated from the first two terms only, is used. The same has been done also in the fourth term introducing the Doppler shift of the γ-rays emitted by the recoiled ^{6}Li nucleus moving with the velocity $v_{^6\mathrm{Li}}$. The detector is very close to the comparably long target, so the range of the angle θ between the detector and the recoiled nucleus is broad ($10°...170°$). The absolute value for the Doppler correction is almost equal for both extreme cases (up to 15.5 keV), but the sign changes, the correction becomes negative towards the beam stop, and

the energy loss of the beam reduces the γ-energy further by 1 keV. This is the reason for an exceptional broadening of the ^{2}H$(\alpha,\gamma)^6$Li signal, reaching a width of up to 31 keV.

An additional broadening is necessary to allow for the energy resolution of the HPGe detector. The available sorted spectra have a typical energy resolution of less than 3 keV (FWHM) in the interesting energy range around 1.6 MeV. The calculated ^{2}H$(\alpha,\gamma)^6$Li regions of interest are thus extended by 1.5 keV on the low- and on the high-energy side to make sure to have the full signal included. Finally, the ^{2}H$(\alpha,\gamma)^6$Li regions of interest are defined as follows:

E_{beam} (keV)	Terms 1+2 (keV)	Term 3 (keV)	Term 4 (keV) +	Term 4 (keV) -	v/c ($\times 10^3$)	Extended ROI (keV)
400	1607.7	- 0.23	15.3	16.4	9.8	1589.5 ... 1624.5
360	1594.4	- 0.23	14.4	15.5	9.3	1577.0 ... 1610.5
280	1567.6	- 0.22	12.5	13.5	8.2	1552.0 ... 1581.5
240	1554.2	- 0.22	11.5	12.5	7.6	1539.5 ... 1567.0

Table 3.4.: Calculation of the adopted ^{2}H$(\alpha,\gamma)^6$Li regions of interest. The used spectra have a bin width of 0.5 keV, so some ROIs have been extended by more than 1.5 keV to match the next bin edge.

3.4. Energy resolution and detection efficiency of γ-rays

The availability of list mode data allowed to discard parts of data which were affected by electronic noise or high trigger rates, or to discard times when there was no beam on target. The gained "clean" γ-spectra obtained from the Caen1728B digitizer module along with its Java-based PC software are used for the data analysis.

A single aquired γ-spectrum of one run contains between a few hours and several days of continuous measurement. Whenever a malfunction in the LUNA2 accelerator or in another system occurred, the data acquisition system was manually stopped and restarted. Hence, a data set is always the sum of several γ-spectra. Such a data set represents a measurement period of several weeks with almost continuous operation. The data sets are further described in section 3.6.3.

The energy calibration has been very stable in time. However, the single γ-spectra were cut into slices of similar time, all of them calibrated independently using the JSpecView software. The events were sorted into bins with a width of 0.5 keV. Then, all single spectra of a particular run were added to a sum spectrum. The achieved energy resolution is good (still not as good as warranted in the data sheet), and the characteristics of both data acquisition branches are compared in table 3.5.

The γ-energy resolution has been compared for several distinct, Gaussian-shaped

Data set	FWHM (keV)			
($E_{\text{beam}} = 400\,\text{keV}$)	198.4 keV	669.9 keV	1547.1 keV	2614.5 keV
1, digital	1.9	2.1	2.6	3.5
1, analog	3.5	3.6	4.6	4.6
2, digital	1.8	1.9	2.8	3.5
combined 1+2, digital	1.9	2.0	2.8	3.5

Table 3.5.: The γ-energy resolution of the data aquisition systems compared for several single, Gaussian-shaped peaks.

γ-lines along the spectrum. Sum spectra of the analog branch have been prepared similarly as described above, using the Maestro software for the energy calibration and a small rebinning tool. Data affected by electronic noise could not be excluded. The peaks were fitted with a Gaussian function described in [36] and modified adding an offset parameter N_0:

$$N(E_\gamma) = N_0 + \frac{A}{\sigma\sqrt{2\pi}}\exp\left(-\frac{(E_\gamma - E_0)^2}{2\sigma^2}\right) \qquad (3.11)$$

The FWHM (full width half maximum) value was then determined via

$$\text{FWHM} = 2.35\,\sigma \qquad (3.12)$$

The peak at 1547.1 keV is inside the ^{2}H(α,γ)^{6}Li region of interest, so the assumption of an energy resolution of below 3 keV in this energy range is justified.

The full-energy peak γ-detection efficiency has been measured with nearly point-like radioactive sources moved along the beam path. Apart from ^{60}Co and ^{137}Cs, an ^{88}Y source has been used because it emits γ-rays with an energy above the ^{2}H(α,γ)^{6}Li regions of interest (E_γ=1836 keV), so an interpolated detection efficiency can be determined. Before doing so, the measured counting rates have to be corrected for the true-coincidence summing effect, as the sources were placed very close to the detector. A precise efficiency measurement is very important, because its error contributes directly to the final S-factor uncertainty.

Source	$E_{\gamma,1}$ (keV)	$I_{\gamma,1}$ (%)	$E_{\gamma,2}$ (keV)	$I_{\gamma,2}$ (%)	Data
^{60}Co	1172.2	99.85	1332.5	99.98	[37]
^{88}Y	898.0	93.7	1836.1	99.2	[38]

Table 3.6.: Sources used for measuring the full peak γ-detection efficiency along with emitted γ-rays and intensities I_γ.
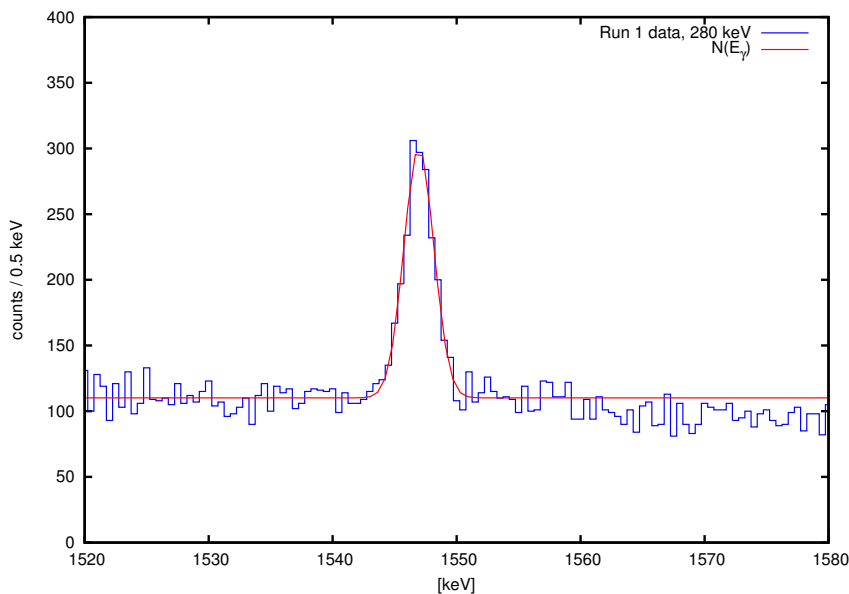
Figure 3.12.: Gaussian fit of the peak at 1547.1 keV due to the ^{63}Cu(n,n'γ) interaction, using the run 1 data set obtained at a beam energy of 280 keV with the digital data aquisition branch.

True-coincidence summing occurs if a nuclide emits several γ-rays in a cascade, and if two or all of them interact with the detector volume at the same time. The HPGe detector is not able to resolve time differences in the picoseconds range, so the energy deposited by two or more coincident γ-rays is summed up. The particular γ-rays, although detected, do not appear in their respective full-energy peaks, but elsewhere in the spectrum, so a correction is needed. This is not necessary in case of emission of single γ-rays (662 keV, ^{137}Cs) or if a big distance between source and detector makes it unlikely that two simultaneously emitted γ-rays reach the detector volume.

The ^{60}Co and the ^{88}Y sources emit γ-rays from a cascade and are therefore subject to true-coincidence summing corrections: Without the occurrence of true-coincidence summing, the counting rate in the full-energy peak of γ-ray 1 is given by

$$n_{\gamma,1} = A \times I_{\gamma,1} \times \epsilon(E_{\gamma,1}) \tag{3.13}$$

where A is the activity of the source, and $\epsilon(E_{\gamma,1})$ is the true full-energy detection efficiency at the given γ-energy [39]. In case of summing effects, the counting rate in the full-energy peak is reduced, and can be assumed as

$$n_{\gamma,1}^* = A \times I_{\gamma,1} \times \epsilon(E_{\gamma,1}) \times [1 - \epsilon_{\text{tot}}(E_{\gamma,2})] \tag{3.14}$$

35
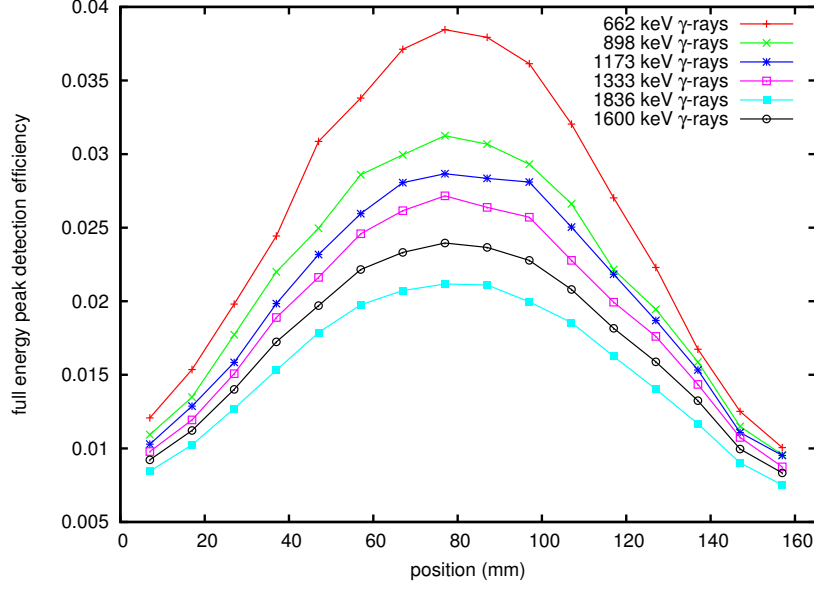
Figure 3.13.: Measured (and, in case of 1600 keV γ-rays, interpolated) full energy peak detection efficiencies. The position $x = 0$ is located at the tip of the target collimator.

where $\epsilon_{\text{tot}}(E_{\gamma,2})$ is the total detection efficiency of γ-ray 2, including full detection or partical energy deposition through Compton scattering or pair production. The counting rate in the full-energy peak of γ-ray 2 is calculated similarly via

$$n_{\gamma,2}^* = A \times \epsilon(E_{\gamma,2}) \times [I_{\gamma,2} - I_{\gamma,1} \times \epsilon_{\text{tot}}(E_{\gamma,1})] \tag{3.15}$$

taking into account that the emission of γ-ray 2 is not necessarily preceded by the emission of γ-ray 1. Hence, correction factors c_i are obtained with

$$c_1 = \frac{n_{\gamma,1}}{n_{\gamma,1}^*} = \frac{1}{1 - \epsilon_{\text{tot}}(E_{\gamma,2})} \ \text{ and } \ c_2 = \frac{n_{\gamma,2}}{n_{\gamma,2}^*} = \frac{I_{\gamma,2}}{I_{\gamma,2} - I_{\gamma,1}\,\epsilon_{\text{tot}}(E_{\gamma,1})} \tag{3.16}$$

A remaining problem are the unknown single total detection efficiencies, as other γ-rays contribute to the spectrum. The following approximations are employed, with a conservatively estimated error of 20 %:

$$1. \ \epsilon_{\text{tot}}(898\,\text{keV}) = \epsilon_{\text{tot}}(662\,\text{keV})\frac{\epsilon(898\,\text{keV})}{\epsilon(662\,\text{keV})} \tag{3.17}$$

$$2. \ \epsilon_{\text{tot}}(1836\,\text{keV}) = \epsilon_{\text{tot}}(1332\,\text{keV})\frac{\epsilon(1836\,\text{keV})}{\epsilon(1332\,\text{keV})} \tag{3.18}$$

$$3. \ \epsilon_{\text{tot}}(1173\,\text{keV}) = \epsilon_{\text{tot}}(1332\,\text{keV}) = \frac{N_{\text{tot,Co-60}}}{2\,t_{\text{acq}}\,A_{Co-60}} \tag{3.19}$$

The true-coincidence summing correction amounts up to $13\,\%$ in case of ^{60}Co if the source is placed right above the detector head. Finally, the true full-energy detection efficiency for a specific γ-ray is obtained with

$$\epsilon(E_\gamma) = c\frac{n_\gamma}{A \times I_\gamma} \tag{3.20}$$

This correction has been done for all sources and positions along the beam path, and the results are plotted in figure 3.13. The value for γ-rays inside the ^{2}H$(\alpha,\gamma)^6$Li region of interest is still unknown yet and has to be calculated by interpolation. It is assumed that the energy dependence of the full-energy detection efficiency can generally be described by

$$\epsilon(E_\gamma) = A + B \times E_\gamma^{-2} \tag{3.21}$$

This function is used to fit the existing data points at all positions and to calculate the function value for $E_\gamma = 1.6\,\text{MeV}$. The results are plotted in figure 3.13 as well. The average full-energy peak detection efficiency amounts to $\bar{\epsilon}(1.6\,\text{MeV}) = 1.71\,\%$.

The different uncertainties (source activity, counting statistics and $20\,\%$ on the total detection efficiencies) are propagated, and the final uncertainties are half of the $68\,\%$ confidence band around the best fit function at $1.6\,\text{MeV}$.

3.5. The shielding

The main component of the shielding is given by the location: The LUNA facility is located at Laboratori Nazionali del Gran Sasso (LNGS), a deep unterground laboratory with a shielding of $3800\,\text{m}$ water equivalent against cosmic radiation. The flux of cosmic muons is reduced to a negligible influence compared to local sources of radiation [40].

The HPGe γ-detector has to be protected from environmental γ-rays during the measurement, emitted by ^{40}K and isotopes of the ^{238}U and the ^{232}Th decay chains in the dust and surrounding walls and from ^{222}Rn in the air. The very low background rates measured in a previous LUNA gas target setup [41] with the same detector could not be achieved anymore due to several necessary changes.

The main component of the shielding was a massive lead castle covering nearly 4π of solid angle with at least $20\,\text{cm}$ of selected lead (^{210}Pb activity of 25 Bq/kg Pb) instead of the previous thickness of $30\,\text{cm}$. The purpose for this decrease was to free space for the additional neutron shielding, consisting of a $10\,\text{cm}$ layer of borated polyethylene on the side walls. This layer was part of an anti-radon box, which was closed by leafs of acrylic glass on the front and on the back side and a massive top cover of borated polyethylene (see figures 3.3 and 3.15). A continuous flow of nitrogen
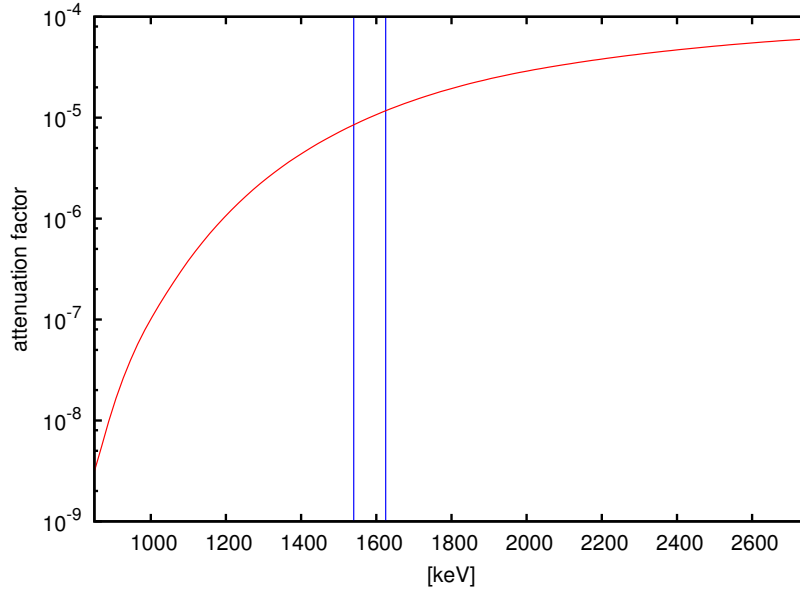
Figure 3.14.: γ-ray attenuation factors of the lead shielding, with 20 cm of thickness, using XCOM data [42]. The ^{2}H$(\alpha,\gamma)^6$Li region of interest is marked by two lines.

gas, evaporated from a Dewar vessel filled with liquid nitrogen, was supplied through a pipe directly below the detector head inside the lead castle, to keep any ^{222}Rn out.

Previously, the inner shielding had consisted of very pure copper, to stop γ-rays emitted by contaminations on the surface of the lead bricks and the decay of ^{210}Pb, but the copper had to be replaced by polished lead bricks. The first measurements had shown that a strong ^{65}Cu(n,n'γ) line touches the ^{2}H$(\alpha,\gamma)^6$Li region of interest, so all copper was removed, apart from the hull of the HPGe detector.

In figure 3.16, the laboratory background obtained overground is compared to the laboratory backgrounds measured in two LUNA gas target setups. Inside the ^{2}H$(\alpha,\gamma)^6$Li region of interest, the background rate in the present setup is more than one order of magnitude lower than in a clean, radon-protected lead castle overground, but still one order of magnitude larger than in the previous ^{3}He$(\alpha,\gamma)^7$Be setup. ^{214}Bi lines indicate the presence of ^{222}Rn, and ^{40}K and ^{208}Tl lines a contamination with dust. Further details about the time stability and composition of the laboratory background are written in section 4.1.

The purpose of the neutron shielding was not to stop the very few environmental neutrons which are present at LNGS. (α,n) reactions or the fission of ^{238}U are the only sources of the neutron flux, which amounts to less than $6 \times 10^{-6}\,\mathrm{cm}^{-2}\,\mathrm{s}^{-1}$, $E_\mathrm{n} = 0.025\,\mathrm{eV}...10\,\mathrm{MeV}$ [43]. It is many orders of magnitude below the neutron flux
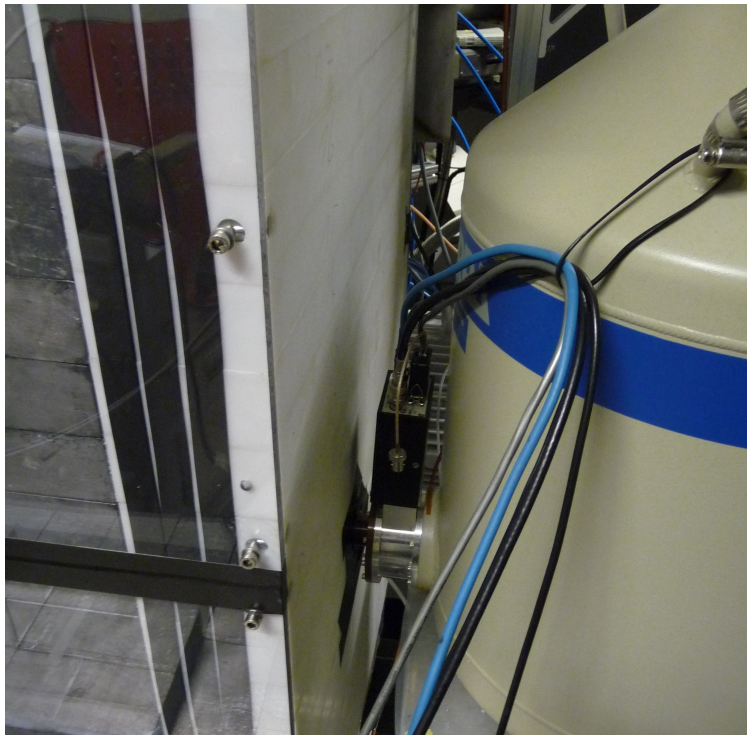
Figure 3.15.: A detail of the anti-radon box. The transparent acrylic glass is
tightly fixed to the borated polyethylene. Three neoprene tapes
ensure the gas tightness. The cold finger of the HPGe detector is
fed through the side wall.

that has been generated during the ^{2}H(α,γ)^{6}Li measurements at the LUNA site. To
not affect neighbouring ultra-low background experiments, the LUNA neutron rate
was restricted to a maximum of 10 neutrons per second, which was the actual reason
for the additional neutron shielding. The neutron rate was measured and controlled
in two ways which gave similar results:

- Evaluation of the triangular 692 keV ^{72}Ge(n,n'γ) peak in the beam induced
  background measured by the HPGe detector according to [36].

$$\Phi_{\mathrm{n}} \left[\frac{\text{neutrons}}{\text{cm}^2} \right] = \frac{300 \times (692\,\text{keV peak content})}{\text{HPGe active volume } [\text{cm}^3]} = 0.59 \times N_{692} \qquad (3.22)$$

- The measured rate of protons in the silicon detector was compared with a
  simulated proton rate. From this, the neutron rate inside the entire target can
  be derived. The simulation is based on Geant3 and has been developed at INFN
  Genova.
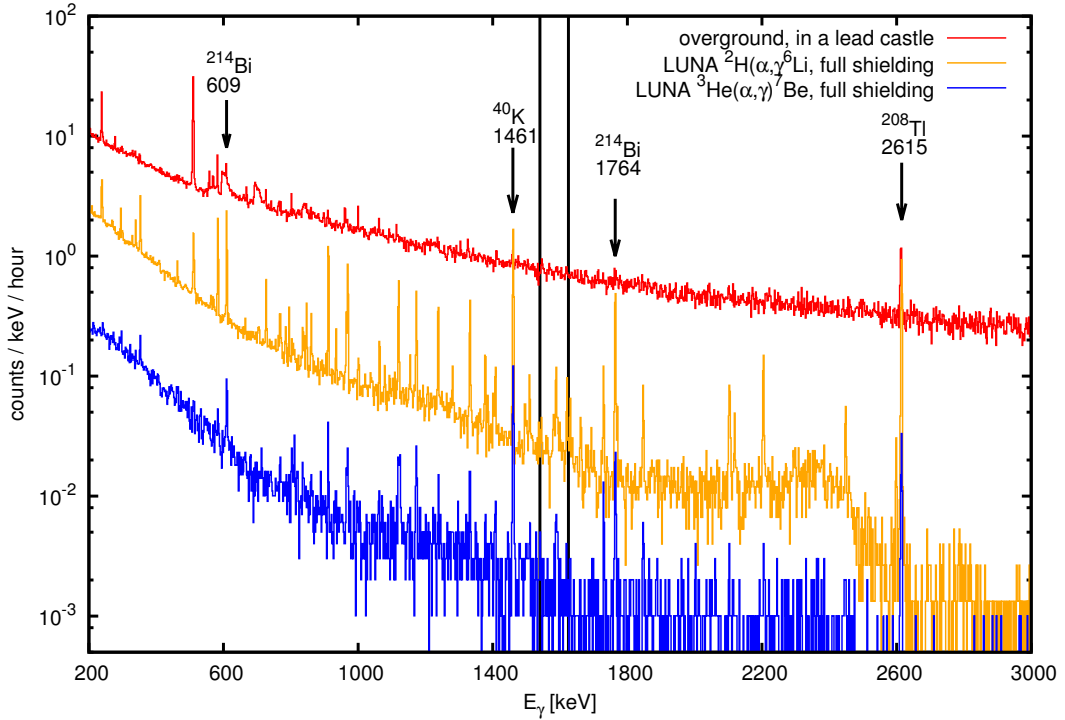
Figure 3.16.: A laboratory background spectrum obtained overground compared
with the LUNA laboratory background deep underground. All se-
tups had a radon protection. The ^{2}H$(\alpha,\gamma)^6$Li region of interest is
marked by two black lines.

3.6. Measurement timeline

3.6.1. The setup development until the end of 2009

After the discovery of an unexpectedly large ^{6}Li abundance in metal-poor halo stars
by Asplund et al. [4] and the challenging task to extract a correct S-factor from the
high-energy Coulomb dissociation data obtained at the GSI, the possibility to mea-
sure the S-factor directly deep underground at LUNA was discussed inside the col-
laboration in June and July 2007. The gas target setup of the previous ^{3}He$(\alpha,\gamma)^7$Be
experiment was still mounted and well understood, and first studies using the pre-
liminary results of the GSI group were promising that a measurement at LUNA
is feasible. First test measurements in November 2007 revealed the presence of a
strong beam-induced background due to neutrons from the ^{2}H$(^2$H,n$)^3$He reaction.
Furthermore, the large amounts of copper close to the HPGe detector generated high
Cu(n,n'γ) peaks also in the expected ^{2}H$(\alpha,\gamma)^6$Li region of interest.

Several ideas to solve the problems were discussed until spring 2009, such as the use of a solid instead of a gaseous target, and experimentally studied, such as surrounding the beam path with a steel pipe to stop scattered deuterons. The latter improved the situation noticeably. Other options turned out to be not favourable:

- Detection of the ^{6}Li nucleus. It is emitted in forward direction, the primary path depends on the angle of the emitted γ-ray. As the target gas is still present, the nucleus is stopped rapidly and removed by the gas flow or deposited on a metal surface. Therefore, measuring the number of ^{6}Li nuclei is not possible.

- A beam of deuterons on a helium target. Accelerating deuterons is possible with the LUNA2 accelerator, but would cause severe problems with neutron radiation. An abundant implantation of deuterons would be caused, on the collimators and on the beam stop, serving as a target for the the ^{2}H(^{2}H,n)^{3}He reaction. As discussed in section 4.2, a high, non-controllable flux of neutrons would be the result.

- A solid instead of a gaseous deuterium target. This option is disfavoured due to the stopping of the α-beam inside the target: The energy of the α-particle which induces the ^{2}H(α,γ)^{6}Li reaction is not well defined anymore. As the reaction occurs non-resonant with a strong energy dependence here, the beam energy must be known precisely.

The finally applied method - an ^{4}He$^+$-beam on a D$_2$ gas target has some disadvantages as well: The target density is limited for practical reasons, and the geometry (long target, close detector) leads to a high Doppler shift correction, but the measurement is still feasible.

Further modifications to the ^{3}He(α,γ)^{7}Be setup were necessary:

- The copper target chamber was replaced by a shorter steel chamber. Simulations showed, later experimentally verfied, that the beam-induced background rate could be largely reduced by shortening the beam path, while not so much signal was lost.

- The HPGe detector was moved closer to the beam path through a recess in the bottom of the target chamber, to improve the signal-to-noise ratio.

- The inner shielding consisting of pure copper was replaced by lead.

- A silicon detector was introduced to measure the neutron production indirectly.

The studies and experimental tests continued until a final design of the inner parts of the setup was ready in fall 2009. This was the time when the author joined the LUNA collaboration.

3.6.2. Measurement parameter optimization

During the experimental tests, it turned out that scattered deuterons not only produced neutrons in the gas, but were also implanted into metal surfaces, forming additional targets for the ^{2}H(^{2}H,n)^{3}He reaction there. The following questions had to be answered:

- Which gas target pressure is optimal? The boundary conditions were to find the best signal-to-noise ratio while keeping the neutron rate, the implantation effects and the deuterium consumption under control.

- Which is the best beam energy? Again the signal-to-noise ratio should be the optimal, with the expected ^{2}H(α,γ)^{6}Li signal shifted to a low-background region.

To produce a neutron, two deuterons are needed: A first one which is kicked by an incident α-particle, and a second one which is the target for the primary deuteron. Hence, one expects that the beam induced background rate raises with p^2. In contrast, the rate of ^{2}H(α,γ)^{6}Li reactions is proportional to p only, so low target pressures are favoured, also in view of the implantation problem. During November and December 2009 and again in October 2010, the beam induced background rate was studied for several gas target pressures in the range of 0.1...1.0 mbar. Its p^2-dependence could be confirmed (see figures 3.18 and 3.19), but an offset remained, pointing to the presence of a persistent implantation.

To quantify the contribution of implanted deuterons to the accumulated beam induced background N_{total}, the following model was introduced to describe it analytically:

$$N_{\text{total}} = N_{\text{gas}} + N_{\text{imp}} = \sum_{runs} (c\,p^2\,Q + k\,p\,Q) \tag{3.23}$$

with c and k being constants and Q the integrated charge of single runs. In the beginning, one can assume $N_{\text{imp}} = 0$, and the constant c can be determined from the very first run. In practice, this has been impossible, as no reliable data with an unused setup was available. Therefore, a value of $c = 0.15$ has been estimated from the analysis of the first reliable data. Now, the contribution N_{imp} can be calculated via

$$N_{\text{imp,run}} = N_{\text{total}} - c\,p^2\,Q_{\text{run}} \tag{3.24}$$

for every run. The results are plotted in figure 3.17. Surprisingly, the level of implantation does not rise steadily. It appears to be dependent on the target pressure as expected, but drops to a new equilibrium after reducing the target pressure. This effect has been observed again during test measurements in the finalized setup in fall 2010.
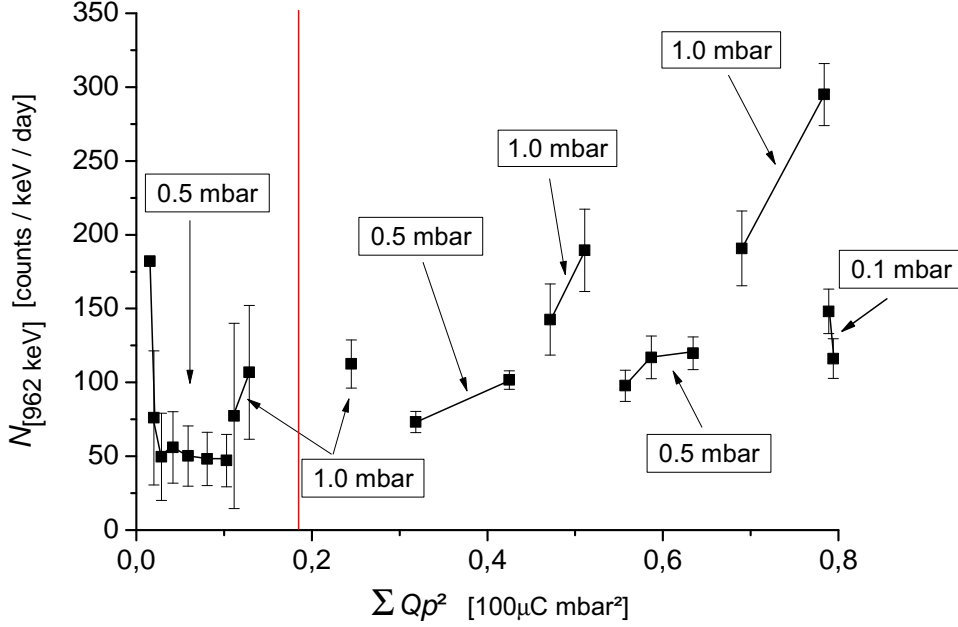
Figure 3.17.: The implantation of deuterium depending on the target gas pressure. The content of the 692 keV ^{72}Ge(n,n'γ) peak is plotted. The measurements were interrupted by one month, this is marked by the red line.

An additional evidence for the presence of implanted deuterium is shown in figures 3.18 and 3.19: The pressure dependence of the beam induced background is fitted best with a second-order polynomial function containing a linear term. The remaining offset is not due to laboratory background (it has been subtracted before), but either due to the remaining implantation even after a complete evacuation of the target, or due to a deuterium layer on metal surfaces which could be removed only by baking them out.

Measuring the ^{2}H(α,γ)^{6}Li cross section at a pressure of just 0.1 mbar was not favourable: The expected signal rate in the γ-detector would have been only 0.6 counts per hour at a beam energy of 400 keV and a beam current of 300 μA. As a compromise, a target pressure of 0.3 mbar was chosen. Even at high beam currents of 360 μA, the neutron rate did not exceed the order of magnitude of 10 neutrons per second, and the implantation-induced increase of the background rate has been about 10% per 100 C of integrated charge (see fig. 3.20) which has been comparably moderate.
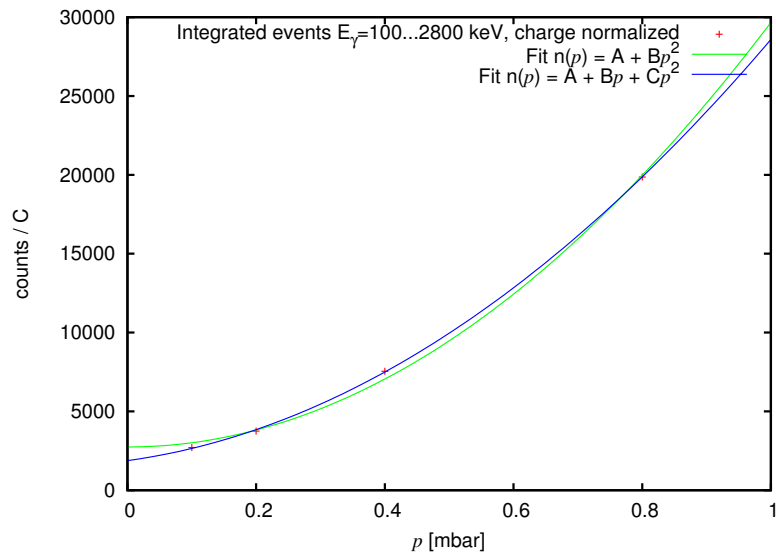
Figure 3.18.: The target pressure dependence of the charge-normalized beam induced background rate of the entire γ-spectrum, obtained at a beam energy of 400 keV.
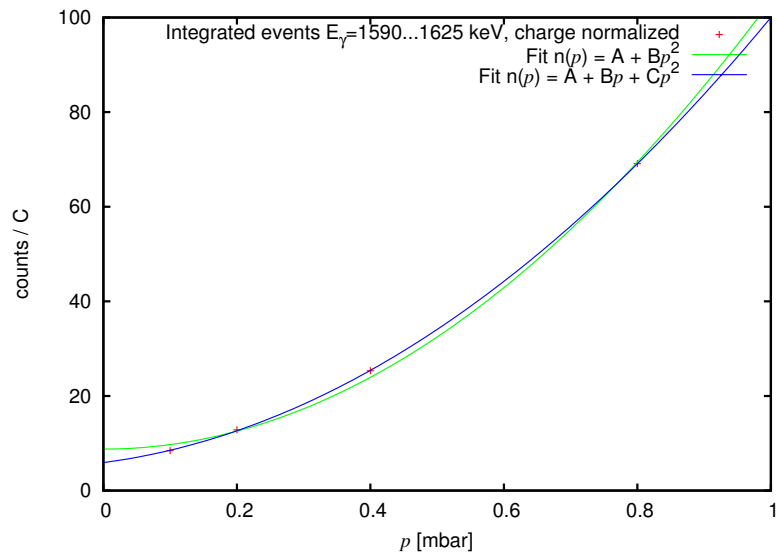
Figure 3.19.: The same as above, but using the charge-normalized beam induced background inside the 400 keV $^2\mathrm{H}(\alpha,\gamma)^6\mathrm{Li}$ region of interest.
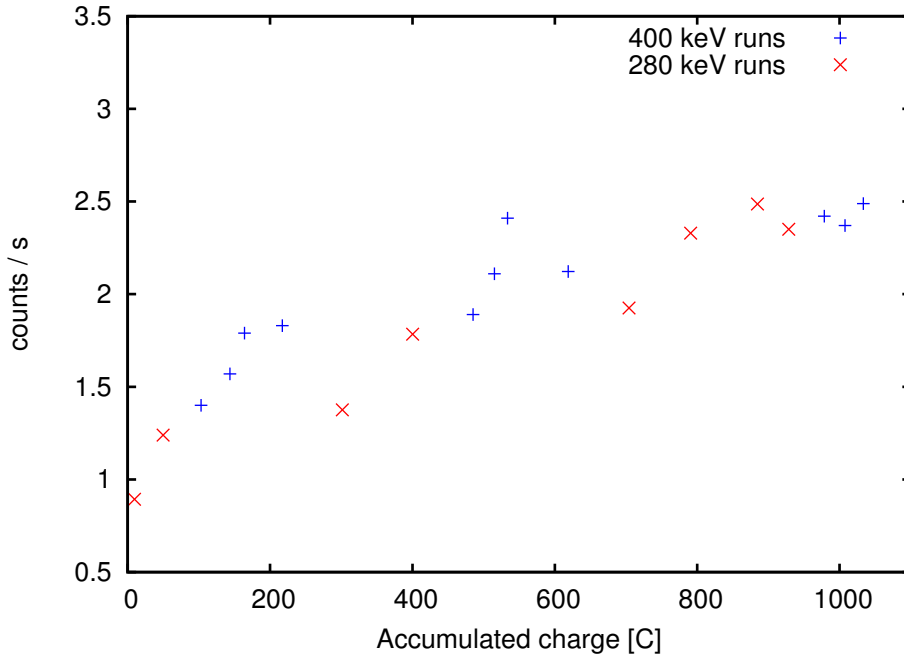
Figure 3.20.: The rising beam induced background rate with increasing accumu-
lated charge (data sets 1 and 2). The rate of events in the HPGe
detector is plotted ($E_\gamma = 0.1...4.0\,\mathrm{MeV}$).

The question of the best beam energy has been answered similarly by experimental
runs at various beam energies and by theoretical considerations. First it turned out
that the beam induced background rate showed no significant difference in the beam
energy range of $360...400\,\mathrm{keV}$. So, the idea has been to optimize the signal-to-noise
ratio. The expected cross section of the non-resonant $^2\mathrm{H}(\alpha,\gamma)^6\mathrm{Li}$ reaction drops
exponentially with lower beam energy, while the region of interest is shifted to lower
γ-energies. In table 3.7 and figure 3.21, several signal-to-noise ratios are shown.

The maximum is reached at a beam energy of $390\,\mathrm{keV}$. Above this value, the signal-
to-noise ratio decreases again, because the $^{65}\mathrm{Cu(n,n'}\gamma)$ line at $1623.4\,\mathrm{keV}$ is more and
more included in the region of interest. However, the highest possible beam energy
has been chosen to avoid including a natural background line ($^{228}\mathrm{Ac}$, $1588.2\,\mathrm{keV}$),
with the possibility to exclude the $^{65}\mathrm{Cu(n,n'}\gamma)$ peak in the data analysis if necessary.

After it turned out that a $^3\mathrm{He}$ beam is not helpful to reproduce the beam induced
background of a $^4\mathrm{He}$ beam, the approach was changed: A low beam energy of $280\,\mathrm{keV}$
ensures that the $^2\mathrm{H}(\alpha,\gamma)^6\mathrm{Li}$ region of interest is shifted to a position where no distinct
γ-lines are present, and where the $400\,\mathrm{keV}$ region of interest is not touched. If the
shape of the beam induced background is independent from the beam energy, a

Beam energy (keV)	Expected signal (counts/C)	^{2}H(α,γ)^{6}Li region of interest (keV)	Noise (counts/C)	S/N ratio
360	1.29	1578.0...1610.5	20.6	0.063
365	1.35	1579.5...1612.0	20.5	0.066
370	1.41	1581.0...1614.0	20.8	0.067
375	1.46	1582.5...1616.0	21.0	0.070
380	1.52	1584.0...1617.5	21.1	0.072
385	1.59	1586.0...1619.5	21.0	0.076
390	1.65	1587.5...1621.0	21.0	0.078
395	1.71	1589.0...1623.0	22.1	0.078
400	1.78	1590.5...1625.0	23.5	0.076
280	0.56	1553.5...1582.0	22.6	0.025

Table 3.7.: Signal-to-noise ratios for various beam energies. The beam induced background in the ^{2}H(α,γ)^{6}Li regions of interest is taken from the combined data set 1+2 at a beam energy of 280 keV, to be sure that no 400 keV signal is included.

γ-spectrum obtained at 280 keV energy can be used to subtract the beam induced background of a 400 keV spectrum. This approach is discussed in chapter 4. These considerations led to the decision to measure at beam energies of 400 keV and 280 keV. To verify the presence of the ^{2}H(α,γ)^{6}Li signal and to gain another data point, the beam energies were changed to 360 keV and 240 keV in a third measurement campaign.

3.6.3. Data taking

In fall 2010, the shielding of the setup had been mounted. Several further modifications were implemented now:

- The steel tube to stop scattered deuterons was lengthened to cover the entire beam path, and a steel ring was mounted on the calorimeter head for the same purpose.

- The silicon detectors were mounted together with their cooling system.

- The data acquisition system was supplemented by the digital Caen N1728B module and completed.

The finalized setup was studied using various beam energies and gas target pressures as described in the previous section. In spring 2011, an unsuccessful test using a ^{3}He beam to reproduce the beam induced background obtained with a ^{4}He beam
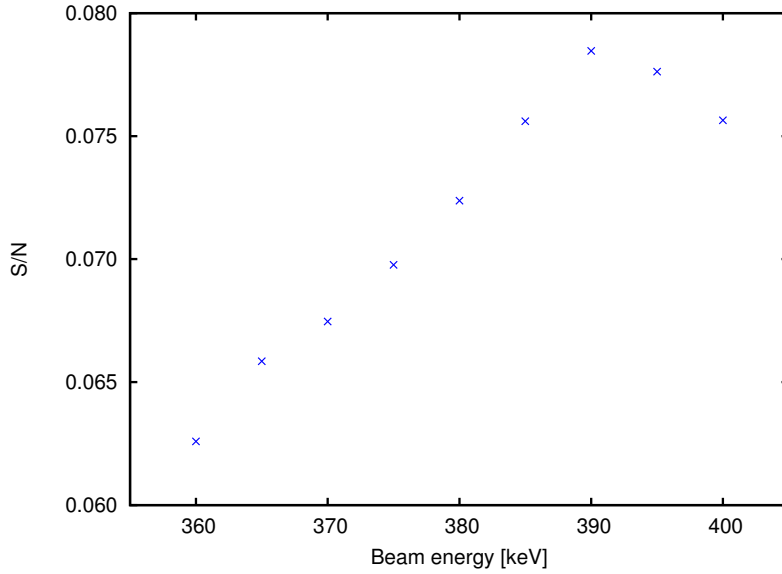
Figure 3.21.: A plot of the data listed in table 3.7.

made it necessary to exchange some activated setup components: Even more energetic neutrons were produced via the ^{2}H(^{3}He,n)^{4}He reaction with a high Q-value. The data taking with the new approach using two different beam energies started soon after. Four data sets are available and listed in the following table:

Name	Obtained in	E_{Beam} (keV)	Charge (Coulomb)	Live time (hours)
Data set 1	spring 2011	400 / 280	256.6 / 278.0	237.4 / 285.7
Data set 2	fall 2011	400 / 280	248.8 / 260.9	200.4 / 205.1
Data set 3	spring 2012	360 / 240	252.7 / 211.5	205.2 / 217.7
Data sets 1+2	(combined)	400 / 280	514.3 / 538.9	437.7 / 490.9

Table 3.8.: Available sets of sorted and summed spectra with their parameters.

During downtimes of the accelerator, all in all 671 hours of laboratory background data in the fully shielded, radon-protected setup were measured. All spectra used for the data analysis are extracted from the Caen N1728B data, sorted and cleaned from noise-affected data as discussed in section 3.4. In the present work, a separation of γ- and neutron-induced events using the rising edge of the preamplifier signals has not been attempted yet, hence the raw γ-spectra measured by the HPGe detector are used.

Four auxiliary measurements were untertaken as well:

- The performance of the Geant4 simulation has been verified by inserting a weak AmBe neutron source into the steel tube for ten hours. This measurement is further described in section 4.2.2.

- The full-energy peak detection efficiency of the HPGe detector has been measured using several radioactive sources (see section 3.4).

- The target gas was replaced by pure dry nitrogen to look for unexpected sources of beam induced background, but the γ-spectra obtained at a 400 keV beam of α-particles showed no deviation from the laboratory background.

After the data taking, the setup was dismounted in May 2012.

3.7. The ^{2}H(^{2}H,n)^{3}He experiment in Dresden

In September 2012, an auxiliary experiment was carried out at the DT-neutron generator facility, operated by the Technical University of Dresden, but housed at the ELBE facility of the Helmholtz-Zentrum Dresden-Rossendorf.

The aim was to accelerate deuterons to an energy similar to the typical energy of kicked deuterons inside the LUNA gas target setup, to reproduce the neutron energy spectrum. Then, the response of a HPGe detector inside such a neutron field should be studied in detail, benefitting from the possibility to reach very good statistics, which was not possible at LUNA due to the neutron rate limitations. The shape of the spectra inside the ^{2}H(α,γ)^{6}Li region of interest has been of special interest.

The tritium source had been replaced by a solid TiD target which has already been used before, so it may have contained at least traces of tritium. It was irradiated by a beam of 325 keV deuterons. The roughly estimated neutron emission rate has been $10^7\,\mathrm{s}^{-1}$ at low beam intensities (according to the operator), so a big distance between source and detector was required. The used HPGe detector had a relative efficiency of 19.3 % and a total active volume of about 90 cm^3. Assuming a distance of 3 m to the source, the neutron flux density at the detector has been $100\,\mathrm{s}^{-1}\,\mathrm{cm}^{-2}$. The evaluated flux density using formula (3.22) was about a tenth of this value.

The energy output of the preamplifier was connected via a very long coaxial cable to the data aquisition electronics in the control room. Similarly to the LUNA setup, an analog branch with an Ortec 671 amplifier and an Ortec 919E multichannel analyzer was used in parallel to the Caen N1728B digital module, but without the pile up rejection mechanism based on the timing signal analysis.

The measured laboratory background already showed a noticeable neutron flux. At the time of the measurement, strong AmBe and ^{252}Cf neutron sources were stored

in the same room. With beam on target, the Maestro dead time estimated by GammaVision reached a value of 8 %. First a spectrum was measured with the uncovered HPGe detector. In a second step, the same materials as in the LUNA setup were placed around the detector head: Lead, steel and copper, and the measurement was repeated.
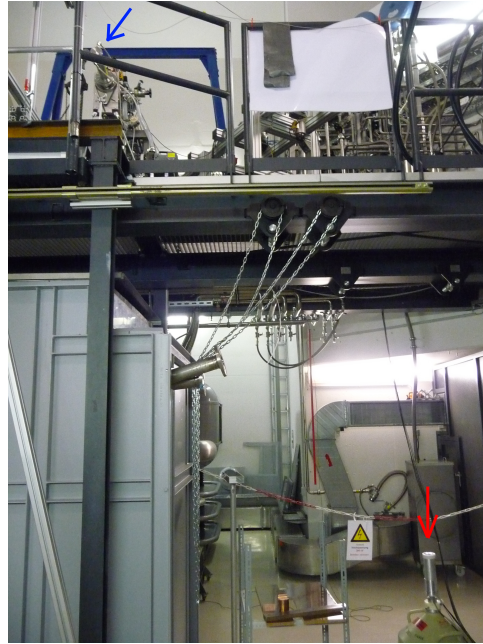
Figure 3.22.: Photo of the setup at the Dresden DT-neutron generator. The source is marked by a red arrow, the HPGe detector by a blue one.

In a last step, the HPGe detector was replaced by a bigger (100 % relative efficiency), segmented HPGe detector. The very high event rate led to a strong distortion of the measured spectrum, which was not usable for this reason. For a certain time, the waveforms were recorded by the digital Caen module, to possibly analyze the rising edges of the signals later.

I turned out that the neutron energy spectrum in Dresden is largely affected by high-energy $^3H(^2H,n)^4He$ neutrons due to the residual tritium content in the used TiD target, and the shapes of spectra obtained at LUNA and in Dresden can hardly be compared. Of certain interest is the occurrence of a ^{57}Fe line at 1612 keV due to neutron capture of ^{56}Fe, confirmed by corresponding high-energy γ-lines at 7.1 MeV. There is no visible peak at 1612 keV in the LUNA spectra, but as the setup contains large amounts of steel, this line is subject to a detailed discussion in section 4.4.4.
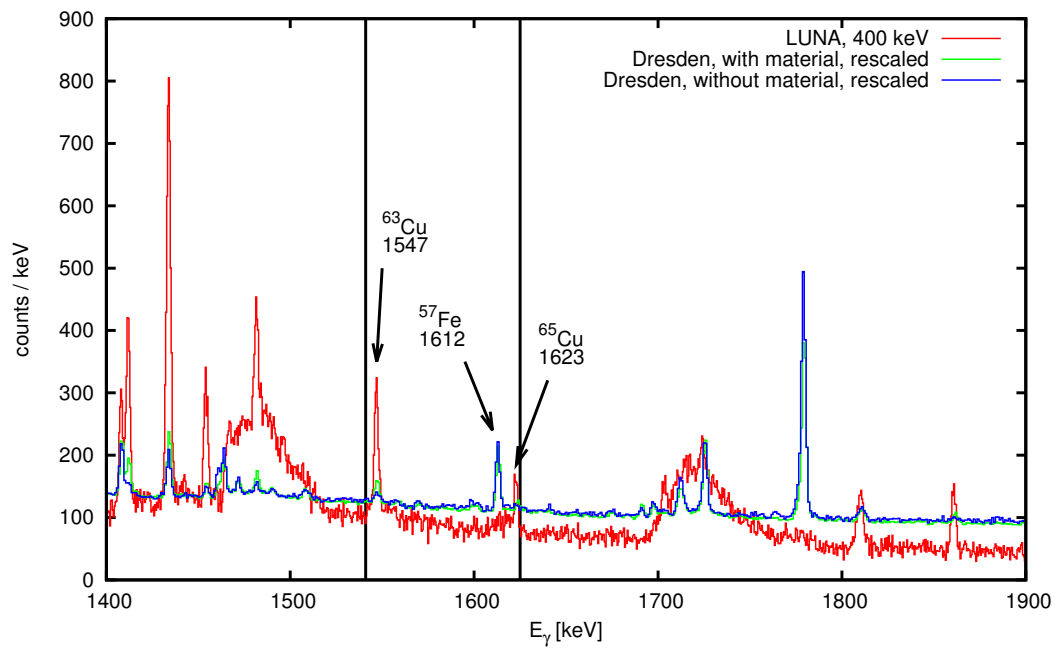
Figure 3.23.: A comparison of the spectra obtained at LUNA and in Dresden, close to the ^{2}H$(\alpha,\gamma)^6$Li regions of interest which are marked by two black lines.
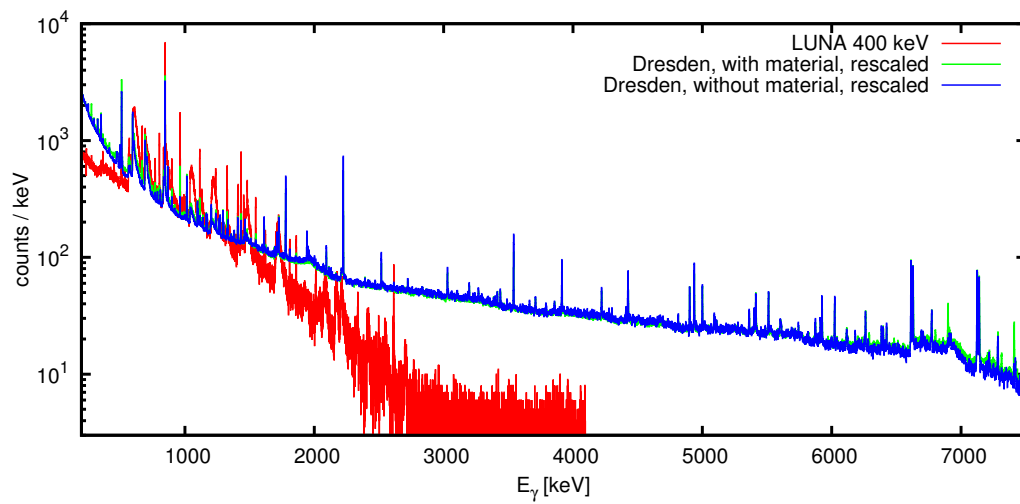
Figure 3.24.: As above, but the entire γ-spectra.

4. Data Analysis

In this chapter, the analysis of the measured γ-spectra is described, especially how the ${}^2\mathrm{H}(\alpha,\gamma){}^6\mathrm{Li}$ yield can be extracted, and how its uncertainty is estimated.

4.1. The laboratory background

Also without the beam on the gas target, the HPGe detector receives a number of γ-rays coming from the decay of natural radioactive nuclei inside and around the setup, even with a shielding surrounding the detector. This laboratory background has to be subtracted from the spectra aquired during the measurement with beam. The reason is mainly, that the amount of beam induced background and especially the ${}^2\mathrm{H}(\alpha,\gamma){}^6\mathrm{Li}$ yield depend on the beam charge, but the laboratory background is time-dependent only. The subtraction of this background is necessary to exclude the time-dependence from the data analysis. In order to subtract the laboratory background properly, it is necessary to understand its composition, especially in the ${}^2\mathrm{H}(\alpha,\gamma){}^6\mathrm{Li}$ region of interest, and to verify its time stability.

The sources of radiation are already briefly described in section 3.5. In figure 4.1, the most prominent γ-lines inside and above the ${}^2\mathrm{H}(\alpha,\gamma){}^6\mathrm{Li}$ region of interest are marked along with the emitting nuclides. A complete list of laboratory background sources is given in table 4.1 along with their supposed origin. The list contains also non-natural sources of γ-rays. After the ${}^3\mathrm{He}$ beam experiment (see section 3.6.3), parts of the target chamber remained activated after (p,n) and (n,p) reactions on its material (steel AISI 304: 18 % Cr, 10 % Ni and 72 % Fe). Although the activity of Co and Mn nuclides is low, their γ-lines are clearly visible in the low-background setup. The half lives of ${}^{56}\mathrm{Co}$ (77 d) and ${}^{54}\mathrm{Mn}$ (312 d) are in the range of the measurement duration, so their decay could cause an erroneous subtraction of the laboratory background.

In the present case, this error can be assumed as being negligible, since the laboratory background has been aquired usually between the single in-beam measurements, whenever the accelerator was not running. Furthermore, the artificial γ-lines above the ${}^2\mathrm{H}(\alpha,\gamma){}^6\mathrm{Li}$ region of interest have a very low counting rate.
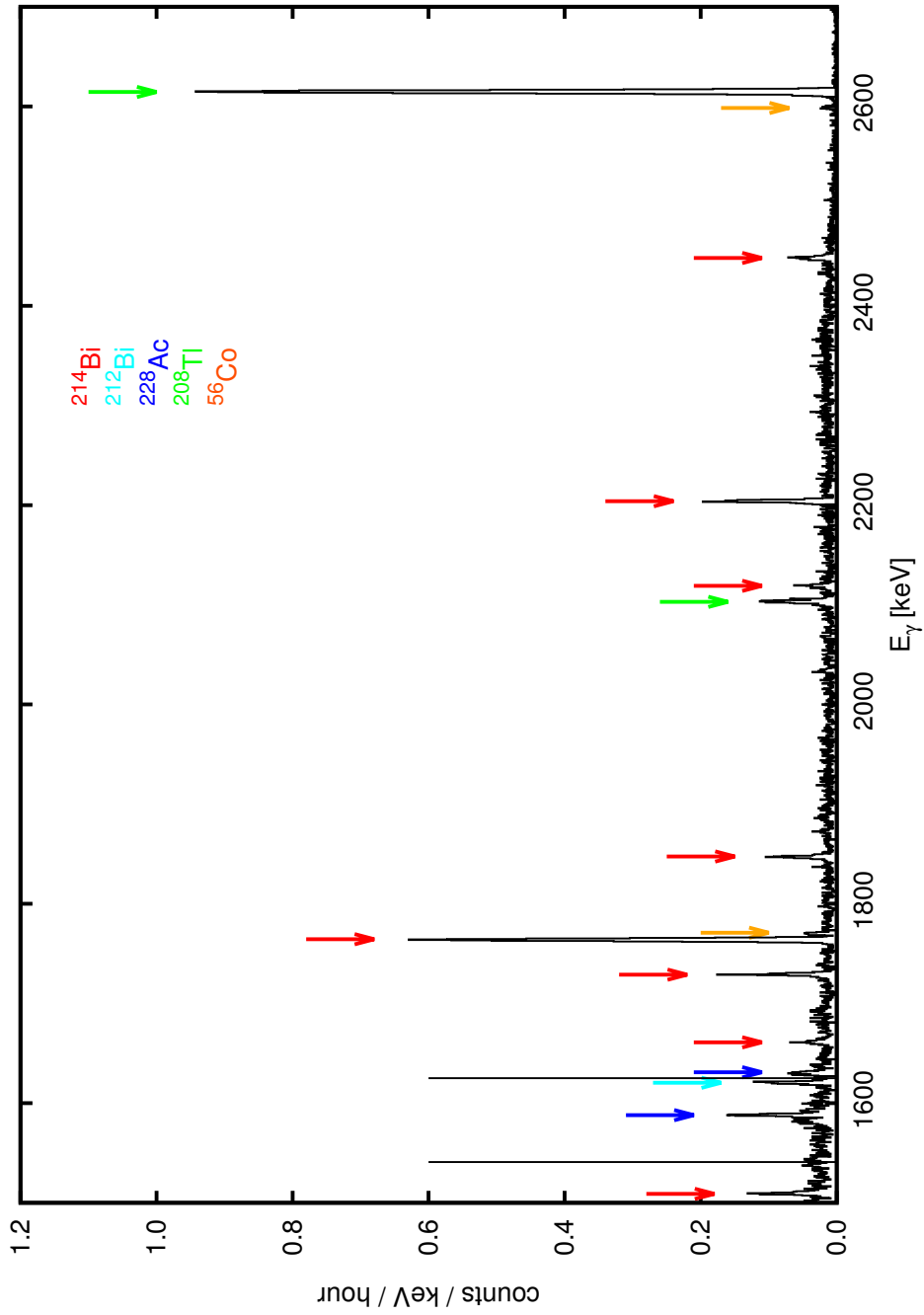
Figure 4.1.: The laboratory background inside and above the ^{2}H$(\alpha,\gamma)^6$Li region of interest which is marked by parallel black lines. The arrow color of a marked γ-line indicates its source. This spectrum contains the total amount of statistics (data sets 1-3, 671 hours).

Nuclide	Prominent lines (keV)	Decay chain	Origin
^{40}K	1461		dust contamination
^{54}Mn	835		setup activation
^{56}Co	847, 1238, 2599, 3202, 3253		setup activation
^{60}Co	1173, 1333		setup activation
^{208}Tl	583, 861, 2615	^{232}Th	dust contamination
^{212}Bi	1621	^{232}Th	dust contamination
^{212}Pb	239	^{232}Th	dust contamination
^{214}Bi	609, 1120, 1238, 1765, 2204	^{238}U	radon decay
^{214}Pb	295, 352	^{238}U	radon decay
^{228}Ac	795, 911, 969, 1588, 1630	^{232}Th	dust contamination

Table 4.1.: List of observed γ-lines in the laboratory background.

The LUNA laboratory has no clean room characteristics, and dust falling from the ceiling is present. It was impossible to avoid that some dust contaminated the setup, especially during the construction of the lead shielding or maintenance works. Furthermore, the used lead bricks were not cleaned before being mounted (apart from the innermost layer surrounding the detector), and all of them had been stored unprotected on the floor before. Hence, there is a persistent contamination of uranium, thorium and potassium inside the setup, contributing a stable, continuous γ-background. Both distinct γ-lines inside the ^{2}H$(\alpha,\gamma)^6$Li region of interest (^{228}Ac, 1588 keV and ^{212}Bi, 1621 keV) are of this type and can be subtracted well after time normalization. The same is true for the comparably strong γ-line at 2615 keV (^{208}Tl).

The gaseous nuclide ^{222}Rn ($T_{1/2} = 3.8$ d) is an interstage product of the ^{238}U decay chain, and can enter or leave the setup before its decay due to its long half life. One of its daughter nuclides, ^{214}Bi, emits several γ-lines with energies above 1.7 MeV, so their Compton continua influence the ^{2}H$(\alpha,\gamma)^6$Li region of interest directly. The amount of ^{222}Rn inside the setup is strongly dependent on the gas tightness of the anti-radon box and on the nitrogen flushing and could be subject to changes in time (see the comparison of different levels of radon protection in figure 4.2). Therefore, it has to be confirmed that also this non-stationary contribution to the laboratory background is stable in time.

In table 4.2, different counting rates of laboratory background are compared for all data sets. Especially inside the ^{2}H$(\alpha,\gamma)^6$Li region of interest, the laboratory background rate has been stable in time during the measurements, and no systematic errors due to an erroneous subtraction from the measured in-beam spectra have to be expected. Figure 4.3 shows the values for single measurements obtained in 2011, also underlining the stability of the contamination and the anti-radon protection.

In the following analysis, a summed γ-spectrum for each data set is used. The
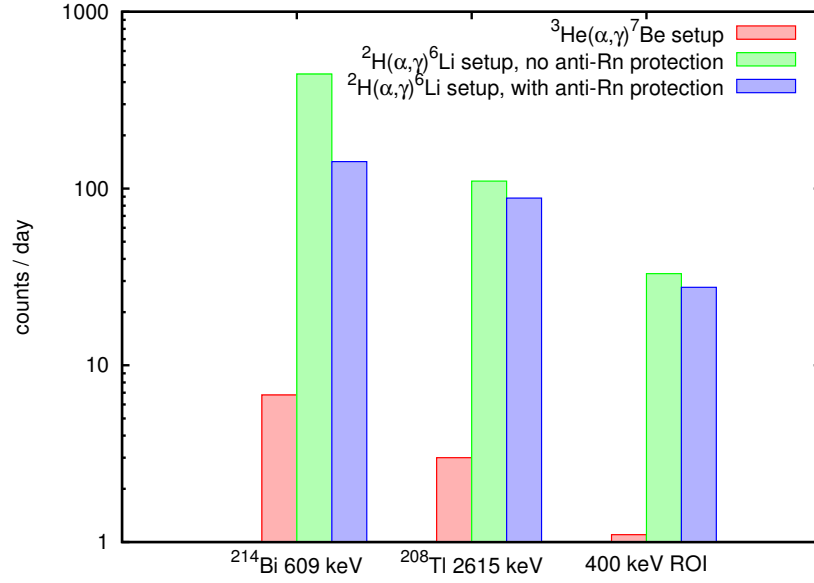
Figure 4.2.: The effects of the quality of the shielding on the laboratory background.

corresponding time-normalized laboratory background has been subtracted in all cases bin-wise according to

$$N_{i,\text{ds,subtr}} = N_{i,\text{ds,raw}} - \frac{t_{\text{lbg}}}{t_{\text{beam}}} N_{i,\text{ds,lbg}} \tag{4.1}$$

for each bin i using clean summed laboratory γ-background spectra of each data set.

Data set	Statistics (hours)	Counting rates		
		200...4000 keV keV^{-1} h^{-1}	1541...1625 keV keV^{-1} h^{-1}	1590.5...1625 keV keV^{-1} h^{-1}
1	376.3	0.155	0.034	0.033
2	81.2	0.151	0.034	0.033
3	213.2	0.155	0.034	0.032
Sum	670.6	0.154	0.034	0.033

Table 4.2.: Available data and counting rates of the laboratory background.
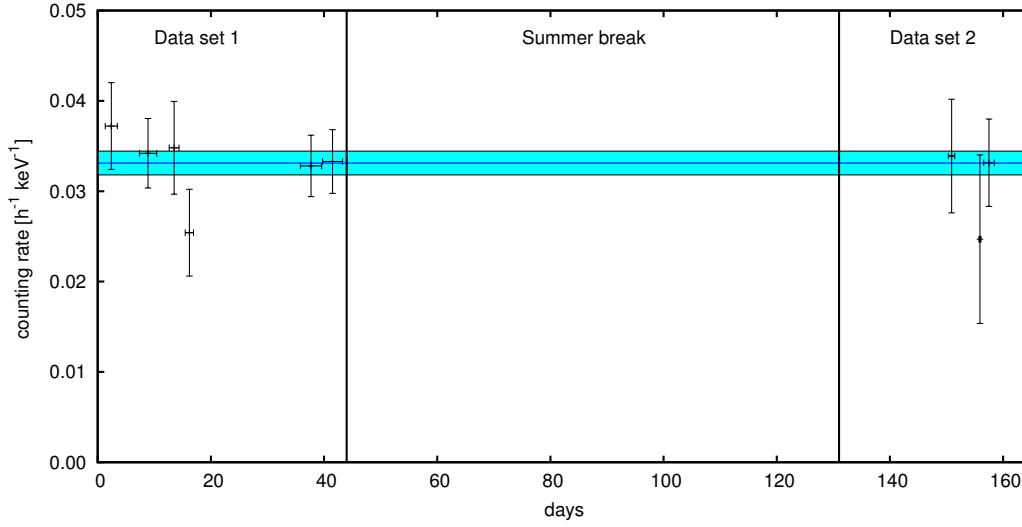
Figure 4.3.: Laboratory background inside the 280 keV/400 keV regions of interest for single measurements in 2011. The average value with its uncertainty is illustrated by a blue bar. Horizontal bars on the data points indicate the length of a measurement.

4.2. The beam induced background

4.2.1. Identified processes

The in-beam γ-spectrum has a remarkably different shape compared to the laboratory background. When the ^{4}He$^+$ beam is incident on the D$_2$ gas target, the event rate in the γ-detector rises by more than an order of magnitude. A comparison of the in-beam with the no-beam spectra is shown in figure 4.4. Additional structures and peaks are visible, which are a clear sign of a neutron flux inside the setup:

- Inelastic neutron scattering on Ge nuclei, Ge(n,n'γ): Neutrons are scattered at Ge nucleons and excite the nucleus: Additional energy is transmitted to populate a discrete energy level. This process is followed by de-excitation via emission of specific γ-rays. They may leave the detector or interact with Ge atoms. If their full energy is registered, a random amount of energy from the recoiled Ge nucleus may be registered in addition. This process contributes the broad triangular shaped structures to the spectrum: A sharp rising left edge (the γ-ray energy is registered only) and a broad (several tens of keV) falling right shoulder, when some kinetic energy of the Ge nucleus is added. In table 4.3, the observed Ge(n,n'γ) peaks are listed.

E_γ [keV]	Interaction	E_γ [keV]	Interaction
563	^{76}Ge(n,n'γ)	1204	^{74}Ge(n,n'γ)
596	^{74}Ge(n,n'γ)	1464	^{72,74}Ge(n,n'γ)
608	^{74}Ge(n,n'γ)	1483	^{74}Ge(n,n'γ)
691	^{72}Ge(n,n'γ)	1697	^{74}Ge(n,n'γ)
834	^{70}Ge(n,n'γ)	1708	^{70}Ge(n,n'γ)
1040	^{70}Ge(n,n'γ)	2155	^{70}Ge(n,n'γ)
1108	^{76}Ge(n,n'γ)	2198	^{74}Ge(n,n'γ)

Table 4.3.: Observed triangular-shaped Ge(n,n'γ) lines in the beam-induced background. The assignment to the Ge isotopes has been done using ENSDF data [14].

- Inelastic neutron scattering on setup materials, Fe/Cr/Ni/Cu/Pb(n,n'γ): The same as above, but the recoiled nuclei are not inside the detector material, and their kinetic energy can not be detected. Some of the emitted γ-rays interact with the detector material, contributing distinct, narrow full energy peaks, Compton continua and other features of γ-spectra. The most important full-energy peaks are marked in figure 4.4.

- Neutron capture, (n,γ): Neutrons are backscattered and thermalized, and might be captured by nuclei inside the setup. A clear evidence for the occurrence of this process is the 198 keV line of ^{71m}Ge, a product of the neutron capture of ^{70}Ge. A possible contribution of ^{56}Fe(n,γ)^{57}Fe to the beam induced background in the ^{2}H(α,γ)^{6}Li region of interest is discussed in section 4.4.4. Other significant neutron capture processes have not been recognized.

The available neutron energy is given by the Q-value and the kinematics of the ^{2}H(^{2}H,n)^{3}He reaction. The maximum deuteron energy at $E_\alpha = 400$ keV is $E_{d,max} = 356$ keV, hence the maximum neutron energy is $E_{n,max} = 3307$ keV. At a beam energy of 280 keV, neutrons may still reach an energy of 3138 keV, so the number of energy levels of setup nuclei that can be populated is limited. Despitely, a low beam-induced background has been measured also above this energy, which points again to the occurrence of neutron capture. A second source of high-energy beam induced background may come from energetic tritons and ^{3}He nuclei that are products of the deuteron-deuteron interaction as well. They can interact with deuterons either in the target gas or on the metal surfaces, in reactions with a high Q-value, producing very energetic protons and neutrons:

- ^{3}H(^{2}H,n)^{4}He, $Q = 17.589$ MeV, $E_{n,max} = 19.4$ MeV

- ^{3}He(^{2}H,p)^{4}He, $Q = 18.353$ MeV, $E_{p,max} = 18.9$ MeV
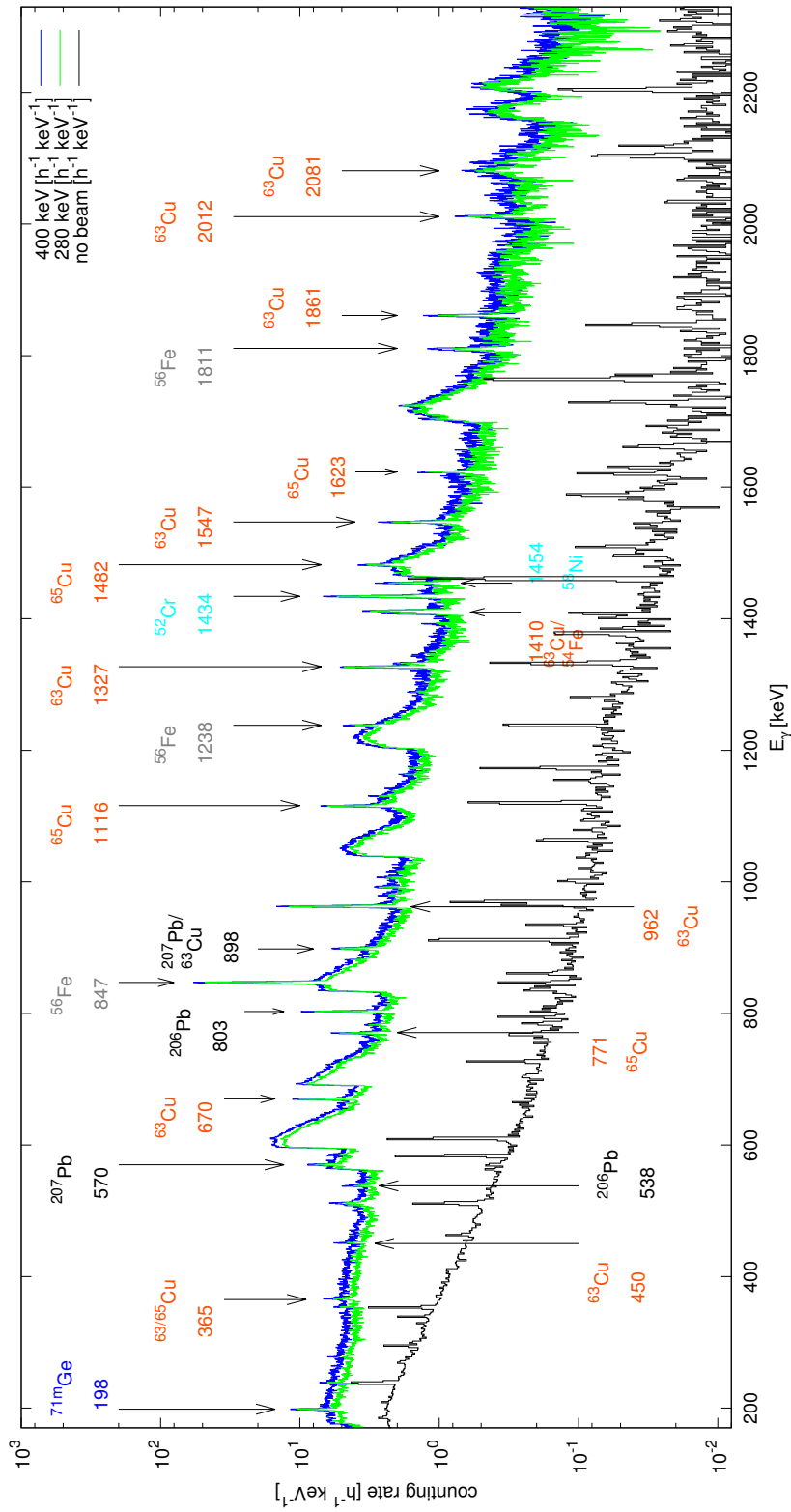
Figure 4.4.: The beam induced background compared with the laboratory background.

These energies open many nuclear reaction channels (including proton capture and nucleon exchange) and allow the excitation of nuclei to high-energy levels as well. Nevertheless, the counting rate of γ-rays with $E_\gamma > 3\,\mathrm{MeV}$ is small compared to the counting rate in the $^2\mathrm{H}(\alpha,\gamma)^6\mathrm{Li}$ region of interest (see table 4.4). The observed increase of high-energy γ-background is due to the accumulating implantation of deuterons, protons and tritons in the metal surfaces that can be reached by energetic particles. Between the measurements of data set 2 and data set 3, the most inner components of the setup have been exchanged: the target collimator, the steel tube and the calorimeter end cap, to remove deuteron-implanted materials. The amount of high-energy γ-rays dropped accordingly, although parts of the target chamber remained contaminated (figures 4.5 and 4.6) which could not be exchanged.

Data set	Counting rates ($\mathrm{keV^{-1}\ C^{-1}}$)		
	$E_\gamma = 1540...1625\,\mathrm{keV}$	$E_\gamma = 1800...3000\,\mathrm{keV}$	$E_\gamma = 3000...4000\,\mathrm{keV}$
1 (400 keV)	0.737	0.159	0.023
2 (400 keV)	0.818	0.181	0.026
3 (360 keV)	0.712	0.157	0.025

Table 4.4.: Counting rates of high-energy beam-induced background.
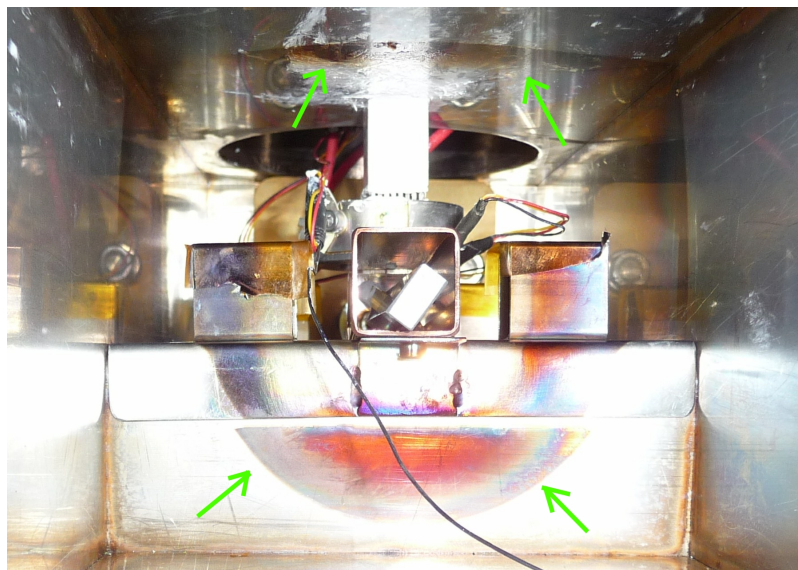
Figure 4.5.: Visible contamination (marked by green arrows) inside the target chamber after the measurement of data set 2 and an accumulated beam charge of 1.05 kC. Compare to the unused setup shown in figure 3.10.
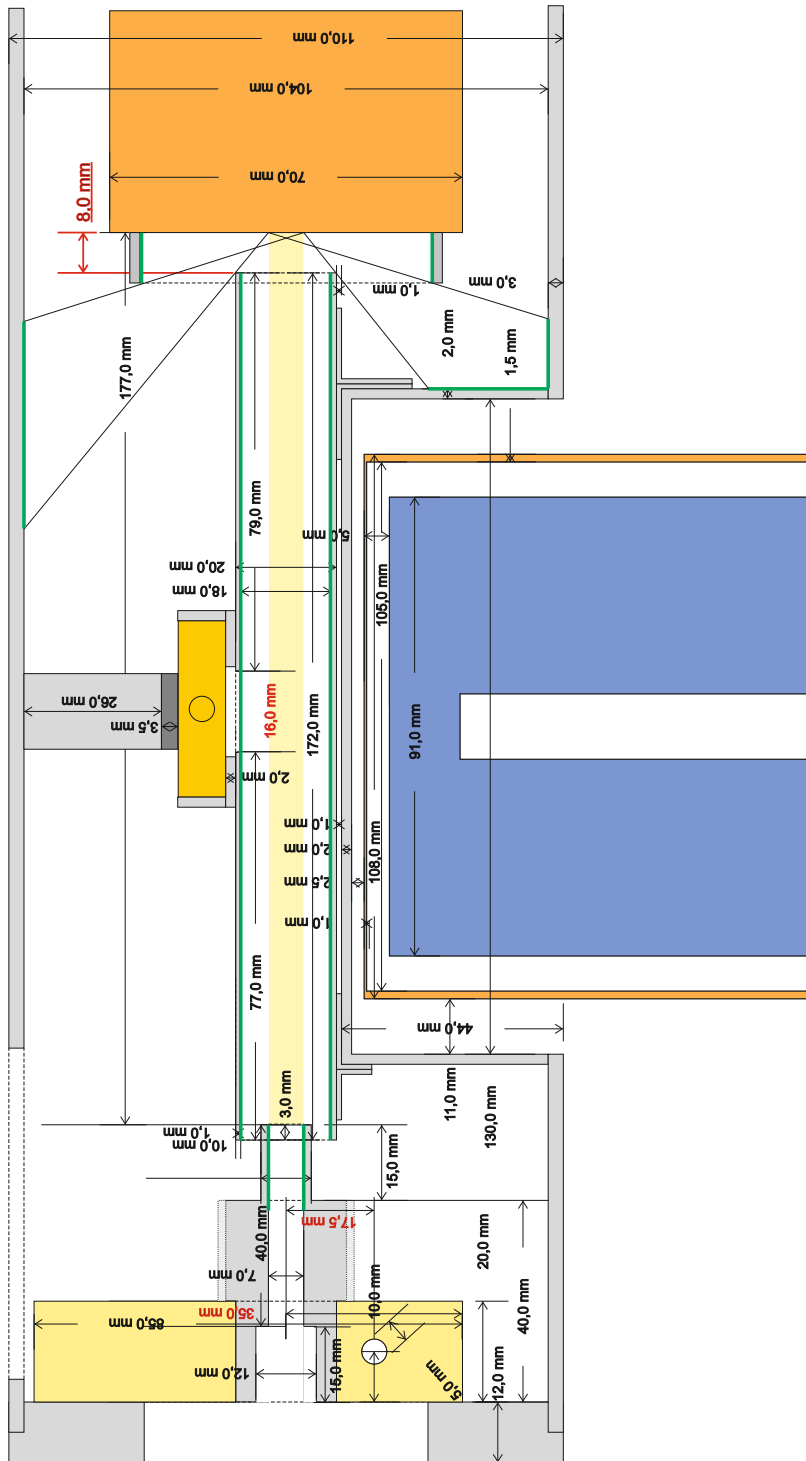
Figure 4.6.: Metal surfaces inside the setup that could undergo implantation of energetic particles are marked with green color.

Inside the ^{2}H(α,γ)^{6}Li regions of interest, after subtraction of the laboratory background, three distinct γ-lines remain and can be identified (table 4.5). The broad triangular ^{74}Ge(n,n'γ) peak at 1483 keV affects the $E_\alpha = 240$ keV region of interest only due to its shape.

E_γ [keV]	Origin	Transitions
1483	^{74}Ge(n,n'γ)	$1483 \rightarrow 596 \rightarrow 0$
1547	^{63}Cu(n,n'γ)	$1547 (\rightarrow 670) \rightarrow 0$
1623	^{65}Cu(n,n'γ)	$1623 (\rightarrow 1116) \rightarrow 0$

Table 4.5.: List of observed γ-lines in the ^{2}H(α,γ)^{6}Li regions of interest. The origin is given for each line.

4.2.2. Monte Carlo simulation

The precise geometry of the LUNA ^{2}H(α,γ)^{6}Li setup has been programmed by Z. Elekes into the Geant4 Monte Carlo simulation software (version 4.9.2) which is gratefully acknowledged. He provided the simulated spectra upon request by the author, who analyzed them. The geometry of the γ-detector has been unknown in the beginning, but has been found empirically by adjusting the values for the size and position of its active volume until the simulated γ-spectra of point-like γ-sources used for the detection efficiency calibration matched the measured ones, and until the simulation software could reproduce the measured full-energy peak detection efficiency curves for several γ-sources.

The simulation for the ^{2}H(α,γ)^{6}Li measurement has been designed to calculate the single processes step by step, in order to use the available computation time in an efficient way:

1. Rutherford scattering: Incident α-particles are scattered on deuterons. The results are the energy and angular distributions of energetic deuterons. For the following step, the energy distribution integrated over all angles is used.

2. Neutron production: Energetic deuterons are started along the beam path with a random angle, and they interact with gas deuterons via the ^{2}H(^{2}H,n)^{3}He reaction. The result is the neutron energy distribution.

3. Neutron interaction: The neutrons are again started randomly along the beam path with the calculated energy distribution and interact with the setup materials and the HPGe detector. The γ-rays that are emitted by any material and later interact with the γ-detector are registered. Its energy resolution is adapted to the measured value.

This has been repeated for all beam energies that were used for the measurement. With this approach, Geant4 was able to reproduce the measured γ-spectra with a very good agreement (see figure 4.8), although there are a few exceptions, marked by red arrows: The decay of the ^{71m}Ge metastable state (1) and the ^{72}Ge deexcitation via internal conversion (2) are not correctly treated by Geant. Furthermore, an error in the databases (3) and a possible erroneous population of Ge levels (4,5) were recognized [44].

In addition, the Geant4 simulation code for the LUNA gas target setup has been benchmarked using a weak ^{241}Am-^{9}Be source (13 neutrons per second) inserted in the steel tube and centered above the γ-detector. It emits neutrons via the ^{9}Be(α,n)^{12}C reaction. Although the available statistics is poor due to necessary restrictions inside the deep underground laboratory, the measured spectrum could be compared with the simulated one (figure 4.7). The agreement is again very good, apart from the known problem with the triangular peak at 691 keV in Geant4. The weak emission of γ-rays by the ^{241}Am source (662 keV and 722 keV) was not implented in the simulation, which explains the deviation below $E_\gamma = 600$ keV.
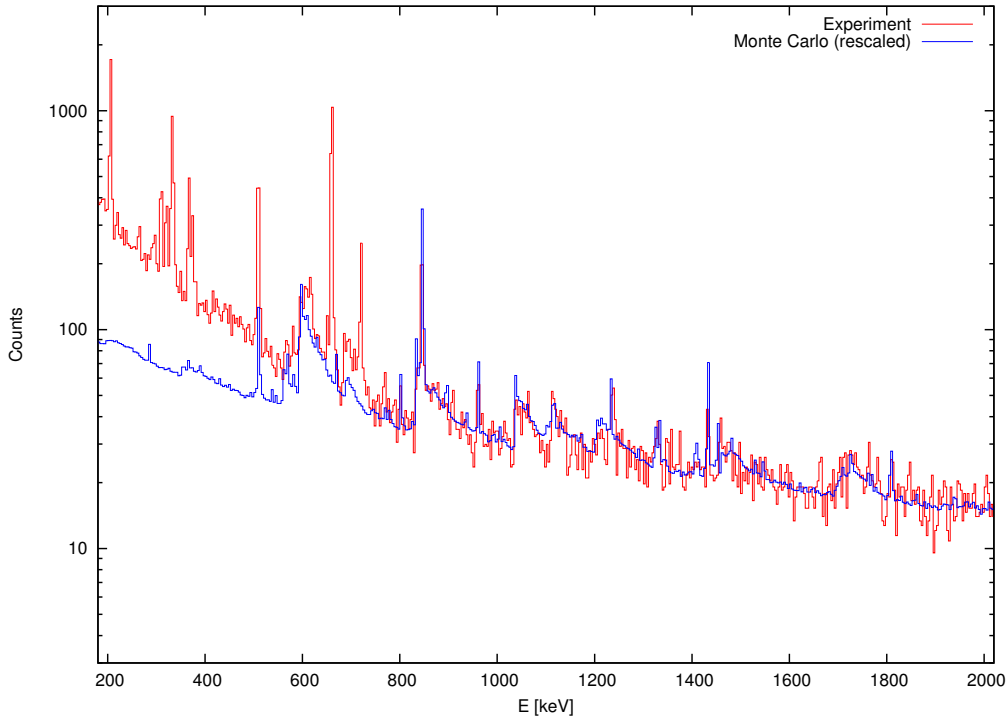
Figure 4.7.: Measured and simulated spectrum of the γ-detector with an AmBe neutron source. The measured spectrum has been rebinned to treat the poor statistics.

61
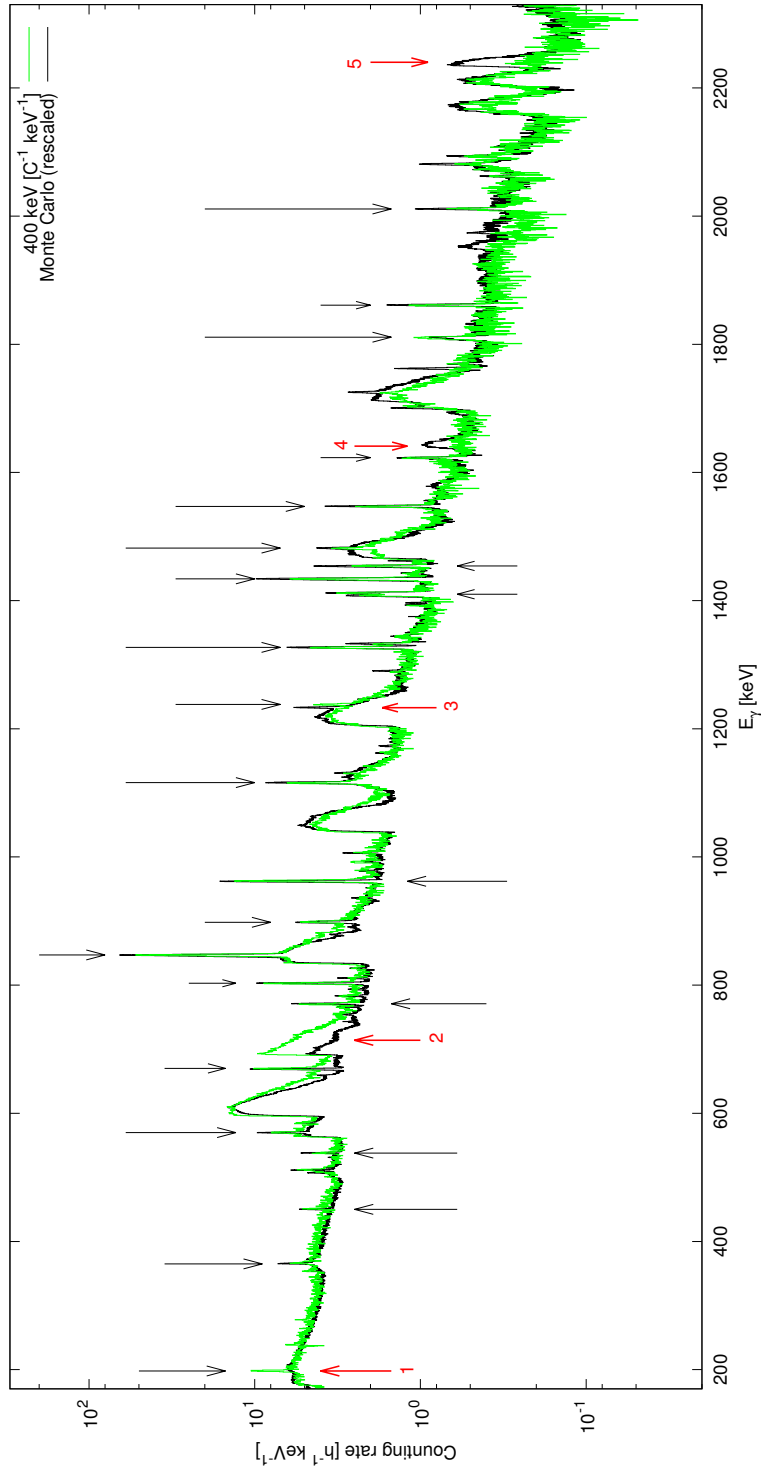
Figure 4.8.: The simulated and the measured γ-spectra compared. The (n,n'γ) lines are marked by black arrows like in figure 4.4. Remarkable deviations are marked by numbered red arrows which are explained in the text.

The Geant4 simulation allows to visualize the contribution of several interaction processes to the measured γ-spectra. This is of high interest to understand the shape of the beam induced background inside the ${}^2\mathrm{H}(\alpha,\gamma){}^6\mathrm{Li}$ regions of interest, and especially a possible beam energy dependence of it.

Analyzing the results of the simulation, only two processes were found to have a non-negligible influence on the shape of the γ-spectra: The inelastic neutron scattering on Ge nuclei, Ge(n,n'γ), and the inelastic neutron scattering on nuclei of the setup materials except for Ge, Fe/Cr/Ni/Cu/Pb(n,n'γ). The comparison in figure 4.9 shows that the contribution of the latter process to the background continuum is one order of magnitude smaller, which is true also for the ${}^2\mathrm{H}(\alpha,\gamma){}^6\mathrm{Li}$ regions of interest (figure 4.10). Furthermore, deviations due to different beam energies appear above the ${}^2\mathrm{H}(\alpha,\gamma){}^6\mathrm{Li}$ regions of interest for both processes.
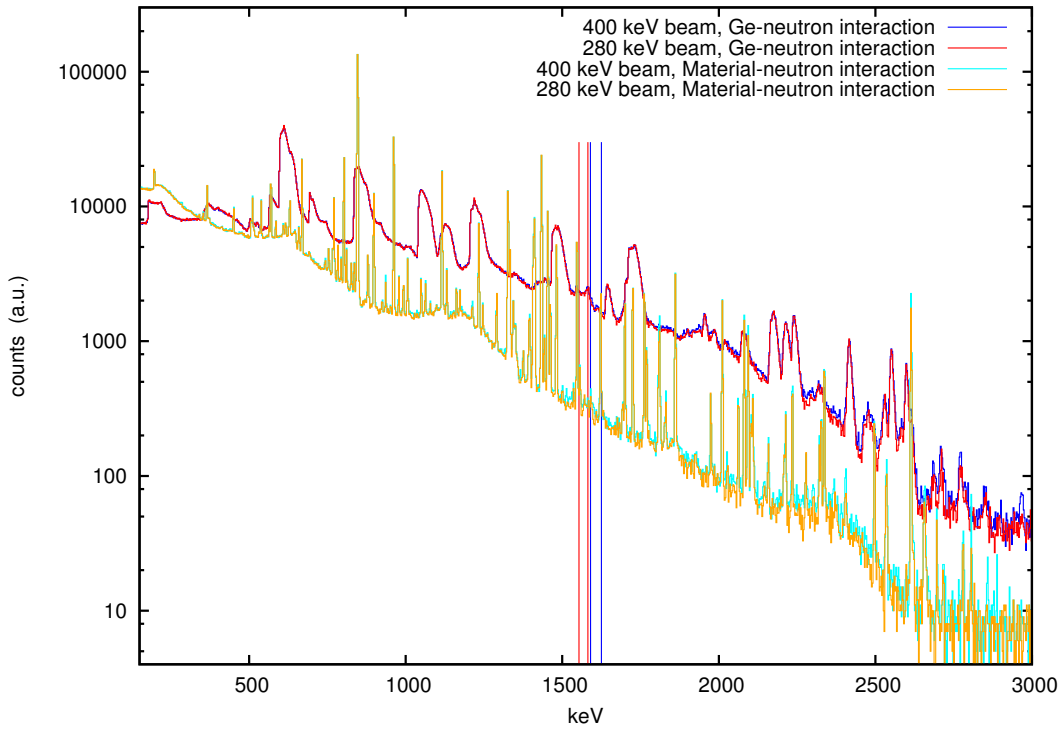
Figure 4.9.: The two major contributions to the beam induced background as simulated by Geant4. The ${}^2\mathrm{H}(\alpha,\gamma){}^6\mathrm{Li}$ regions of interest are marked with lines coloured according to the Ge-neutron interaction spectra.

Although the general agreement is good, the available simulation is not able to precisely reproduce the shape of the beam induced background inside the regions of interest (see figure 4.10) when compared to a measured spectrum. While the agree-

ment is fairly good inside the 400 keV region of interest, the opposite is true inside the 280 keV region of interest and between the two regions. Apparently, the simulated spectrum has a Compton edge-like structure at 1584 keV. The corresponding full energy peak would be located at 1808 keV. This is close to the location of a known and observed ^{56}Fe(n,n'γ) line at 1811 keV.

As a conclusion, the Geant4 simulation is helpful to understand the contribution of specific processes to the beam induced background (which becomes necessary again in section 4.4.1), but can not reproduce the measured γ-spectrum with the precision necessary to understand small energy-dependent deviations in the shape of the neutron-induced background, which would be important for its subtraction.
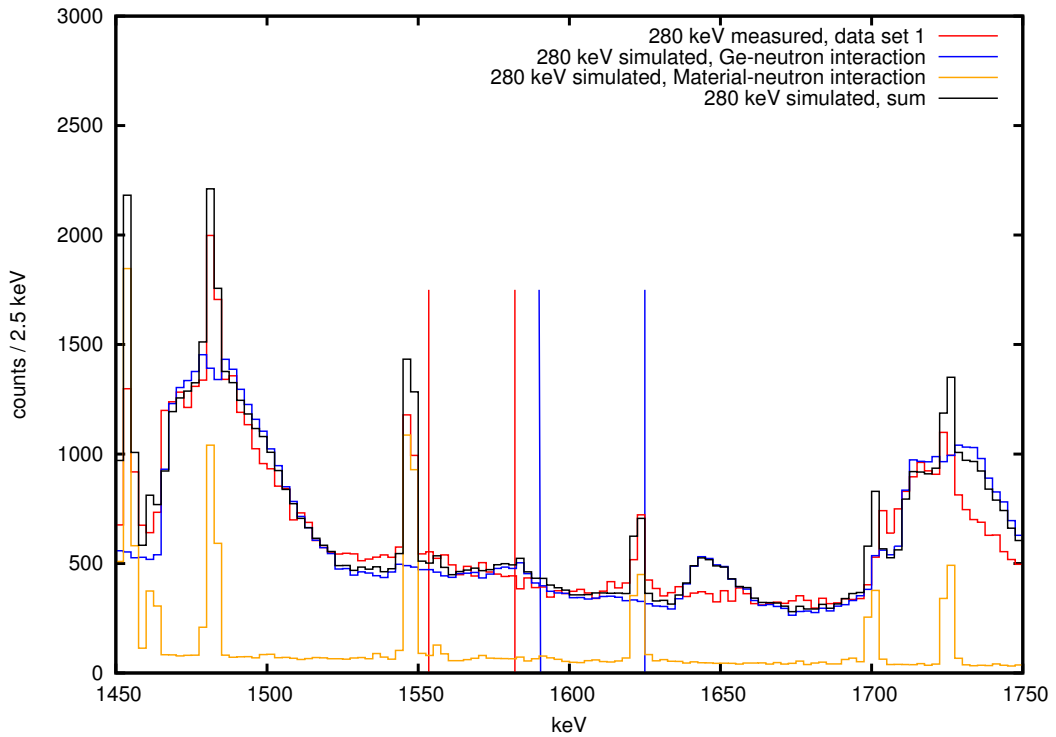
Figure 4.10.: Comparison between measurement and simulation in the case of 280 keV beam energy close to the ^{2}H(α,γ)^{6}Li regions of interest (blue lines: 400 keV beam, red lines: 280 keV beam).

4.2.3. The silicon detector

The silicon detector (see figure 3.10) monitored the rate of neutrons from the ^{2}H(^{2}H,n)^{3}He reaction indirectly by measuring the rate of protons from the ^{2}H(^{2}H,p)^{3}H reaction, which has a similar deuteron-energy dependent cross section in this energy range

[45]. In order to estimate a neutron flux from the measured proton rate, a Monte Carlo simulation based on Geant3 has been developed by P. Corvisiero. It calculates the detection efficiency of protons produced inside the steel pipe when an α-beam is incident on the gas target, and takes the energy straggling due to the protective aluminum foil into account. In figure 4.11, the measured proton energy spectrum is compared to the simulated spectrum, with a very good agreement. Below 1 MeV, the measured spectrum was largely affected by electronic noise. For this reason, it was not possible to see the produced tritons and ^{3}He particles as well. Above 4 MeV, the some single events appeared which could be either induced by electronic noise or measured high-energy protons from the ^{2}H(^{3}He,p)^{4}He reaction. In this area, also the pulser peak was located, to measure the dead time precisely (see also section 3.3.1).
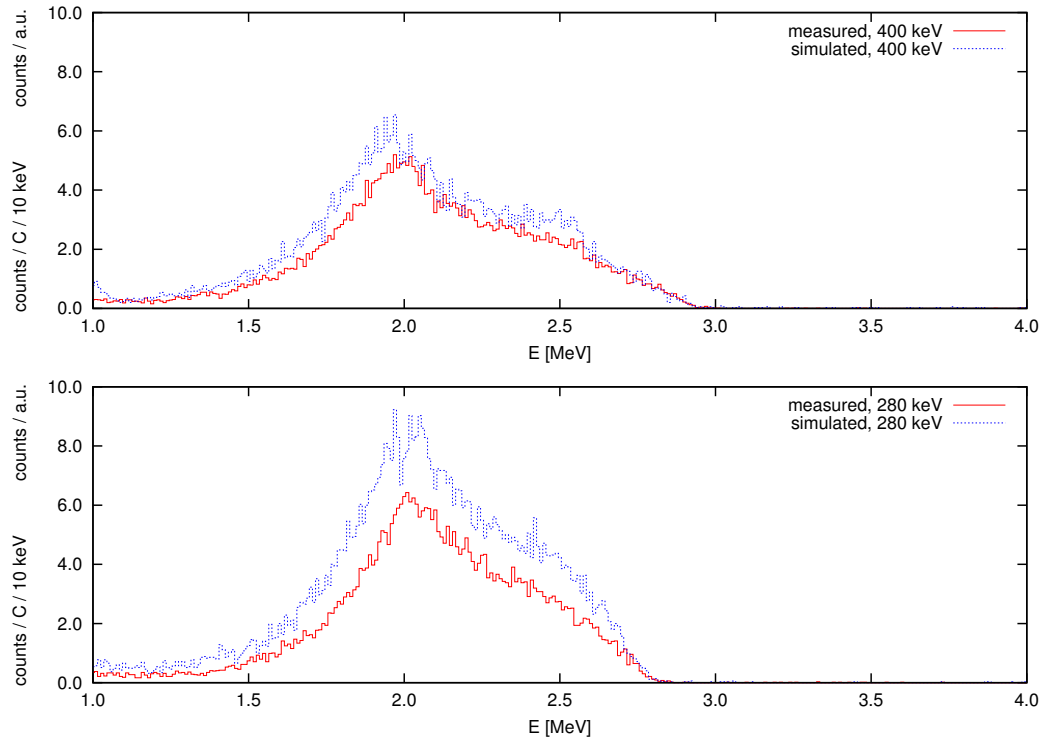
Figure 4.11.: Simulated (using a modified Geant3 software) and measured proton spectra of the silicon detector compared. The simulated spectra are arbitrarily normalized.

The increase of the neutron rate due to the implantation of deuterium led to an increase in the proton rate as well (figure 4.12). Both rates are well correlated in general. Reliable data are available for data set 1 only. Strong electronic noise affected later measurements, apart from single exceptions.
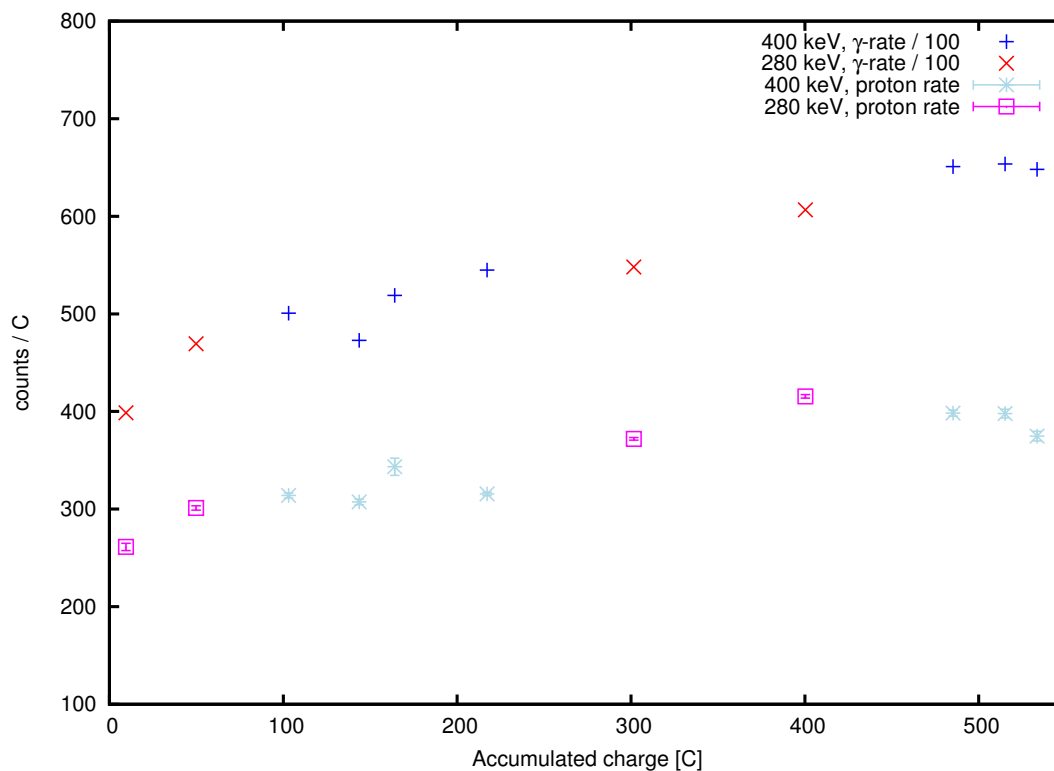
Figure 4.12.: Counting rates of the silicon and the γ-detector with growing deuterium implantation. The γ-rate was obtained by integrating the spectrum for $E_\gamma = 200...4000\,\text{keV}$ and is shown normalized.

Additional protons come from reactions with implanted deuterium only, and only protons from inside the steel tube can reach the silicon detector. Therefore, it can be concluded that additional neutrons that interact with the HPGe detector come mainly from the steel tube. In cases where the proton and the γ-rate rate behaved differently, implantation of deuterons must have occurred also at another site. Possible surfaces where implantation may occur, and which have not been mentioned yet, are the outer surface of the target collimator and the surface of the beam stop. Implantation in these surfaces depend on the beam focus (which has been different for every single run) and on the beam intensity. Both parameters could not be reproduced, or changed within a single run.

4.3. Subtraction of the beam induced background

4.3.1. Variability

Due to the implantation of deuterons in metal surfaces, the neutron field changes slowly its geometric shape (additional neutron sources are generated and become stronger) and its energy spectrum due to an increasing contribution of in general lower-energy neutrons from deuterated surfaces: Deuterons may lose a noticeable amount of energy inside the metal before interacting with another deuteron. The possible influence of the origin of neutrons (and hence the geometric shape of the neutron field) on the shape of the beam induced background is demonstrated in figure 4.13. In case of the target collimator and the steel tube, neutrons are started from $10\,\mu$m below the metal surface. Neutrons started in the gas, from the beam axis are the standard case in all other simulated γ-spectra shown.
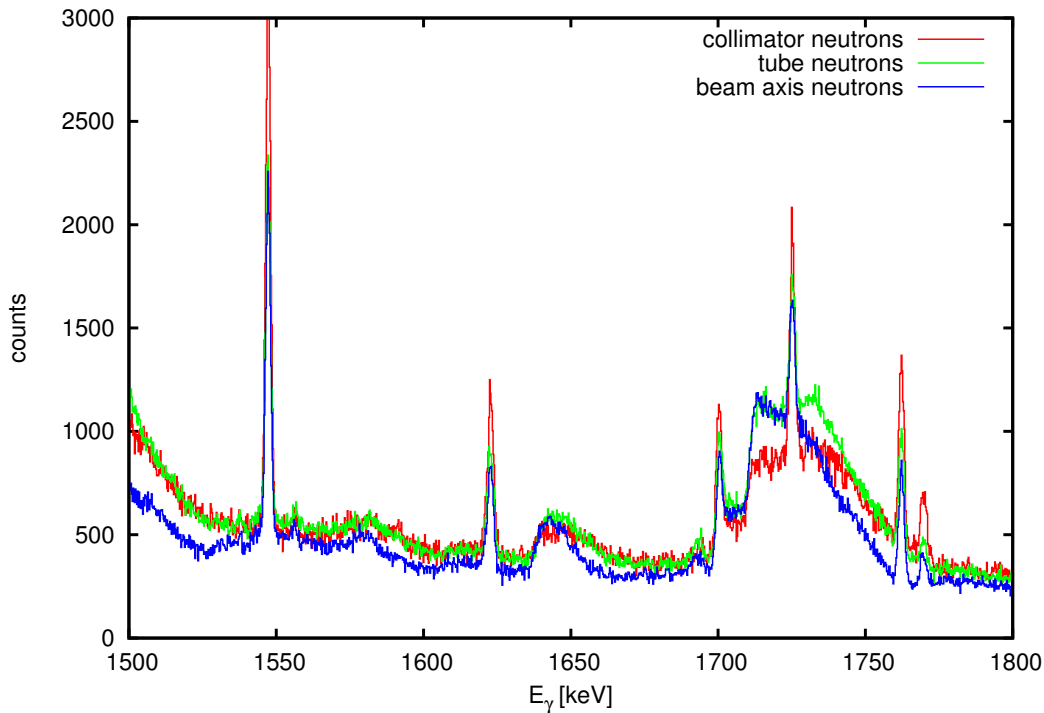
Figure 4.13.: Beam induced background around and above the $^2\mathrm{H}(\alpha,\gamma)^6\mathrm{Li}$ regions of interest due to neutrons of different origin, simulated by Geant4, with arbitrary normalization factors.

The precise distribution and density of implanted deuterons which serve as addi-

tional targets for the ^{2}H(^{2}H,n)^{3}He reaction depends on many parameters (such as the beam current and the beam focus), hence the time dependence of the shape of the beam induced background is unknown.

Similar considerations are true for systematic errors due to the subtraction of γ-spectra aquired at different beam energies. The neutron energy spectrum and the shape of the neutron field vary with the beam energy due to the energy dependences of the Rutherford scattering process and the ^{2}H(^{2}H,n)^{3}He cross section. At a beam energy of 280 keV, the number of energetic deuterons is higher due to a bigger cross section for elastic scattering, but the average deuteron energy is lower compared to the 400 keV case. This leads to deviations in the spectral energy fluence of the neutron field. In fact, the beam induced background rate at a beam energy of 280 keV appears to be systematically lower towards higher γ-energies in the spectrum. Nevertheless, the main source of kinetic neutron energy is given by the Q-value of the ^{2}H(^{2}H,n)^{3}He reaction (Q = 3.269 MeV). Inside the ^{2}H(α,γ)^{6}Li regions of interest, the simulated shape of the background induced by neutrons started in the gas is apparently equal for beam energies of 280 keV and 400 keV (fig. 4.14).
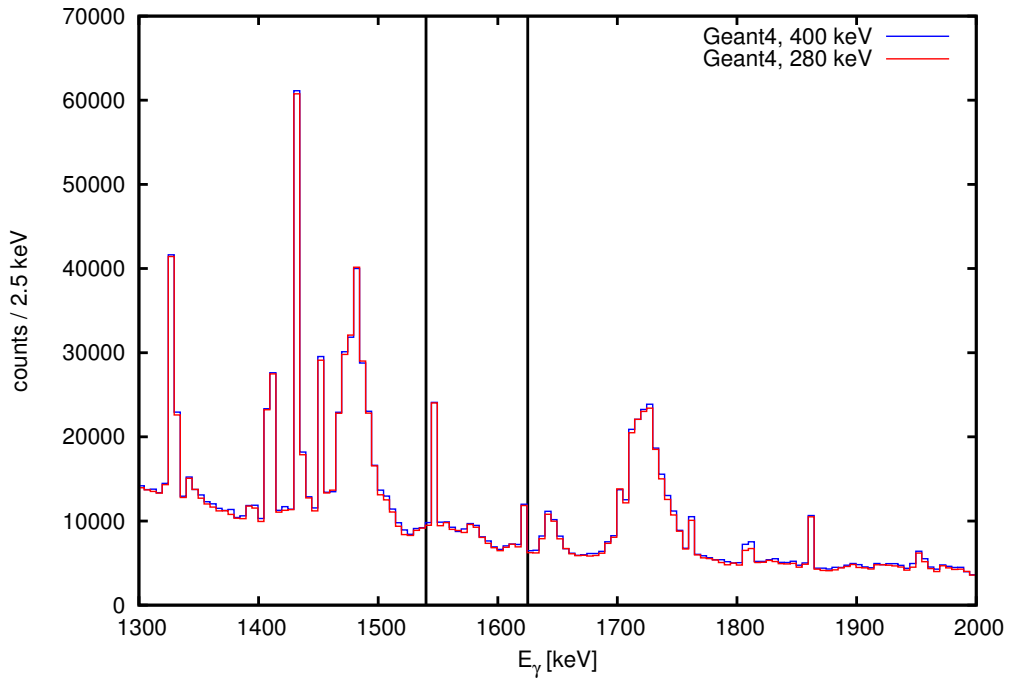
Figure 4.14.: Simulated beam induced background inside the ^{2}H(α,γ)^{6}Li regions of interest (marked by two black lines) for gas neutrons with a large binning to reduce statistical fluctuations. In each simulation, 350 million neutrons were started.

To obtain the weak ^{2}H$(\alpha,\gamma)^6$Li signal, two large numbers have to be subtracted. For this reason, also small deviations in the shape of the measured beam induced background matter and are the main source of systematic errors.

Hence, subtracting a 280 keV γ-spectrum from a 400 keV γ-spectrum, normalizing just with the ratio of applied beam charges, gives wrong results. Trying empirical constant normalization factors to be used for the entire γ-spectrum is not helpful as well, because the systematic errors coming from the different neutron energy spectra would be ignored. Therefore, a γ-energy dependend normalization factor is needed, which still must be found empirically, because the knowledge of the neutron field and its interactions is very limited. However, small deviations in the shape of the background inside the ^{2}H$(\alpha,\gamma)^6$Li regions of interest (like the example in figure 4.13) can not be treated in this way and will remain as systematic errors.

4.3.2. Parametrization

The γ-spectrum that is used to subtract the beam induced background from another γ-spectrum has to be normalized, to ensure that the correct number of events (that is, the same amount of beam induced background) is subtracted. If this is done properly, the residual spectrum will be flat and zero within statistical fluctuations, apart from remaining ^{2}H$(\alpha,\gamma)^6$Li events inside the region of interest. In a range of $E_\gamma = 1550...1620$ keV, the beam induced background is mainly flat and consists of the sum of several Compton continua. To find a correct normalization factor for this area, a way to parameterize this beam induced background continuum is needed.

Due to the high number of peaks and other features in the γ-spectra acquired, a continuous determination of an energy dependent normalization factor for the background continuum is not possible. Thus, several "flat regions" along the spectrum, which consist of Compton continua only without any visible structure inside, have been chosen (see table 4.6 and figure 4.16). For all of these regions and for all data sets, the sum of events (reduced by the laboratory background) has been calculated, and then ratios ρ_r according to

$$\rho_r = \frac{N_{280\,\mathrm{keV}}}{N_{400\,\mathrm{keV}}} \tag{4.2}$$

for each region r. Plotting these values against the median γ-energies of the flat regions (see figure 4.15), a decreasing trend is visible towards higher γ-energies, although the error bars are large. The values obtained using the results of the Geant4 simulation show a similar behaviour.

Region median (keV)	Region half width (keV)	Content $N_{400\text{keV}}$	Content $N_{280\text{keV}}$	Ratio ρ_r	Error (%)
219	11	32313	32698	1.012	0.78
435	8	16468	16966	1.030	1.09
818.5	5.5	6562	6667	1.016	1.74
1027	7	6273	6180	0.985	1.79
1190	10	7207	7331	1.017	1.66
1308	8	4945	4904	0.992	2.02
1531	11	4639	4712	1.016	2.07
1631.5	4.5	1308	1324	1.013	3.90
1838	18	3718	3571	0.961	2.34
1986	18	2328	2161	0.928	2.99
2275	15	1133	893	0.788	4.48
2465	25	1122	957	0.853	4.40

Table 4.6.: Flat regions parameters and values for data set 1. The values for other data sets can be found in Appendix A.2.
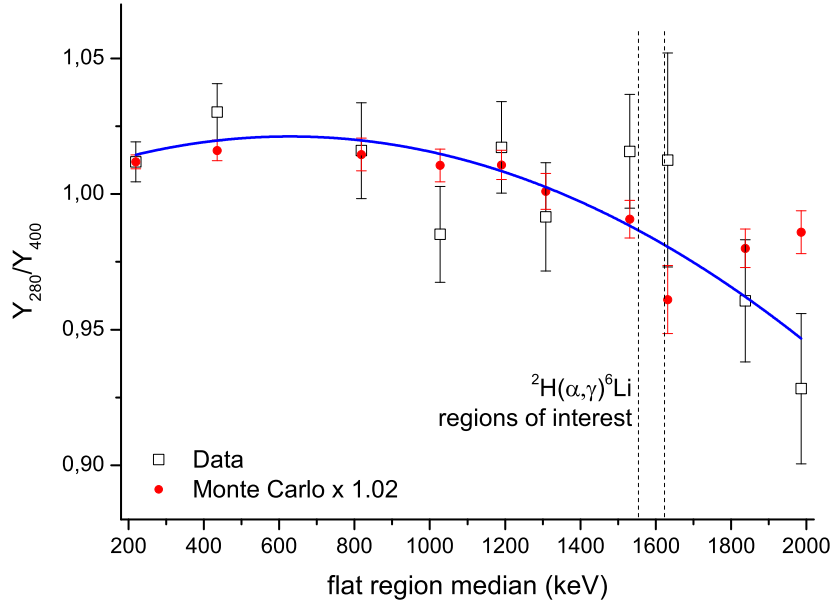
Figure 4.15.: Plot of the obtained ρ_r for data set 1, compared with the values obtained from the results of the Geant4-simulation. A fit to the measured data is attempted with a parabola function (blue graph). The ^{2}H(α,γ)^{6}Li region of interest is marked by dashed lines.
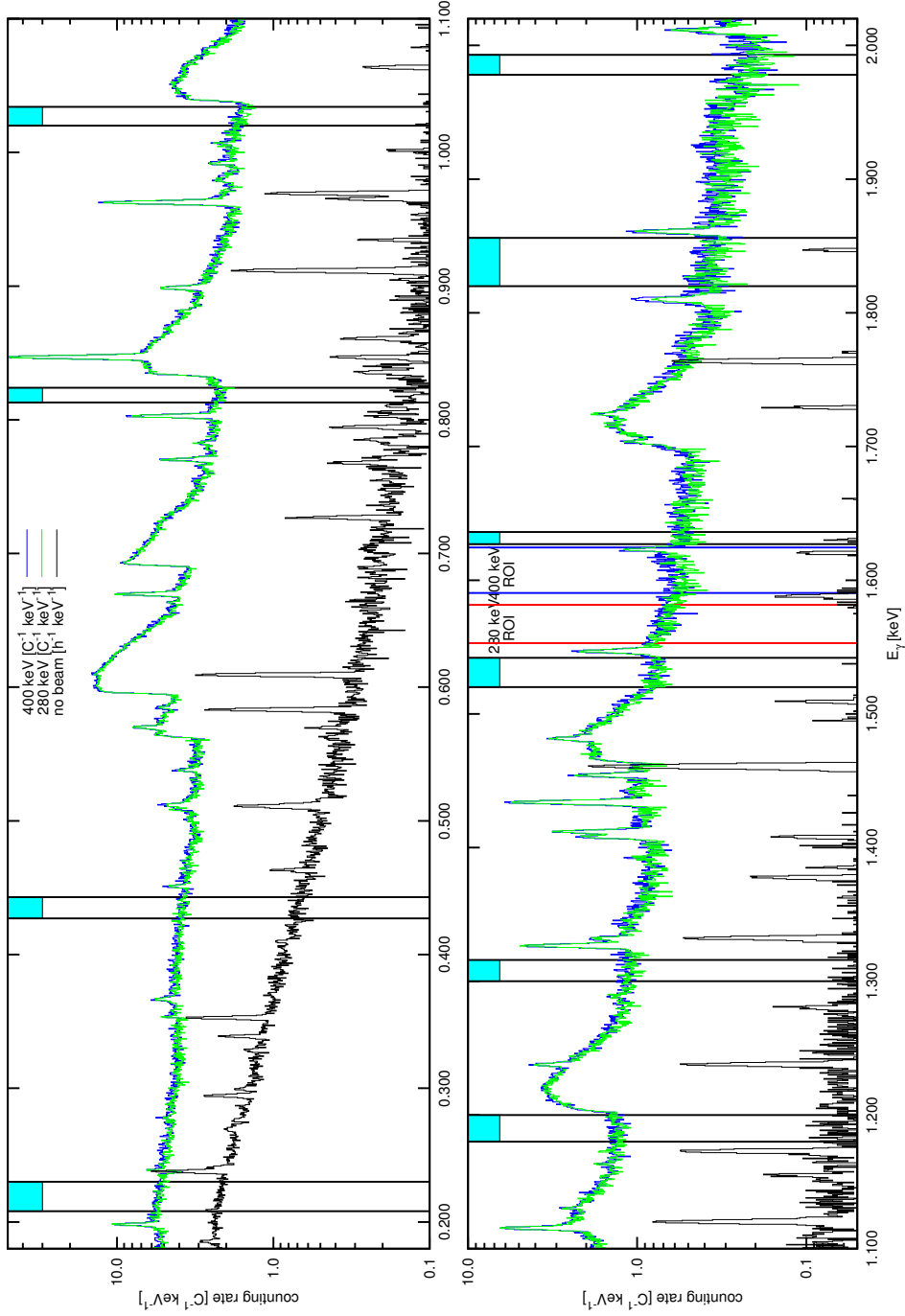
Figure 4.16.: Obtained ^{2}H$(\alpha,\gamma)^6$Li spectra at two beam energies. The flat regions are marked with blue boxes, and the regions of interest with colored boxes as indicated.

The beam induced background continuum itself shows an exponentially falling γ-energy dependence (figure 4.17), with a remarkable kink close to the $^2\mathrm{H}(\alpha,\gamma)^6\mathrm{Li}$ region of interest.
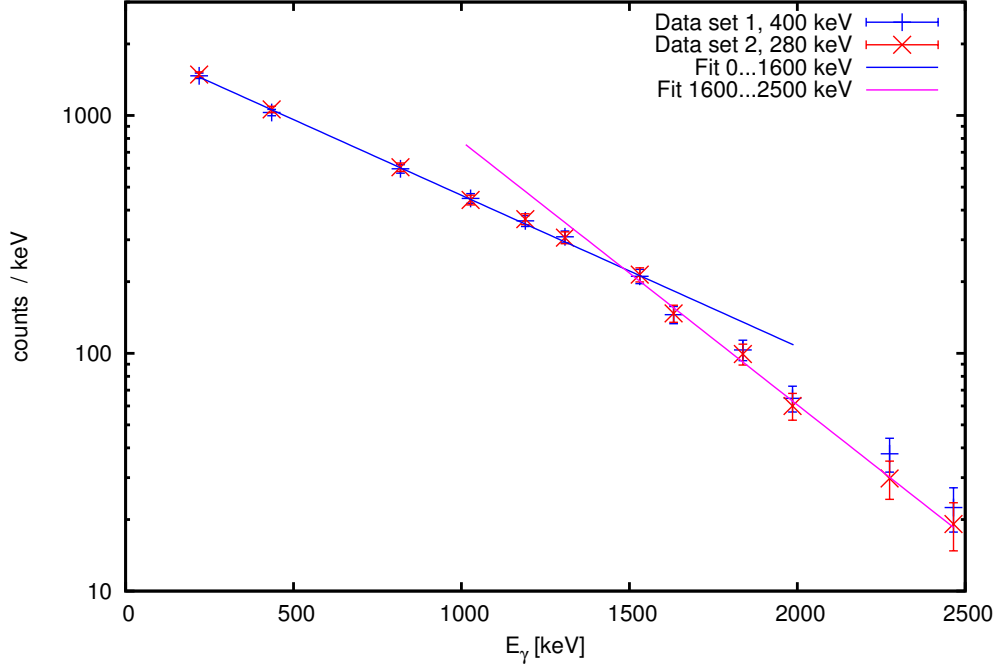
Figure 4.17.: The flat region contents show an exponentially decreasing behaviour, the fit functions used were always like $f(x) = A\,e^{-B\,x}$. The point where the parameters change is close to the $^2\mathrm{H}(\alpha,\gamma)^6\mathrm{Li}$ region of interest.

4.3.3. Weighted average of several fit functions (Method 1)

Now several functions can be applied to fit the data points ρ_r, to get a good approximation for the true value of the normalization factor $\eta(E_\gamma)$ inside the $^2\mathrm{H}(\alpha,\gamma)^6\mathrm{Li}$ region of interest. This has been done using ten different functions of several types, not preferring any assumed model like exponential decrease. The only criteria were a converging fit, and the result should match the data points well. The functions are listed (as they are named in Origin 8.5) in table 4.7 together with the results of their best fits. The weighted average is then calculated as follows: All data points contain statistical errors according to the number of counts inside the single flat regions. These error bars are considered by the fit algorithm, and are smaller towards lower γ-energies. After the fit has converged, the 68 % confidence bands for every fitted

function are available, and in this way also the confidence limits for the function value at the ^{2}H$(\alpha,\gamma)^6$Li region of interest. The difference between the $68\,\%$ confidence limit and the function value is defined here as $\Delta f_i(E_\gamma)$.

Name	Equation	$\eta(1617.6\,\text{keV})$	χ^2/DoF
Harris	$\eta = \frac{1}{A+BE_\gamma^C}$	0.9847	1.49373
GaussAmp	$\eta = A + B\,e^{-0.5\left(\frac{E_\gamma-C}{D}\right)^2}$	1.0091	0.90403
Holliday	$\eta = \frac{1}{A+BE_\gamma+CE_\gamma^2}$	0.9714	1.80802
Allometric2	$\eta = A + BE_\gamma^C$	0.9830	1.55122
Cubic	$\eta = A + BE_\gamma + CE_\gamma^2 + DE_\gamma^3$	0.9817	1.73512
MnMolecular	$\eta = A(1 - e^{B(E_\gamma+C)})$	0.9816	1.66834
Logistic	$\eta = A + \frac{B-A}{1+\left(\frac{E_\gamma}{C}\right)^D}$	1.0085	1.17025
Exp3P1Md	$\eta = e^{A+\frac{B}{E_\gamma+C}}$	0.9767	2.04578
Parabola	$\eta = A + BE_\gamma + CE_\gamma^2$	0.9742	1.67272
Lin1027-1986	$\eta = A + BE_\gamma$	0.9806	1.47315
	weighted average	0.991(40)	

Table 4.7.: Functions used to fit the energy dependence of the normalization factor, with results for data set 1 and the 400 keV region of interest.

The quality of a fit is represented by the χ^2/DoF value. It has to be included in the weighting of all fit functions f_i if it is larger than 1, as this points to an underestimation of the fit error [46]. Hence, each weight is calculated by

$$w_i(E_\gamma) = (\Delta f_i(E_\gamma))^{-2} \quad \text{if} \quad \chi^2/\text{DoF} \leq 1 \tag{4.3}$$

or

$$w_i(E_\gamma) = (\sqrt{(\chi^2/\text{DoF})_i} \times \Delta f_i(E_\gamma))^{-2} \quad \text{if} \quad \chi^2/\text{DoF} > 1 \tag{4.4}$$

Now, the weighted average of the function values, which is then an approximation of the true energy-dependent normalisation factor, is calculated via

$$\eta(E_\gamma) = \frac{\sum w_i(E_\gamma) \times f_i(E_\gamma)}{\sum w_i(E_\gamma)} \tag{4.5}$$

The uncertainty of $\eta(E_\gamma)$ is given by

$$\Delta\eta(E_\gamma) = \sqrt{\frac{1}{\sum w_i(E_\gamma)}} \tag{4.6}$$

Before finally adopting this value, a second χ^2 test is necessary, to take possible remaining error underestimations into account. A value

$$\chi_\eta^2 = \sum [w_i(E_\gamma) \times (\eta - f_i(E_\gamma))^2] \tag{4.7}$$

is compared with $N-1$, the expectation value of χ_η^2 if the function values are normally distributed ($N = 10$ is the number of functions). If $\chi_\eta^2/(N-1) > 1$, an underestimation of the errors is likely, and $\Delta\eta(E_\gamma)$ has to be multiplied with a correction factor

$$S = \sqrt{\frac{\chi_\eta^2}{N-1}} \tag{4.8}$$

to get the final uncertainty [46]. This correction was found to be necessary only for data set 1. In table 4.8, the results are listed.

Data set, E_α	$\overline{f_i(E_\gamma)}$	$\sigma(f_i(E_{\gamma,\text{mean}}))$	$\frac{\chi_\eta^2}{N-1}$	$\eta(E_{\gamma,\text{mean}})$	$\Delta\eta(E_{\gamma,\text{mean}})$
1, 400 keV	0.9852	0.0125	1.65	0.9946	0.0066
1, 280 keV	0.9883	0.0117	1.80	0.9984	0.0064
2, 400 keV	1.0124	0.0056	0.21	1.0128	0.0035
2, 280 keV	1.0160	0.0054	0.22	1.0166	0.0033
3, 360 keV	0.8327	0.0042	0.07	0.8332	0.0048
3, 240 keV	0.8369	0.0046	0.07	0.8376	0.0047
1+2, 400 keV	1.0002	0.0080	0.68	1.0004	0.0027
1+2, 280 keV	1.0037	0.0079	0.78	1.0039	0.0026

Table 4.8.: Analysis of the fit results, and the weighted averages.

4.3.4. Non-γ-energy dependent normalizations (Methods 2 and 3)

The previous method using several fit functions considers the entire γ-energy range of 0.2...2.0 MeV, which has a disadvantage: The error bars of data points at lower γ-energies are small due to the comparably high available statistics, giving them more influence in the choice of the best fit than the more interesting high-energy data points. This is avoided by a second approach: The normalization factor is assumed to be constant only within a smaller range around the $^2\mathrm{H}(\alpha,\gamma)^6\mathrm{Li}$ region of interest, here 1300...1800 keV. This range contains four data points. Assuming their weighted average as a good approximation for the true normalization factor, it is calculated via

$$\eta = \frac{\sum w_r \times \rho_r}{\sum w_r} \tag{4.9}$$

where ρ_r are all four data points within the 1300...1800 keV range, and w_r their weights. They are calculated from the inverse of the squared errors of the data points:

$$w_r = \frac{1}{(\Delta \rho_r)^2} \tag{4.10}$$

Finally the uncertainty of η is given by

$$\Delta \eta = \sqrt{\frac{1}{\sum w_r} \times \frac{\sum (w_r \times (\eta - \rho_r)^2)}{3}} \tag{4.11}$$

with a similar correction as it was introduced in equations (4.7) and (4.8). Only four data points are available for the average calculation, so the error bars are higher than in the previous method.

Data set	η	$\Delta\eta$
1	0.993	0.013
2	1.024	0.017
3	0.840	0.010
1+2	1.0098	0.0081

Table 4.9.: The weighted averages of neighbouring regions with their errors.

Two of the chosen flat regions are very close to the $^2\mathrm{H}(\alpha,\gamma)^6\mathrm{Li}$ region of interest, one at higher γ-energy and one at a lower. As it is apparent in figure 4.15, in this data set both data points have higher values compared to the common trend, so one could assume their values reflect the actual normalization factor in the $^2\mathrm{H}(\alpha,\gamma)^6\mathrm{Li}$ region of interest better than any other value calculated from fits or a weighted average. A drawback is the narrowness of the used flat regions, leading to comparably big error bars in this third method to determine the normalization factor.

In this case, one applies

$$\eta_{400\,\text{keV ROI}} = \rho_{1631.5\,\text{keV}} \qquad\qquad \Delta\eta_{400\,\text{keV ROI}} = \Delta\rho_{1631.5\,\text{keV}} \qquad (4.12)$$

and

$$\eta_{280\,\text{keV ROI}} = \rho_{1531\,\text{keV}} \qquad\qquad \Delta\eta_{280\,\text{keV ROI}} = \Delta\rho_{1531\,\text{keV}} \qquad (4.13)$$

with errors of $4\,\%$ and $2\,\%$ in case of data set 1.

4.3.5. Yield calculation and uncertainty

The number of events D due to the $^2\text{H}(\alpha,\gamma)^6\text{Li}$ reaction can now be obtained via

$$D_{400\,\text{keV}} = N_{400\,\text{keV}}^{\text{ROI}\,400} - \frac{t_{400\,\text{keV}}}{t_{\text{LBG}}}LBG^{\text{ROI}\,400} - \frac{N_{280\,\text{keV}}^{\text{ROI}\,400} - \frac{t_{280\,\text{keV}}}{t_{\text{LBG}}}LBG^{\text{ROI}\,400}}{\eta(E_\gamma)} \qquad (4.14)$$

and

$$D_{280\,\text{keV}} = N_{280\,\text{keV}}^{\text{ROI}\,280} - \frac{t_{280\,\text{keV}}}{t_{\text{LBG}}}LBG^{\text{ROI}\,280} - \eta(E_\gamma)\times\left(N_{400\,\text{keV}}^{\text{ROI}\,280} - \frac{t_{400\,\text{keV}}}{t_{\text{LBG}}}LBG^{\text{ROI}\,280}\right) \qquad (4.15)$$

where, as an example, $N_{400\,\text{keV}}^{\text{ROI}\,280}$ is the number of events in the in the γ-spectrum obtained at $E_\alpha = 400\,\text{keV}$ in the $280\,\text{keV}$ region of interest (defined in table 3.4). The laboratory background $LBG^{\text{ROI}\,280}$ is the number of counts in the same region of interest but obtained without beam. It is normalized with the live measurement times. Similar formulae are applied for data set 3.

The $^2\text{H}(\alpha,\gamma)^6\text{Li}$ yield Y for a specific data set is then determined via

$$Y_{\text{E}_\alpha,\text{ds}} = \frac{D_{\text{E}_\alpha,\text{ds}}}{Q_{\text{E}_\alpha,\text{ds}}} \qquad (4.16)$$

All values used to calculate the yields carry statistical uncertainties. In the present case the live time values are assumed to be exact, so the statistical error of subtraction in case of the $400\,\text{keV}$ $^2\text{H}(\alpha,\gamma)^6\text{Li}$ signal is calculated as follows:

$$\Delta D_{400\,\text{keV}} = \sqrt{N_{400\,\text{keV}}^{\text{ROI}\,400} + \left(\frac{t_{400\,\text{keV}}}{t_{\text{LBG}}}\right)^2 LBG^{\text{ROI}\,400} +}$$

$$\overline{+\frac{(\Delta\eta(E_\gamma))^2}{\eta^4(E_\gamma)}\left(N_{280\,\text{keV}}^{\text{ROI}\,400} - \frac{t_{280\,\text{keV}}}{t_{\text{LBG}}}LBG^{\text{ROI}\,400}\right)^2 +}$$

$$\overline{+\frac{1}{\eta^2(E_\gamma)}\left(N_{280\,\text{keV}}^{\text{ROI}\,400} + \left(\frac{t_{280\,\text{keV}}}{t_{\text{LBG}}}\right)^2 LBG^{\text{ROI}\,400}\right)} \qquad (4.17)$$

And, in case of the lower corresponding beam energy, the derived formula is:

$$\Delta D_{280\,\text{keV}} = \sqrt{N_{280\,\text{keV}}^{\text{ROI}\,280} + \left(\frac{t_{280\,\text{keV}}}{t_{\text{LBG}}}\right)^2 LBG^{\text{ROI}\,280} +}$$

$$\overline{+(\Delta\eta(E_\gamma))^2 \times \left(N_{400\,\text{keV}}^{\text{ROI}\,280} - \frac{t_{400\,\text{keV}}}{t_{\text{LBG}}} LBG^{\text{ROI}\,280}\right)^2 +}$$

$$\overline{+\eta^2(E_\gamma)\left(N_{400\,\text{keV}}^{\text{ROI}\,280} + \left(\frac{t_{400\,\text{keV}}}{t_{\text{LBG}}}\right)^2 LBG^{\text{ROI}\,280}\right)} \tag{4.18}$$

As above, analogous formulae are applied for data set 3.

4.3.6. Preliminary values and discussion

Exemplary results for normalization method 1 are given in table 4.10, and compared to the results of the γ-energy independent normalization methods in figure 4.18.

Weighted average of fit functions				charge normalized	
Data set	Beam energy (keV)	Signal D counts	Error ΔD counts	Yield Y counts / C	Error ΔY counts / C
1	400	565	121	2.13	0.46
1	280	-76	116	-0.27	0.42
2	400	29	128	0.12	0.51
2	280	409	124	1.57	0.47
3	360	115	119	0.46	0.47
3	240	151	111	0.72	0.53
1+2	400	542	173	1.05	0.34
1+2	280	383	167	0.71	0.31

Table 4.10.: Calculated yields after subtraction of the beam induced background, using the energy dependent normalization factor value, calculated from the weighted average of the fit functions, at the center of the corresponding ^{2}H$(\alpha,\gamma)^6$Li region of interest.

With one exception (data set 3, 360 keV), all methods to determine the normalization factor give equal yield results within the error bars. Also, for each of these methods, there are strong discrepancies between the single data sets. One has to note that the error bars represent 1σ of confidence level, thus one result does not necessarily exclude the result of another data set. Values below zero are anyway physically impossible. Furthermore, higher counting rates at lower beam energy (as

it is observed in data set 2) are questionable as there are no resonances expected, and the results of data sets 1 and 2 are compatible only within doubled error values. Obviously, the normalization factor in the ${}^2\mathrm{H}(\alpha,\gamma){}^6\mathrm{Li}$ region of interest is not determined properly in at least one of the data sets, leading to a wrong subtraction and an overestimation of the 400 keV yield with respect to the 280 keV yield in case of data set 1, and the opposite in case of data set 2.
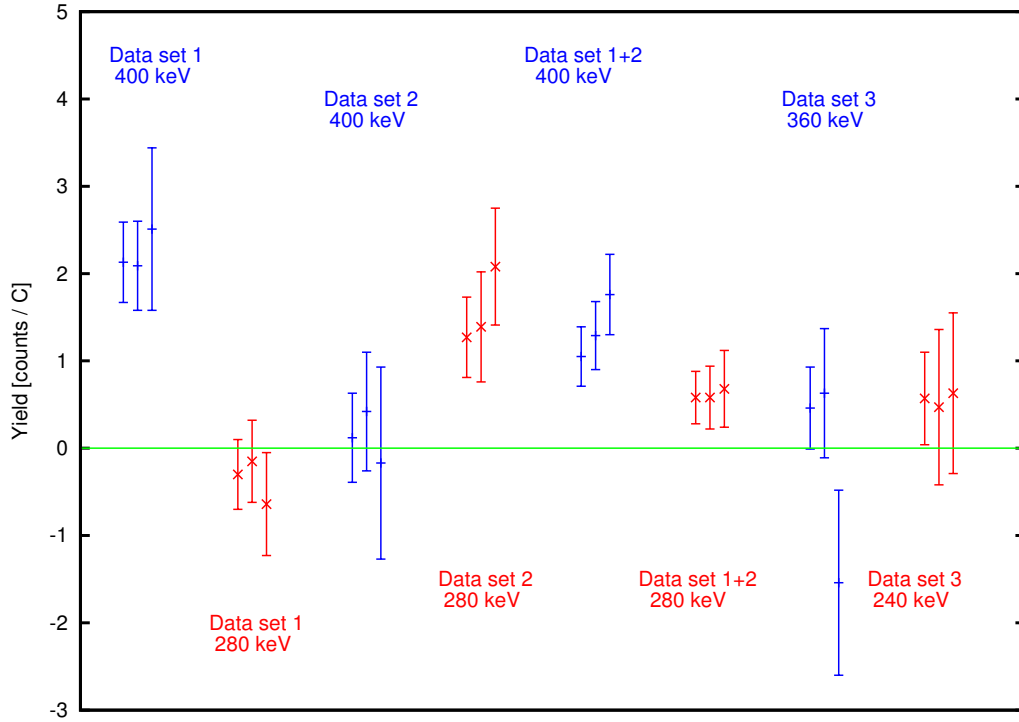
Figure 4.18.: Comparison of the calculated yields. The left bar always represents the result using the fit functions method, the middle the result of the weighted average method, and the right bar the result using the neighbouring flat region.

All three introduced methods to determine η deliver very similar results with quite different approaches. This leads to the conclusion that the problem is not located in the choice of the method or in the calculation of η and its errors, but in a possible fluctuation of η inside the ${}^2\mathrm{H}(\alpha,\gamma){}^6\mathrm{Li}$ region of interest which can not be assessed with flat regions from "outside". In the following section, several sources of such systematic errors are discussed.

4.4. Sources of systematic errors and their treatment

4.4.1. Compton edges

Compton edges and single or double escape peaks inside the ^{2}H$(\alpha,\gamma)^6$Li region of interest may cause systematic errors in the subtraction approach if their contribution to the beam induced background or their shape strongly depend on the beam energy.
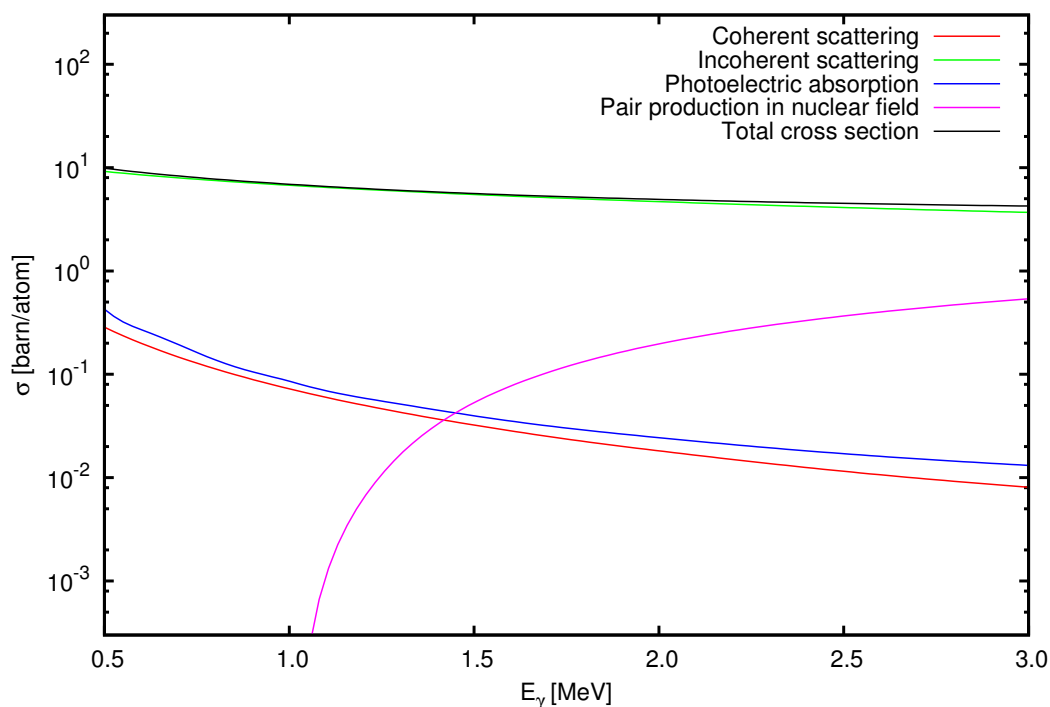
Figure 4.19.: Cross sections for different possible processes of γ-ray interaction with germanium depending on the γ-energy. Data taken from the XCOM database [42].

Incoherent (or Compton) scattering occurs on quasi-free electrons in outer shells of atoms. An incident photon transfers momentum to the electron which leaves the atom, and the wavelength of the secondary photon is increased. This interaction is the dominant one in the germanium detector for the interesting energy range of γ-rays (see figure 4.19). If the emitted photon leaves the active detector volume, the energy of the released electron is detected only. This energy depends on the emission angle of the secondary photon, causing a broad Compton continuum below the full energy peak in the γ-spectrum. In the extreme case of backward scattering, the electron

79

gets a maximum of energy, which appears as a sharp edge inside the γ-spectrum, up to $256\,\text{keV}$ below the full energy peak.

Assuming a Compton edge at the low end of the $^2\text{H}(\alpha,\gamma)^6\text{Li}$ region of interest at $E_{\text{C.e.}} = 1540\,\text{keV}$, the corresponding full energy peak would be located at

$$E_\gamma = \frac{E_{\text{C.e.}}}{2} + \sqrt{\frac{E_{\text{C.e.}}^2}{4} + \frac{E_{\text{C.e.}}\, m_{\text{e}}c^2}{2}} = 1763\,\text{keV} \qquad (4.19)$$

The upper limit to look for structures in the spectrum is obtained with $E_{\text{C.e.}} = 1625\,\text{keV}$, so $E_\gamma = 1850\,\text{keV}$. In this energy range $1763...1850\,\text{keV}$, only one distinct structure can be identified in the γ-spectra (see table 4.11). The peak at $E_\gamma = 1861.2\,\text{keV}$ ($E_{\text{C.e.}} = 1636.5\,\text{keV}$) may affect the flat region around $E_{\text{median}} = 1631.5\,\text{keV}$ and impair the precision of especially the third approach to determine η, which strongly relies on a correct value of this single flat region.

Position (keV)	Identified as	Transition	Compton edge (keV)
1810.8	$^{56}\text{Fe}(n,n'\gamma)$	$2658 \rightarrow 847$	1586.9
1861.2	$^{63}\text{Cu}(n,n'\gamma)$	$1861 \rightarrow 0$	1636.5

Table 4.11.: $^2\text{H}(\alpha,\gamma)^6\text{Li}$ regions of interest affected by Compton edges. The information about the transitions is taken from the ENSDF database [14].

As mentioned previously, the subtraction approach requires that the shape of the beam induced background shows no beam energy dependence inside the $^2\text{H}(\alpha,\gamma)^6\text{Li}$ regions of interest. If the counting rates of lines above these regions vary remarkably, their Compton edges and continuum may distort the yield determination, because the key requirement of the subtraction approach is not given anymore.

In table 4.12, the observed counting rates of all lines in table 4.11 are listed. No remarkable influence on the yield determination is expected from the peak at $1861.2\,\text{keV}$, as the counting rates within the data sets are equal and apparently independent from the beam energy. This is not the case for the $1810.8\,\text{keV}$ line, where a significant energy dependence in the counting rates is observed.

Neutrons excite ^{56}Fe nuclei to the $2658\,\text{keV}$ state, which decays in a cascade via emission of $1811\,\text{keV}$ and $847\,\text{keV}$ γ-rays. In figure 4.20, the Geant4-simulated energy spectrum of primary neutrons from the $^2\text{H}(d,n)^3\text{He}$ reaction in the target gas is plotted. At $400\,\text{keV}$ of beam energy, there are more neutrons available to reach or to exceed the energy which is necessary to populate the $2658\,\text{keV}$ level, and by this the energy dependence of the $1811\,\text{keV}$ counting rate can be explained.

	Data set 1		Data set 2		Data set 3	
Position	400 keV	280 keV	400 keV	280 keV	360 keV	240 keV
(keV)	cnts C^{-1}	cnts C^{-1}	cnts C^{-1}	cnts C^{-1}	cnts C^{-1}	cnts C^{-1}
1810.8	3.21±0.21	1.97±0.20	3.31±0.21	2.80±0.22	2.38±0.19	2.00±0.18
1861.2	2.47±0.17	2.25±0.16	2.79±0.18	2.80±0.19	2.50±0.17	2.36±0.16

Table 4.12.: Net counting rates of significant structures in the γ-spectra that could affect the yield determination through Compton edges.
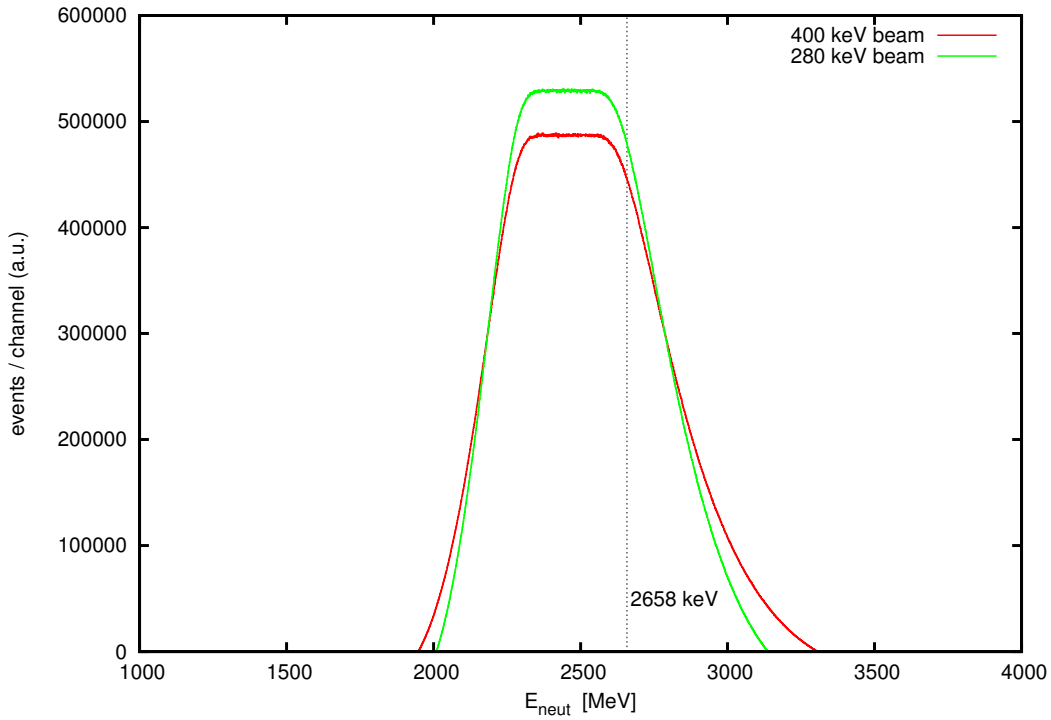
Figure 4.20.: Neutron energy spectra for 400 keV and 280 keV of beam energy, simulated by Geant4 for neutrons produced in the target gas. The dashed line represents the energy of the ^{56}Fe level which is populated before the emission of 1811 keV γ-rays.

The difference in the counting rates is less for data set 2. There are possible reasons for this observation, described in the following:

- An increasing deuteron density on steel surfaces (through implantation) created additional targets for the ^{2}H(^{2}H,n)^{3}He reaction. The overall neutron rate increased regardless of the beam energy, but the energy spectrum of additional

neutrons depends much less on the actual beam energy especially at high levels of implantation, because deuterons may first lose some energy in the surface before creating neutrons. The difference in the counting rates should become less significant by this.

- The beam induced background rate at high γ-energies (above 3 MeV) increased continuously with the applied charge, and was reduced remarkably after the exchange of many parts of the setup which were affected by implantation (section 4.2.1). Contaminated surfaces of the target chamber remained. If the high-energy background is due to energetic neutrons from the ^{3}H(d,n)^{4}He reaction, the influence of the beam energy on the neutron energy spectrum is less.

The Geant4 simulation is able to provide γ-spectra of single interaction processes which contribute to the measured spectrum. With a clean spectrum containing the contribution of the ^{56}Fe(n,n'γ) interaction only, a study of the Compton edge at 1586.9 keV would be possible, although the simulation seems to overestimate it (discussed in section 4.2.2). This spectrum is simulated as follows: Geant4 discards all tracks before the interaction with ^{56}Fe except the tracks of the primary neutrons and ^{3}He particles. After the interaction, Geant is allowed to follow all further tracks. Comparing such spectra obtained at two simulated beam energies reveals possible systematic errors caused by the Compton edge of the 1811 keV peak, a plot is shown in figure 4.21. The different counting rates of 1811 keV γ-rays are visible. The Compton edge appears right between the two main ^{2}H(α,γ)^{6}Li regions of interest, so possible systematics due to a different counting rate of the full energy peak will affect the 280 keV region of interest at most. The 400 keV region of interest is already affected by the shoulder of the Compton edge.

E_{beam} (keV)	1810.8 keV content	Events in the 400 keV ROI	% of full energy peak	Events in the 280 keV ROI	% of full energy peak
400	46676±220	6143±78	13.2±0.2	8517±92	18.2±0.2
280	36249±194	4773±69	13.2±0.2	6398±37	17.7±0.2

ratio $\left.\frac{N_{280\,\text{keV}}}{N_{400\,\text{keV}}}\right|_{1811\text{keV}} = 0.776 \pm 0.005$	measured, data set 1: 0.61±0.09
	measured, data set 2: 0.85±0.09

Table 4.13.: Compton background inside the ^{2}H(α,γ)^{6}Li regions of interest in relation to the 1811 keV full energy peak, using the modified Geant4 version and 4.0 billion simulated events.

Table 4.13 shows the amount of events in the ^{2}H(α,γ)^{6}Li regions of interest compared to the full energy peak content, reaching up to 17 %. Other components of the Compton background come from further ^{56}Fe(n,n'γ)-induced lines at 2085 keV and 2658 keV, this contribution is about one third of the total counting rate. The ratio

of 1811 keV peak contents for the two beam energies is more compatible with the measured values of data set 2, but hardly compatible with data set 1, although the values shown in figure 4.18 suggest that only the data set of run 1 delivers physical results. This is a strong hint that, if the simulation is used to determine systematic errors, this has to be done in a very conservative way.
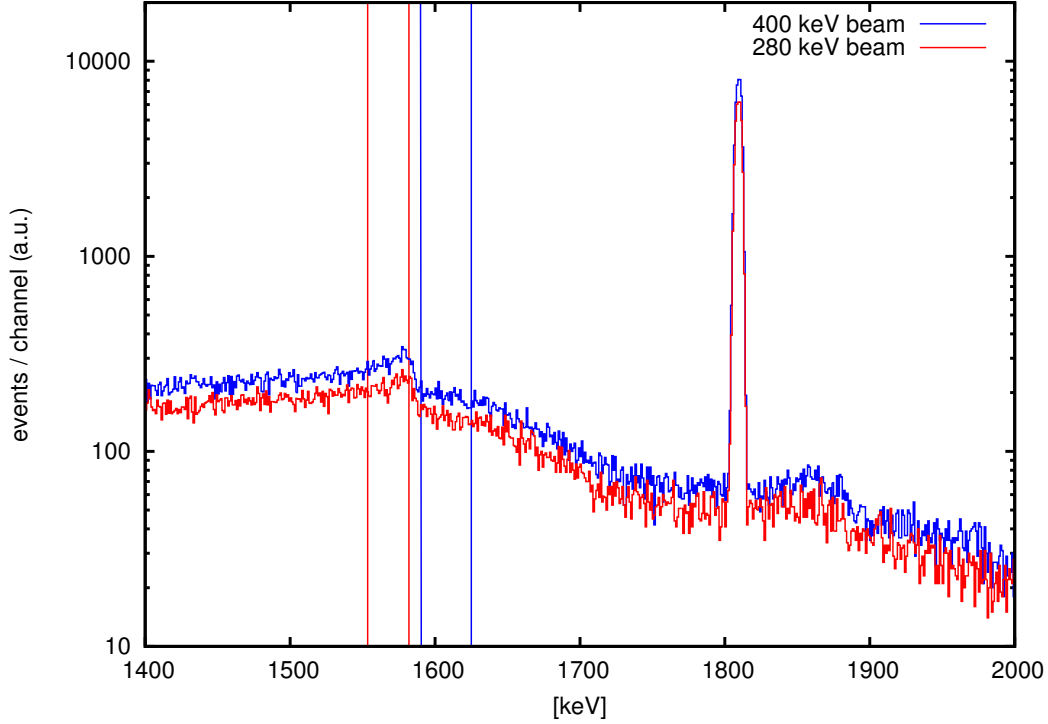
Figure 4.21.: The γ-spectrum for the same number of initial neutrons, but two different beam energies, calculated by a modified Geant4 simulation which considers ^{56}Fe(n,n'γ) interactions only. The ^{2}H(α,γ)^{6}Li regions of interest are marked with lines coloured according to the spectra.

In case of data set 1, the 1811 keV counting rate at 280 keV beam energy amounts to only 61±9 % compared to the 400 keV data. This impairs the background subtraction:

- Using the γ-spectrum obtained at 280 keV beam energy for the subtraction of the beam induced background at 400 keV, the ^{2}H(α,γ)^{6}Li yield will be overestimated: A small part of the background is not subtracted then.

- Subtracting a 400 keV spectrum from a one obtained at 280 keV leads to an even bigger underestimation of the 280 keV yield, because too much background is

subtracted. This effect should be smaller in data set 2, as the 1811 keV counting rates become more equal.

An appraisal of the necessary correction is now attempted. The overestimation of the 400 keV yield can be assessed by

$$\Delta Y_{400,\text{Edge}} = \frac{\kappa_{400}}{Q_{400}} \left(\frac{N_{1811,280\,\text{keV}}}{\eta(1607\,\text{keV})} - N_{1811,400\,\text{keV}} \right) \qquad (4.20)$$

with κ_{400} as the simulated ratio of the Compton background in the 400 keV $^2\text{H}(\alpha,\gamma)^6\text{Li}$ region of interest compared to the content of the 1811 keV full energy peak, in this case assumed to be a mean value of $\kappa_{400} = 13.3\,\%$ according to table 4.13. In case of data set 1, one obtains $\Delta Y_{400,\text{Edge}} = -0.16\ \text{C}^{-1}$.

The underestimation of the 280 keV yield is calculated similarly via

$$\Delta Y_{280,\text{Edge}} = \frac{\kappa_{280}}{Q_{280}} \left(\eta(1567\,\text{keV})\,N_{1811,400\,\text{keV}} - N_{1811,280\,\text{keV}} \right) \qquad (4.21)$$

with $\kappa_{280} = 16.9\,\%$, and $\Delta Y_{280,\text{Edge}} = 0.21\ \text{C}^{-1}$. In table 4.14 all results are collected.

Data set	$Y_{400\,\text{keV}}$ (C^{-1})	$\Delta Y_{400,\text{Edge}}$ (C^{-1})	$Y_{280\,\text{keV}}$ (C^{-1})	$\Delta Y_{280,\text{Edge}}$ (C^{-1})
1	2.13±0.46	-0.16	-0.27±0.42	+0.21
2	0.12±0.51	-0.07	1.57±0.47	+0.09
1+2	1.05±0.34	-0.13	0.71±0.31	+0.16

Table 4.14.: Corrections due to Compton edges to the yields calculated from the weighted average of fit functions. The same corrections would have to be applied for the other yield determination methods.

The corrections are smaller than the already given error bars, even though the κ values are somewhat overestimated (they include the Compton background of $^{56}\text{Fe}(\text{n,n'}\gamma)$ lines above 1811 keV). As a conclusion, these corrections have to be taken into account for the final yield estimation, but can not significantly change the deviating results in data set 2, they appear to be worse indeed. The errors of $\Delta Y_{400,\text{Edge}}$ and $\Delta Y_{280,\text{Edge}}$ are conservatively estimated to be 50 %.

The Compton continua of all further lines at higher γ-energies are already included by the flat regions method to parameterize the beam induced background continuum and need no further consideration here.

4.4.2. Escape peaks

Escape peaks may occur whenever the energy of incident photons exceed the threshold for the pair production process (1022 keV). This kind of photon interaction becomes

increasingly important at higher γ-energy, but in case of Ge it is still only up to a tenth of all interactions in the interesting energy range (see figure 4.19). In the strong electric field close to a Ge nucleus, a photon may be converted into an electron-positron pair. The positron is thermalized and annihilates with another electron, producing two γ-rays with an energy of 511 keV each. If both of them leave the detector without any further interaction inside the active volume, the kinetic energies of the primary electron and positron are detected only, and a peak located at 1022 keV below the full energy peak may grow, the double escape peak. Due to cases where only one of the 511 keV γ-rays escape, a single escape peak at 511 keV less than the full energy appears as well.

Position (keV)	Identified as	Transition	SE peak at (keV)	Affects ^{2}H$(\alpha,\gamma)^6$Li regions of interest
2081.4	^{63}Cu(n,n'γ)	$2081 \to 0$	1570	280 keV
2093±1	^{63,65}Cu(n,n'γ)	$2093(1) \to 0$	1582	360 keV, 280 keV

Table 4.15.: Significant lines in the γ-spectra that could affect the yield determination through single escape peaks. Transition data are taken from the ENSDF database [14].

Single escape peaks in the energy range of 1540...1625 keV could be caused by full energy peaks in the range of 2051...2136 keV. In table 4.15, two lines are listed that appear in the measured γ-spectra in this energy range. Problems for the subtraction approach arise if there are remarkable energy-dependent deviations in the counting rates within one data set, which is not the case (see table 4.16). Around $E_\gamma = 2$ MeV, single escape peaks are still small compared to the full energy peaks [36]. This is supported by the fact that the detector has a high detection efficiency, reducing the probability that γ-rays actually escape. Together with the low measured counting rates, one can conclude that single escape peaks have no remarkable influence on the ^{2}H$(\alpha,\gamma)^6$Li yield error estimation and need no further consideration here.

	Data set 1		Data set 2		Data set 3	
Position (keV)	400 keV cnts C^{-1}	280 keV cnts C^{-1}	400 keV cnts C^{-1}	280 keV cnts C^{-1}	360 keV cnts C^{-1}	240 keV cnts C^{-1}
2081.4	1.19±0.16	1.42±0.15	0.90±0.16	0.95±0.16	0.89±0.15	0.70±0.14
2093±1	0.59±0.11	0.81±0.13	0.88±0.13	1.04±0.13	0.80±0.12	0.78±0.11

Table 4.16.: Net counting rates of lines listed in table 4.15.

Analogous conclusions can be found for the double escape peak from the one distinct line in the energy range of 2562...2647 keV: It originates from ^{208}Pb(n,n'γ) and

is located at 2614.5 keV (transition 2615 → 0, ENSDF), with a possible double escape peak at 1592.5 keV, possibly affecting the ^{2}H$(\alpha,\gamma)^6$Li regions of interest at 400 keV and 360 keV beam energy. Due to the beam energy-independent counting rates and the high detection efficiency of the used detector, no influence of a possible double escape peak on the yield error is expected.

| Position | Data set 1 | | Data set 2 | | Data set 3 | |
| | 400 keV | 280 keV | 400 keV | 280 keV | 360 keV | 240 keV |
(keV)	cnts C^{-1}	cnts C^{-1}	cnts C^{-1}	cnts C^{-1}	cnts C^{-1}	cnts C^{-1}
2614.5	5.51±0.16	5.31±0.16	5.49±0.16	4.98±0.15	5.22±0.16	5.60±0.14

Table 4.17.: Net counting rates of significant lines in the γ-spectra that could affect the yield determination through double escape peaks.

4.4.3. The ^{65}Cu peak at 1623.4 keV

This line on the high-energy end of the 400 keV ^{2}H$(\alpha,\gamma)^6$Li region of interest originates from the 1623→0 transition in excited ^{65}Cu nuclei after inelastic neutron scattering. This level can be populated either directly, or as an intermediate level of a cascade (e.g. 2894→1623→0, ENSDF). Beam energy dependent counting rates of this line will directly affect the subtraction of the beam induced background. Table 4.18 shows the measured counting rates. Especially in data set 1, the values show a significant dependence from the beam energy. Before charge normalization, the difference is about 230 counts, that is already half of the determined 400 keV ^{2}H$(\alpha,\gamma)^6$Li signal in this data set.

| Position | Data set 1 | | Data set 2 | | Data sets 1+2 | |
| | 400 keV | 280 keV | 400 keV | 280 keV | 400 keV | 280 keV |
(keV)	cnts C^{-1}	cnts C^{-1}	cnts C^{-1}	cnts C^{-1}	cnts C^{-1}	cnts C^{-1}
1623.4	1.52±0.18	2.28±0.20	1.93±0.19	2.15±0.20	1.57±0.26	2.17±0.31

Table 4.18.: Net counting rates of the peak at 1623.5 keV due to the ^{65}Cu(n,n'γ) interaction.

To approach this problem, two options can be considered:

- The 400 keV region of interest is shortened to keep the 1623 keV peak outside. This would imply to suppress γ-rays from the collimator region. For geometrical reasons, it is not possible to assign a defined position along the beam path to the γ-energy cutoff value. Therefore, the final error bars may increase, but errors due to improper fitting of the 1623 keV peak will be avoided.

- The 400 keV region of interest is kept, but the influence of the ^{65}Cu peak is subtracted.

Following the second option, corrected numbers of 400 keV ^{2}H$(\alpha,\gamma)^6$Li events would be calculated via

$$D_{400,\text{corr}} = D_{400} - \left(N_{1623,400} - \frac{N_{1623,280}}{\eta} \right) \tag{4.22}$$

with

$$\Delta D_{400,\text{corr}} = \sqrt{ D_{400} + (\Delta N_{1623,400})^2 + \left(\frac{\Delta\eta \, N_{1623,280}}{\eta^2} \right)^2 + \left(\frac{\Delta N_{1623,280}}{\eta} \right)^2 } \tag{4.23}$$

$N_{1623,\text{E}_{\text{beam}}}$ are net contents of the 1623 keV peak after subtraction of the background continuum. The results are shown in table 4.19. The corrections increase the 400 keV yield in general, but worsen the differences between the results of data sets 1 and 2.

	Data set 1		Data set 2		Data sets 1+2	
Method	Y_{400} cnts C^{-1}	$Y_{400,\text{corr}}$ cnts C^{-1}	Y_{400} cnts C^{-1}	$Y_{400,\text{corr}}$ cnts C^{-1}	Y_{400} cnts C^{-1}	$Y_{400,\text{corr}}$ cnts C^{-1}
1	1.92±0.97	2.76±1.01	0.14±1.06	0.51±1.10	1.00±0.80	1.71±0.83
2	1.97±1.73	2.82±1.76	0.40±2.09	0.79±2.12	1.21±1.59	1.93±1.61
3	2.38±0.93	3.27±0.97	-0.15±1.10	0.20±1.14	1.70±0.46	2.47±0.51

Table 4.19.: Charge normalized yield values compared before and after correction for the energy dependent counting rate of 1623.5 keV γ-rays due to the ^{65}Cu(n,n'γ) interaction.

This approach is not followed, but the peak at 1623 keV is excluded from the 400 keV ^{2}H$(\alpha,\gamma)^6$Li region of interest for two reasons:

- The full energy peak detection efficiency for γ-rays from the collimator region could not be measured, but estimated only, so excluding the 1623 keV peak may open the possibility to reduce the uncertainty.

- There are doubts on the correct determination of the net content of the 1623 keV peak, as it is partially affected by the ^{2}H$(\alpha,\gamma)^6$Li signal at a beam energy of 400 keV. Systematic errors in the correct subtraction of the background below the peak are likely to occur, which moreover changes its shape depending on the beam energy. Hence, the peak area is excluded in the further considerations, and the upper bound of the 400 keV ^{2}H$(\alpha,\gamma)^6$Li region of interest is chosen to be at $E_\gamma = 1621$ keV.

4.4.4. Neutron capture on ^{56}Fe

Due to the ^{2}H(^{2}H,n)^{3}He reaction, a flux of fast neutrons is induced. The setup consists at most of materials with $A > 50$, so neutrons are scarcely moderated until they reach the outer shielding which is a layer of borated polyethylene. However, clear evidence for the occurrence of neutron capture processes inside the inner components of the setup is the presence of a ^{71m}Ge line in the in-beam γ-spectrum. The auxiliary experiment using neutrons from the ^{2}H(^{2}H,n)^{3}He reaction at the DT-generator inside the ELBE facility (see section 3.7) yielded a strong γ-line at 1612 keV and the proof that this line is due to neutron capture of ^{56}Fe, the most abundant iron isotope. Hence, it is necessary to check whether this process influenced the LUNA ^{2}H(α,γ)^{6}Li measurements, as many parts of the setup consist of steel.

The absolute number of neutrons which have interacted with the HPGe detectors has been comparable in both experiments, but their characteristics were different: At LUNA, a neutron field from a weak source close to the γ-detector interacted with a comparably small amount of iron close to the detector. At ELBE, a neutron field from a strong source far from the γ-detector interacted with a comparably large amount of iron far from the detector. The resulting γ-spectra are hardly comparable. In table 4.20, the search for characteristic γ-rays of the ^{56}Fe(n,γ)^{57}Fe reaction with thermal neutrons, reported in [47], in both experimental γ-spectra is documented:

E_γ (keV)	I_γ (%)	Visible in ELBE, or	in LUNA γ-spectra
352	9.5	^{214}Pb line at the same position	unclear (same reason)
692	4.8	dominated by ^{74}Ge(n,n'γ) peak	unclear (same reason)
1019	1.8	yes	no
1261	2.6	yes	no
1613	5.4	yes	no
1725	6.3	^{65}Cu(n,n'γ) line at the same position	unclear (same reason)
3413	1.6	yes	no
3436	1.6	yes	no
7631	29	yes (including escape peaks)	no
7646	25	yes (including escape peaks)	no

Table 4.20.: Search for evidences for the ^{56}Fe(n,γ)^{57}Fe reaction in measured γ-spectra, using experimental results with thermal neutrons [47].

The contribution of the ^{56}Fe(n,γ)^{57}Fe reaction to the LUNA beam induced background is apparently negligible. Furthermore, as neutrons are usually thermalized before being captured, this process should be nearly independent from the beam energy, and signatures from the ^{56}Fe(n,γ)^{57}Fe reaction will be largely subtracted after normalization. Hence, this interaction will not be considered further.

4.4.5. Other sources of systematic errors

During the LUNA ^{2}H$(\alpha,\gamma)^6$Li data taking, some parameters varied between single runs. This may have caused additional systematic errors, which are briefly discussed in the following:

- Beam focus and intensity. The areas that were touched or hit by the α-beam changed within a single run, as the beam focus and its intensity inevitably varied. Furthermore, it was not possible to restore a set of standard initial conditions in the beginning of a measurement. Hence, the beam intensity on surfaces in contact with deuterium, such as the target collimator and the beam stop, varied, with an unknown effect on the beam induced background.

- Run duration. The range of measurement durations is between two hours and five days of continuous operation. It has been observed that the event rate per beam charge is lower in general when the duration of a run is in the order of days. The processes of implantation, hydrogen and helium diffusion in metals or gas adsorption inside the setup are not well understood, and the same is true for the amount of time needed to reach equilibria.

- Target gas. There are indications that the $400\,\mathrm{keV}$ ^{2}H$(\alpha,\gamma)^6$Li event rate dropped and the $280\,\mathrm{keV}$ rate rose after the exchange of the deuterium bottle at the end of the data set 1 measurements. If, through a leak, the target gas became contaminated with air, or the new deuterium contained impurities, the region of interest could have been shifted to lower γ-energies, or the shape of the beam induced background could have changed through additional interactions. Nevertheless, a decrease in the beam induced background (and the neutron) rate has not been observed.

- Works on the setup. Before each period of data taking, major works on the setup and on the electronic chain have been necessary, and many parts of the setup had to be dismounted. It can not be excluded that these works have caused unknown systematic errors.

4.4.6. Combination of different data sets

So far the subtraction of beam induced background has been done only within one data set, to avoid possible systematic errors due different deuteron implantation levels or other changed setup conditions. Now it is attempted to combine spectra of different data sets. In order to simplify the analysis, method 2 has been used (weighted average of neighbouring data points). The combinations are:

- Subtraction of the 280 keV beam induced background, data set 2, from the 400 keV beam induced background, data set 1.
  Results: $Y_{400\,\text{keV}} = (1.10 \pm 0.54)\,\text{C}^{-1}$ $\qquad Y_{280\,\text{keV}} = (1.02 \pm 0.61)\,\text{C}^{-1}$

- Subtraction of the 280 keV beam induced background, data set 1, from the 400 keV beam induced background, data set 2.
  Results: $Y_{400\,\text{keV}} = (1.59 \pm 0.73)\,\text{C}^{-1}$ $\qquad Y_{280\,\text{keV}} = (0.16 \pm 0.56)\,\text{C}^{-1}$

- Subtraction of the 240 keV beam induced background, data set 3, from the 400 keV beam induced background, data set 2.
  Results: $Y_{400\,\text{keV}} = (1.17 \pm 0.93)\,\text{C}^{-1}$ $\qquad Y_{240\,\text{keV}} = (0.63 \pm 0.92)\,\text{C}^{-1}$

- Subtraction of the 280 keV beam induced background, data set 1, from the 360 keV beam induced background, data set 3.
  Results: $Y_{360\,\text{keV}} = (0.97 \pm 0.63)\,\text{C}^{-1}$ $\qquad Y_{280\,\text{keV}} = (0.08 \pm 0.61)\,\text{C}^{-1}$

Comparing the results with the values in table 4.10, it appears that something is "wrong" with the 280 keV spectrum of data set 2 only, but the error bars are large, and all values are compatible if one includes their statistical errors in the considerations.

For a further check, spectra obtained at the same beam energy are subtracted. If there are no deviations between the single data sets, yield values compatible with zero should be obtained:

- Subtraction of the 280 keV beam induced background, data set 2, from the 280 keV beam induced background, data set 1.
  Results: $Y_{280\,\text{keV},1} = (-0.99 \pm 0.54)\,\text{C}^{-1}$ $\qquad Y_{280\,\text{keV},2} = (1.23 \pm 0.66)\,\text{C}^{-1}$

- Subtraction of the 400 keV beam induced background, data set 2, from the 400 keV beam induced background, data set 1.
  Results: $Y_{400\,\text{keV},1} = (0.71 \pm 0.64)\,\text{C}^{-1}$ $\qquad Y_{400\,\text{keV},2} = (-0.86 \pm 0.78)\,\text{C}^{-1}$

These results confirm the hypothesis of a strongly variable normalization factor $\eta(E_\gamma)$ inside the $^2\text{H}(\alpha,\gamma)^6\text{Li}$ regions of interest, which can not be assessed with information obtained from regions outside. Furthermore, the deviation in the shape of the beam induced background between the single data sets is apparent, which is much stronger in the 280 keV region of interest.

4.5. Final yield values and discussion

Two conclusions arise from the data analysis: First, each data set has to be analyzed independently, and a subtraction of the beam induced background has to be done within the same data set only; and second, the error bars of the normalization factor $\eta(E_\gamma)$ are not large enough to resolve the contradictions between the values of data

sets 1 and 2. Only tenfold increased error bars on η would provide that. Therefore, the normalization factors are not directly usable, and a way to continue the data analysis without them has to be found. This is also illustrated in figures 4.22 and 4.23, where the results of the first method to determine $\eta(E_\gamma)$ are applied to the γ-spectra of different data sets. The clear excess in the 400 keV region of interest in data set 1 has moved to the 280 keV region of interest in data set 2, while the normalisation itself has been done correctly (see figure 4.23).
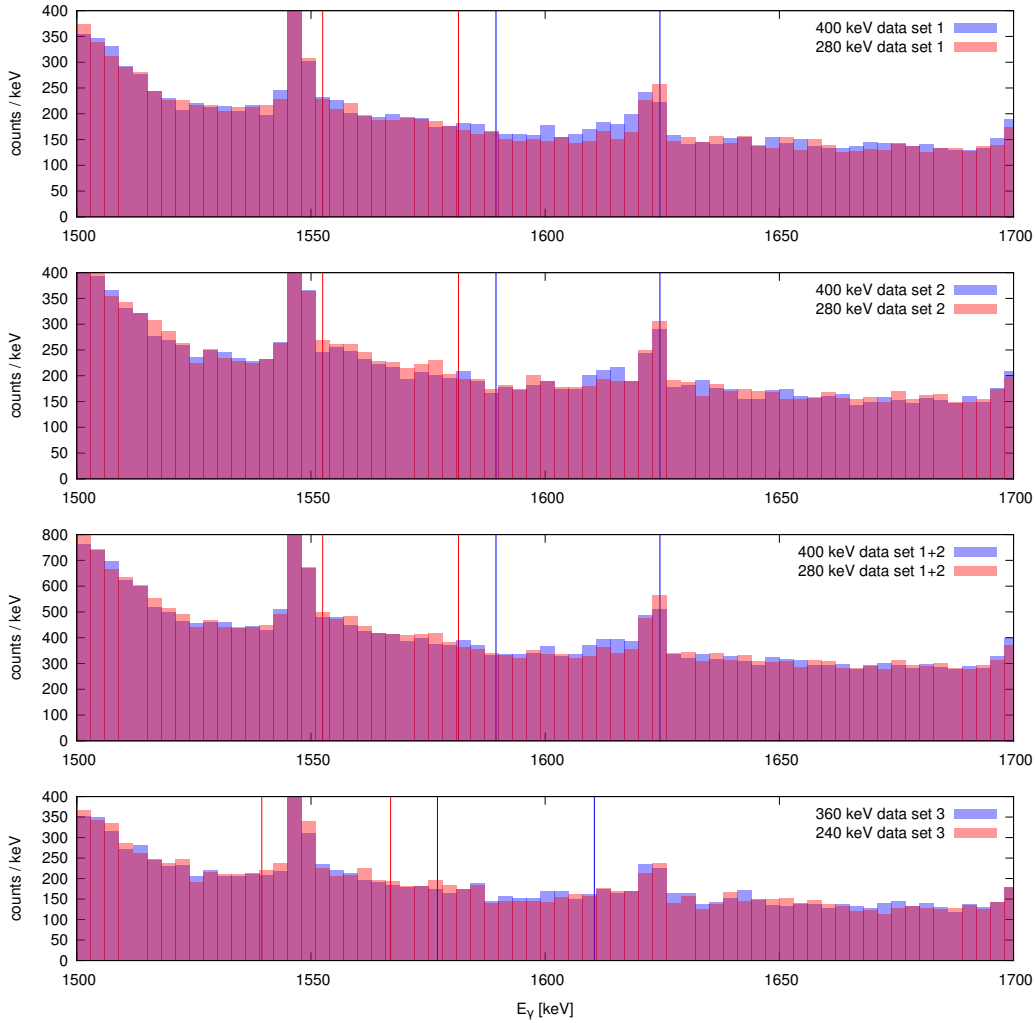
Figure 4.22.: The γ-spectra after normalization. The ^{2}H(α,γ)^{6}Li regions of interest are marked according to the color of the histogram.
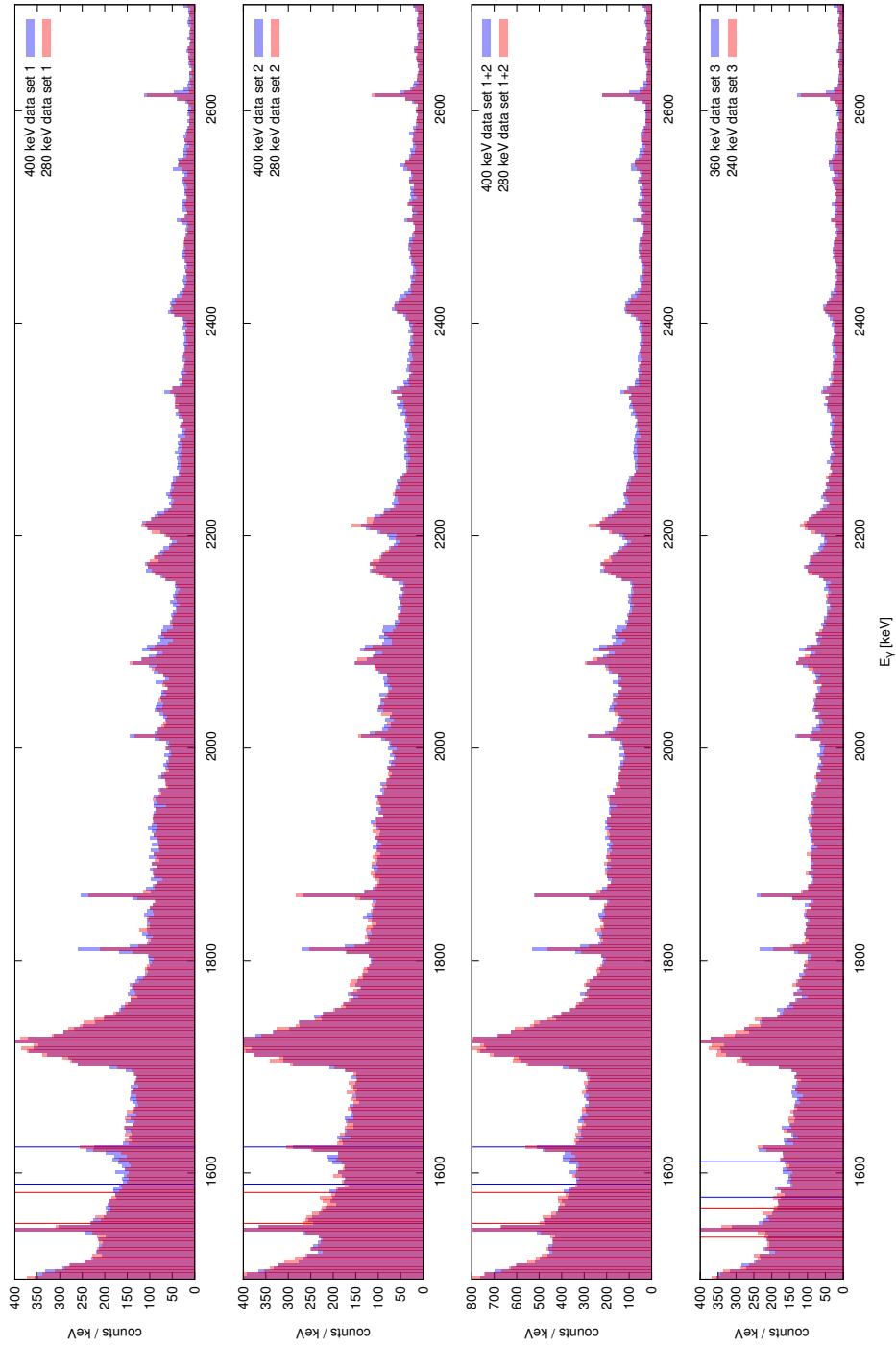
Figure 4.23.: The same plot as in figure 4.22, but with an extended range of γ-energies.

Regardless of the actual behaviour of $\eta(E_\gamma)$ in the regions of interest: If $^2\mathrm{H}(\alpha,\gamma)^6\mathrm{Li}$ signals exist and can not be extracted due to an uncertain normalization, still the sum of the signals is constant. In the present analysis method, the value of $\eta(E_\gamma)$ is nearly constant within the $^2\mathrm{H}(\alpha,\gamma)^6\mathrm{Li}$ regions of interest, and their width W is similar, regardless of the beam energy. If now, due to a shift in the normalization factor $\eta + \delta\eta$, the excess D_1 will be shifted as

$$D_1^* = D_1 + W\delta\eta \tag{4.24}$$

the amount of additional events will be missing in the other region of interest:

$$D_2^* = D_2 - W\delta\eta \tag{4.25}$$

In any case, the sum remains constant:

$$D_1^* + D_2^* = D_1 + W\delta\eta + D_2 - W\delta\eta = D_1 + D_2 \tag{4.26}$$

In this way, the influence of the normalization factor $\eta(E_\gamma)$ is removed, but only the sum of two signals can be reliably obtained from the measurement.

The final yield values are calculated using the first normalization method which parameterizes the beam induced background using flat regions. This method gives the smallest statistical errors. The yield values are corrected for the influence of the Compton edge of the 1811 keV $^{56}\mathrm{Fe}$ peak (as it is described in section 4.4.1). In case of the data sets obtained at beam energies of 400 keV and 280 keV, the $^{65}\mathrm{Cu}(\mathrm{n,n'}\gamma)$ peak and for the beam energy-dependent counting rate of the 1623 keV $^{65}\mathrm{Cu}(\mathrm{n,n'}\gamma)$ peak at 1623.4 keV is excluded from the 400 keV region of interest, which now ends at $E_\gamma = 1621.0$ keV. The results are listed in table 4.21.

		corrected		sum	
Data set	Beam energy (keV)	Y_{corr} (C^{-1})	Error ΔY_{corr} (C^{-1})	Yield Y_{sum} (C^{-1})	Error ΔY_{sum} (C^{-1})
1	400	1.99	0.42	1.91	0.60
1	280	-0.08	0.43		
2	400	0.28	0.47	1.92	0.67
2	280	1.64	0.47		
3	360	0.40	0.47	1.17	0.71
3	240	0.78	0.53		

Table 4.21.: $^2\mathrm{H}(\alpha,\gamma)^6\mathrm{Li}$ yields and yield sums after correction for the Compton background of the 1811 keV $^{56}\mathrm{Fe}$ peak, and excluding the 1623 keV $^{65}\mathrm{Cu}(\mathrm{n,n'}\gamma)$ peak. The results for other η determination methods are given in Appendix A.3.

All yield sums are comparable within its error bars, but the central values show physical results and are even equal in the case of the $400\,\mathrm{keV}/280\,\mathrm{keV}$ data sets. Still, no absolute yield values for specific beam energies can be extracted. However, if the energy dependence of the S-factor, known from theoretical calculations, is included, single S-factor values can be extracted. This is described in the following chapter.

5. Deriving the S-factor

In this chapter, the calculation of the ^{2}H(α,γ)^{6}Li S-factor for all four data points at $E_{\text{CMS}} = 133\,\text{keV}$, $E_{\text{CMS}} = 120\,\text{keV}$, $E_{\text{CMS}} = 93\,\text{keV}$ and $E_{\text{CMS}} = 80\,\text{keV}$ is performed.

5.1. Basic considerations

According to ICRU 85 [48], the cross section of a target entity is given by

$$\sigma = \frac{N}{\Phi} \tag{5.1}$$

where N is the number of interactions per target entity, and Φ the fluence of incident particles. The fluence in a specific target entity in the LUNA gas target can be expressed as follows:

$$\Phi = n\,l\,\frac{Q}{e} \tag{5.2}$$

with n being the target density (cm^{-3}), l the length of the entity, and Q/e the absolute number of incident particles. The measured signal D inside the γ-detector depends on the detection efficiency ϵ, hence $D = \epsilon\,N$, and with $Y = D/Q$,

$$\sigma = \frac{Y\,e}{\epsilon\,n\,l} \tag{5.3}$$

follows. The target density is given by the number of target nuclei N_T per volume, and one finds

$$n = \frac{N_T}{V} = \frac{p\,N_T}{p\,V} \stackrel{\text{ideal gas, D}_2}{=\!=\!=} \frac{2\,p\,N_T}{N_T\,k_B\,T} \stackrel{\text{beamheating}}{=\!=\!=} \frac{2\,p}{k_B\,(T + \Delta T)} \tag{5.4}$$

Hence, one obtains

$$\sigma(E) = \frac{Y(E)\,e\,k_B\,(T + \Delta T)}{2\,\epsilon\,p\,l} \tag{5.5}$$

The astrophysical S-factor can be expressed as (see [49])

$$S(E) = \sigma(E)\,E\,\exp\left(0.989534\,Z_1\,Z_2\,\sqrt{\frac{1}{E}\frac{m_\alpha\,m_d}{m_\alpha + m_d}}\right) \tag{5.6}$$

Here and in the following, already center of mass-energies $E = E_{\text{CMS}}$ are used.

Finally, one finds

$$S(E) = \frac{Y(E)\, e\, k_B\, (T + \Delta T)\, E}{2\epsilon\, p\, l} \exp(2.290833\, E^{-1/2}) \qquad (5.7)$$

with the assumption that the masses m_α and m_d (taken from [13]) as well as the elementary charge e and the Boltzmann constant k_B (taken from [50]) are exact values. Six error-prone quantities remain: $Y(E)$, $T + \Delta T$, E, ϵ, p and l. As there are no correlations between them, the uncertainty of $S(E)$ can be calculated via

$$\Delta S(E) = \sqrt{\sum_f \left(\frac{\partial S(E)}{\partial f} \Delta f\right)^2} \qquad (5.8)$$

with six terms inside the square root. Each one of them is discussed in the following section, considering an averaged gas target.

5.2. The averaged gas target

1. Yield Y. Through the summation of single yields (as introduced in section 4.5), systematic errors due to a wrong normalization factor are removed, and the remaining uncertainty is of statistical nature. As the statistical uncertainty accounts for 30 % or more, this error gives the biggest contribution to the final uncertainty (table 5.2).

   The beam current has been calculated according to equation (3.1). The power values were logged ten times per minute, determined from the analog output of the calorimeter power supply which was read out by LabView via a FieldPoint unit. During the ^{3}He$(\alpha,\gamma)^7$Be experiment, the calorimeter had been calibrated in a similar setup, using the entire target chamber as a Faraday cup with a negative secondary electron suppression voltage on the target collimator. The beam current calculated from the power values was then compared to the measured current from the target chamber to the ground.

   Before and after a single ^{2}H$(\alpha,\gamma)^6$Li run, the calorimeter power without beam has been measured (usually averaging the data points of a few minutes). The stored power values during the ^{2}H$(\alpha,\gamma)^6$Li measurement were averaged as well to calculate the average power with beam. Together with the stopping correction in equation (3.1), the beam current has been determined. Its systematic uncertainty is assumed to the same as during the ^{3}He$(\alpha,\gamma)^7$Be measurements, being 1.5 % [51], so the systematic error on the beam charge and hence the yield is assumed to be 1.5 % as well.

2. Target length l. If the γ-detector would be point-like, every γ-energy at a given beam energy would be related to emission of γ-rays at a defined position. Due to

the large size of the germanium crystal and the energy resolution of the detector, the point of emission becomes uncertain. Towards the beam stop, the gas target as a defined end, but this is not the case inside the target collimator, where the gas pressure increases linearly along the beam path. Hence, the uncertainty of the target length is estimated to be 5 mm, and $l = (192 \pm 5_{\text{syst}})$ mm. In case of the 400 keV region of interest which has a reduced upper bound of 1621 keV, the target length is estimated to $l = (177 \pm 10_{\text{syst}})$ mm.

3. Gas temperature $T + \Delta T$. The calculation of an average gas temperature $\overline{T}$ and the beam heating correction ΔT have been discussed in section 3.2.2. The average temperature is assumed to be the same for all data sets, while the beam heating correction is calculated for each data set individually from the average beam current and the stopping power values. The uncertainty is assumed to be $\Delta(T + \Delta T)_{\text{syst}} = 10$ K.

4. Full-energy peak detection efficiency ϵ. The determination of $\epsilon(x)|_{E_\gamma = 1600\,\text{keV}}$ and of the corresponding uncertainties is described in section 3.4. It was not possible to place radioactive sources on the beam path very close to the beam stop and inside the target collimator, hence values for $\epsilon(x)|_{E_\gamma = 1600\,\text{keV}}$ on these positions have been estimated by extrapolation of the existing data points, with an assigned uncertainty of 50 %. As an error of the average full-energy peak detection efficiency $\overline{\epsilon}$, the average of the relative errors of all data points has been chosen:

$$\Delta \overline{\epsilon} = \frac{1}{n} \sum_{i=1}^{n} \frac{\Delta \epsilon_i}{\epsilon_i} \tag{5.9}$$

The result is $\overline{\epsilon} = (1.52 \pm 0.19_{\text{syst}})$ % and in case of a beam energy of 400 keV, $\overline{\epsilon} = (1.64 \pm 0.20_{\text{syst}})$ %.

5. Target pressure p. As stated in section 3.2.1, the gas target pressure has been very stable in time. It has been stored every 30 s by a permanently running LabView application which used the analog output of the MKS controller. The zero calibration of the Baratron gauge has been done with a well evacuated target chamber, and a linearity error of 0.25 % is stated in the data sheet. As the controller output had to be digitized and converted to a pressure value, the systematic error is conservatively assumed to be 1 %. From the average pressure values of single runs, $\overline{p} = (0.306 \pm 0.003_{\text{syst}} \pm 0.006_{\text{stat}})$ mbar is obtained.

6. Beam energy E. The LUNA2 accelerator provides a beam with a highly stable energy, any fluctuations are negligible. However, the α-particles lose energy through stopping in the target gas, a few keV depending on the beam energy (discussed in section 3.2.2). Since the γ-detector is located below the center of the gas target, the α-particles have lost half of the total energy loss ΔE_α

Quantity f	$\left\|\frac{\partial \sigma(E)}{\partial f} \Delta f\right\|_{E_\alpha = 400\,\text{keV}}$ (10^{-12} barn)	$\left\|\frac{\partial \sigma(E)}{\partial f} \Delta f\right\|_{E_\alpha = 280\,\text{keV}}$ (10^{-12} barn)
Efficiency ϵ	7.1_{syst}	2.2_{syst}
Target pressure p	0.6_{syst} $\qquad$ 1.1_{stat}	0.2_{syst} $\qquad$ 0.4_{stat}
Target length l	3.3_{syst}	0.5_{syst}
Gas temperature $T + \Delta T$	1.8_{syst}	0.6_{syst}
Yield Y	2.8_{syst} $\qquad$ 18.2_{stat}	2.6_{syst} $\qquad$ 5.6_{stat}

Table 5.2.: Contributions to the error of the cross section $\sigma(E)$ for the case of data set 1.

when being above the γ-detector. Hence, for the calculation of the S-factor, the particle energy at this point with the maximum γ-detection efficiency is used:

$$E_{\text{lab,analysis}} = E_{\text{nominal}} - \frac{\Delta E_\alpha}{2} \tag{5.10}$$

The uncertainty is assumed to be

$$\Delta E_{\text{lab,analysis}} = \frac{\Delta E_\alpha}{2} \tag{5.11}$$

The values are listed in table 5.1. The uncertainty of the α-particle energy is regarded as being systematic as well.

Data set	E_{nominal} (keV)	$\Delta E/2$ (keV)	$E_{\text{lab,analysis}}$ (keV)	$E_{\text{CMS,analysis}}$ (keV)	ΔE_{CMS} (keV)
1	400	1.6	398.4	133.4	0.5
1	280	1.4	278.6	93.3	0.5
2	400	1.5	398.5	133.4	0.5
2	280	1.4	278.6	93.3	0.5
3	360	1.5	358.5	120.0	0.5
3	240	1.3	238.7	79.9	0.4

Table 5.1.: α-particle energies and uncertainties used for the calculation of the S-factor.

In table 5.2, the single contributions to the total error of the cross section $\sigma(E)$ are listed for the case of data set 1. Compared to the statistical error of the yield, all systematic errors are of minor importance.

5.3. The energy dependence of the S-factor at low energies in theory

As only the sum of yields can be extracted from a single data set, the ratio between them has to be inferred from the trend of the S-factor given by theoretical assumptions. A ratio χ between S-factors at two energies is defined as

$$\frac{S(E_1)}{S(E_2)} =: \chi \tag{5.12}$$

Using equation (5.7), the yield ratio λ can be derived:

$$\frac{Y(E_1)}{Y(E_2)} =: \lambda = \chi \, \frac{\epsilon_1 \, p_1 \, l_1 \, (T + \Delta T)_2 \, E_2}{\epsilon_2 \, p_2 \, l_2 \, (T + \Delta T)_1 \, E_1} \exp\left[\kappa \left(E_2^{-1/2} - E_1^{-1/2} \right) \right] \tag{5.13}$$

with

$$\kappa = 0.989534 \, Z_1 \, Z_2 \, \sqrt{\frac{m_\alpha \, m_d}{m_\alpha + m_d}} \tag{5.14}$$

The S-factor values used are taken from the most recent indirect measurement at the GSI [15]. As the angular distribution of $^2\mathrm{H}(\alpha,\gamma)^6\mathrm{Li}$ γ-rays in the direct LUNA experiment is unknown, the total GSI S-factor, which is the sum of contributions from the E1 and E2 transitions, is employed.

The available single data points of the GSI data are fitted in a limited energy region around the LUNA data points ($E_{\mathrm{CMS}} = 50...160\,\mathrm{keV}$), using a second order polynomial (see figure 5.1). The obtained function is used to calculate χ values according to the definition (5.12), assuming them to be without any uncertainty.

Apart from the GSI data, there are other theoretical calculations which have been mentioned in chapter 2. Taking into account the high uncertainty which arises from the discrepancies between the different models and the unknown angular distribution, a constant total S-factor is assumed in a second analysis, which immediately sets the ratio $\chi = 1$.

With this input, the values for λ are determined. The uncertainty $\Delta\lambda$ is calculated analogous to equation (5.8) both for statistical and systematic errors. Finally, with the yield sums Y, one obtains

$$Y(E_1) = \frac{\lambda Y}{\lambda + 1} \quad \text{and} \quad \Delta Y(E_1) = \sqrt{\left(\frac{\lambda \, \Delta Y}{\lambda + 1} \right)^2 + \left(\frac{\Delta\lambda \, Y}{(\lambda + 1)^2} \right)^2} \tag{5.15}$$

$$Y(E_2) = \frac{Y}{\lambda + 1} \quad \text{and} \quad \Delta Y(E_2) = \sqrt{\left(\frac{\Delta Y}{\lambda + 1} \right)^2 + \left(\frac{\Delta\lambda \, Y}{(\lambda + 1)^2} \right)^2} \tag{5.16}$$

The results are listed in tables 5.3 and 5.4 for all data sets and for both theoretical models. Due to the calculation method, the obtained yield values $Y(E_1)$ and $Y(E_2)$ and hence the S-factors $S(E_1)$ and $S(E_2)$ within one data set are correlated.
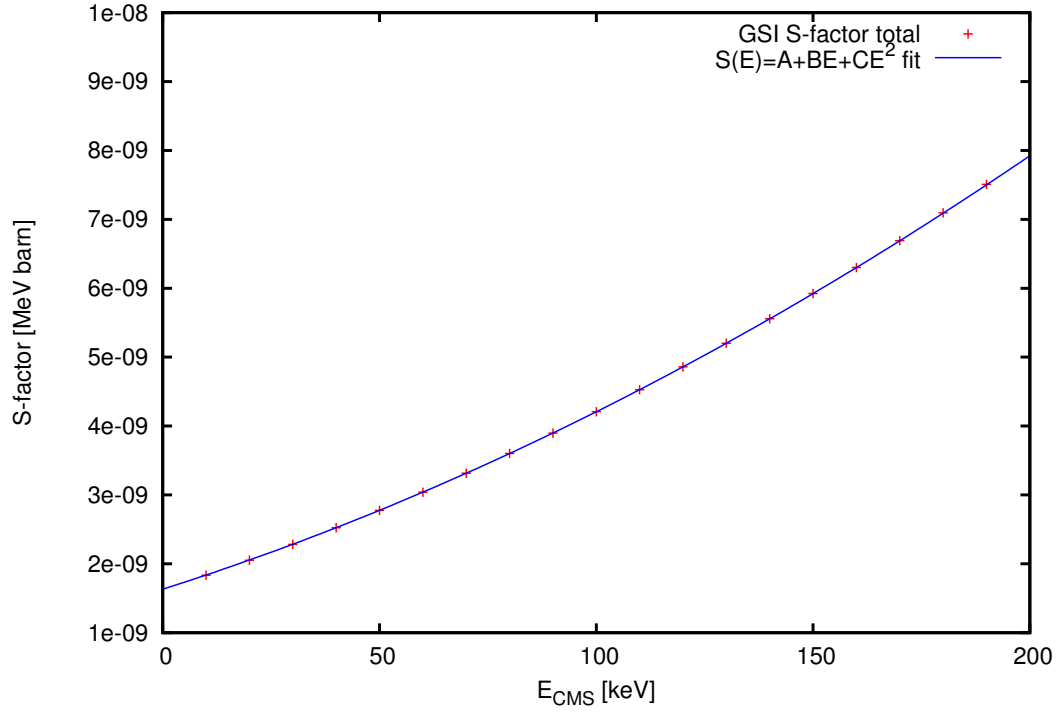
Figure 5.1.: Fit of the theoretical S-factor curve with a polynomial function.

Data set	E_{CMS} (keV)	$S(E)_{\mathrm{GSI}}$ (MeV nb)	χ_{GSI}	λ_{GSI}	$\lambda_{\chi=1}$
1	133.4 93.3	5.32 4.00	1.33	$3.19 \pm 0.61_{\mathrm{syst}} \pm 0.09_{\mathrm{stat}}$	$2.40 \pm 0.46_{\mathrm{syst}} \pm 0.07_{\mathrm{stat}}$
2	133.4 93.3	5.32 4.00	1.33	$3.18 \pm 0.61_{\mathrm{syst}} \pm 0.09_{\mathrm{stat}}$	$2.39 \pm 0.46_{\mathrm{syst}} \pm 0.07_{\mathrm{stat}}$
3	120.0 79.9	4.86 3.60	1.35	$4.04 \pm 0.76_{\mathrm{syst}} \pm 0.11_{\mathrm{stat}}$	$2.99 \pm 0.56_{\mathrm{syst}} \pm 0.08_{\mathrm{stat}}$

Table 5.3.: χ- and λ-values for different theoretical S-factor trends at low energies.

5.4. Derived S-factor values and errors

The S-factors and their errors are calculated according to equations (5.7) and (5.8). The results are provided in table 5.6 and are compared to the GSI data in figures 5.2 and 5.3.

		$\chi = \chi_{\text{GSI}}$	$\chi = 1$
Data set	E_{CMS} (keV)	$Y(E)$ (Coulomb^{-1})	$Y(E)$ (Coulomb^{-1})
1	133.4	$1.46 \pm 0.07_{\text{syst}} \pm 0.46_{\text{stat}}$	$1.35 \pm 0.08_{\text{syst}} \pm 0.42_{\text{stat}}$
	93.3	$0.46 \pm 0.07_{\text{syst}} \pm 0.14_{\text{stat}}$	$0.56 \pm 0.08_{\text{syst}} \pm 0.18_{\text{stat}}$
2	133.4	$1.46 \pm 0.07_{\text{syst}} \pm 0.51_{\text{stat}}$	$1.35 \pm 0.08_{\text{syst}} \pm 0.47_{\text{stat}}$
	93.3	$0.46 \pm 0.07_{\text{syst}} \pm 0.16_{\text{stat}}$	$0.57 \pm 0.08_{\text{syst}} \pm 0.20_{\text{stat}}$
3	120.0	$0.94 \pm 0.04_{\text{syst}} \pm 0.57_{\text{stat}}$	$0.88 \pm 0.04_{\text{syst}} \pm 0.53_{\text{stat}}$
	79.9	$0.23 \pm 0.04_{\text{syst}} \pm 0.14_{\text{stat}}$	$0.29 \pm 0.04_{\text{syst}} \pm 0.18_{\text{stat}}$

Table 5.4.: Final yield values for $\chi = \chi_{\text{GSI}}$ and $\chi = 1$.

		$\chi = \chi_{\text{GSI}}$	$\chi = 1$
Data set	E_{CMS} (keV)	$\sigma(E)$ (picobarn)	$\sigma(E)$ (picobarn)
1	133.4	$58 \pm 9_{\text{syst}} \pm 18_{\text{stat}}$	$54 \pm 8_{\text{syst}} \pm 17_{\text{stat}}$
	93.3	$17.9 \pm 3.5_{\text{syst}} \pm 5.7_{\text{stat}}$	$22.1 \pm 4.2_{\text{syst}} \pm 7.0_{\text{stat}}$
2	133.4	$58 \pm 9_{\text{syst}} \pm 20_{\text{stat}}$	$54 \pm 8_{\text{syst}} \pm 19_{\text{stat}}$
	93.3	$18.1 \pm 3.6_{\text{syst}} \pm 6.4_{\text{stat}}$	$22.3 \pm 4.2_{\text{syst}} \pm 7.8_{\text{stat}}$
3	120.0	$37 \pm 5_{\text{syst}} \pm 23_{\text{stat}}$	$35 \pm 5_{\text{syst}} \pm 21_{\text{stat}}$
	79.9	$9.1 \pm 1.8_{\text{syst}} \pm 5.5_{\text{stat}}$	$11.5 \pm 2.2_{\text{syst}} \pm 7.0_{\text{stat}}$

Table 5.5.: Final cross section values for $\chi = \chi_{\text{GSI}}$ and $\chi = 1$.

		$\chi = \chi_{\text{GSI}}$	$\chi = 1$
Data set	E_{CMS} (keV)	$S(E)$ (MeV nanobarn)	$S(E)$ (MeV nanobarn)
1	133.4	$4.1 \pm 0.6_{\text{syst}} \pm 1.3_{\text{stat}}$	$3.8 \pm 0.6_{\text{syst}} \pm 1.2_{\text{stat}}$
	93.3	$3.0 \pm 0.6_{\text{syst}} \pm 1.0_{\text{stat}}$	$3.7 \pm 0.7_{\text{syst}} \pm 1.2_{\text{stat}}$
2	133.4	$4.1 \pm 0.6_{\text{syst}} \pm 1.4_{\text{stat}}$	$3.8 \pm 0.6_{\text{syst}} \pm 1.3_{\text{stat}}$
	93.3	$3.1 \pm 0.6_{\text{syst}} \pm 1.1_{\text{stat}}$	$3.8 \pm 0.7_{\text{syst}} \pm 1.3_{\text{stat}}$
3	120.0	$3.3 \pm 0.5_{\text{syst}} \pm 2.0_{\text{stat}}$	$3.1 \pm 0.4_{\text{syst}} \pm 1.9_{\text{stat}}$
	79.9	$2.4 \pm 0.5_{\text{syst}} \pm 1.5_{\text{stat}}$	$3.0 \pm 0.6_{\text{syst}} \pm 1.8_{\text{stat}}$

Table 5.6.: Final S-factor values for $\chi = \chi_{\text{GSI}}$ and $\chi = 1$.

As described in the previous section, all data points are derived from a yield sum assuming a particular slope of the S-factor. As the yield at higher energy contributes

most to the yield sum and is therefore closer to this value, the higher-energy yield can be regarded as "measured", and the lower energy yield as "derived". This has been marked in all following figures by changed colors.

The error bars in figures 5.2 and 5.3 are the statistical and systematic errors added in quadrature:

$$\Delta S(E) = \sqrt{(\Delta S(E)_{\text{syst}})^2 + (\Delta S(E)_{\text{stat}})^2} \tag{5.17}$$

With these error values, the results of data sets 1 and 2, which have been obtained independently at the same beam energy, can be combined by calculating a weighted average, which reduces the errors significantly:

$$S(E) = \frac{\Delta S_1^{-2}(E)\, S_1(E) + \Delta S_2^{-2}(E)\, S_2(E)}{\Delta S_1^{-2}(E) + \Delta S_2^{-2}(E)} \tag{5.18}$$

and

$$\Delta S(E) = \frac{1}{\Delta S_1^{-2}(E) + \Delta S_2^{-2}(E)} \tag{5.19}$$

The results are, in case of $\chi = \chi_{\text{GSI}}$,

$$S(133.4\,\text{keV}) = (4.09 \pm 1.05)\,\text{MeV nb} \tag{5.20}$$

$$S(93.3\,\text{keV}) = (3.04 \pm 0.83)\,\text{MeV nb} \tag{5.21}$$

and, in case of $\chi = 1$,

$$S(133.4\,\text{keV}) = (3.79 \pm 0.98)\,\text{MeV nb} \tag{5.22}$$

$$S(93.3\,\text{keV}) = (3.75 \pm 1.01)\,\text{MeV nb} \tag{5.23}$$

For the case of $\chi = \chi_{\text{GSI}}$, the values are plotted in figure 5.4.
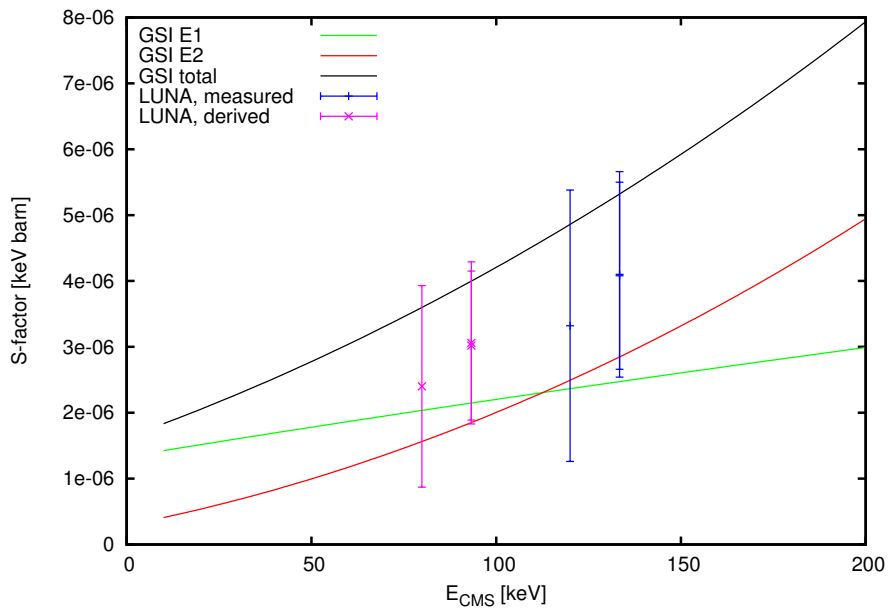
Figure 5.2.: Measured S-factor values compared to the GSI data for $\chi = \chi_{\text{GSI}}$.
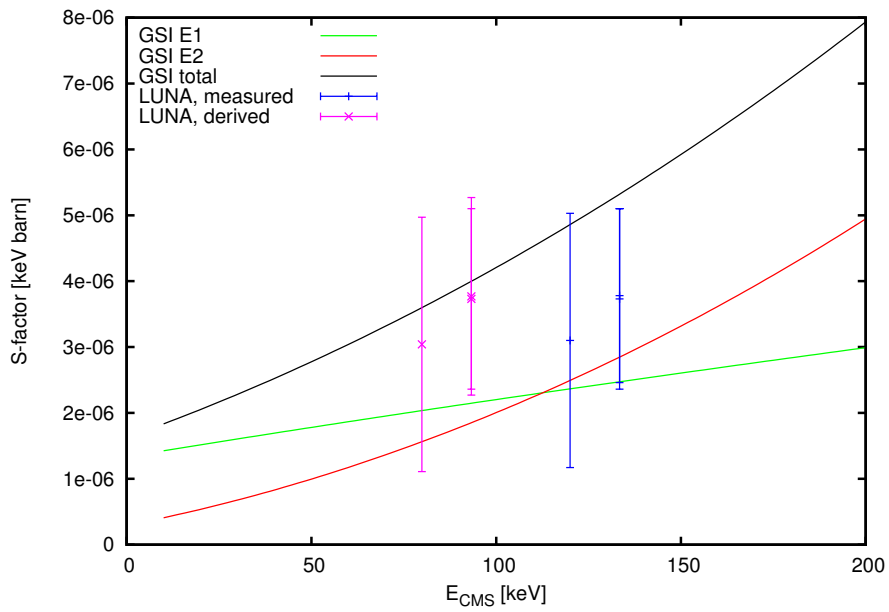
Figure 5.3.: Measured S-factor values compared to the GSI data for $\chi = 1$.
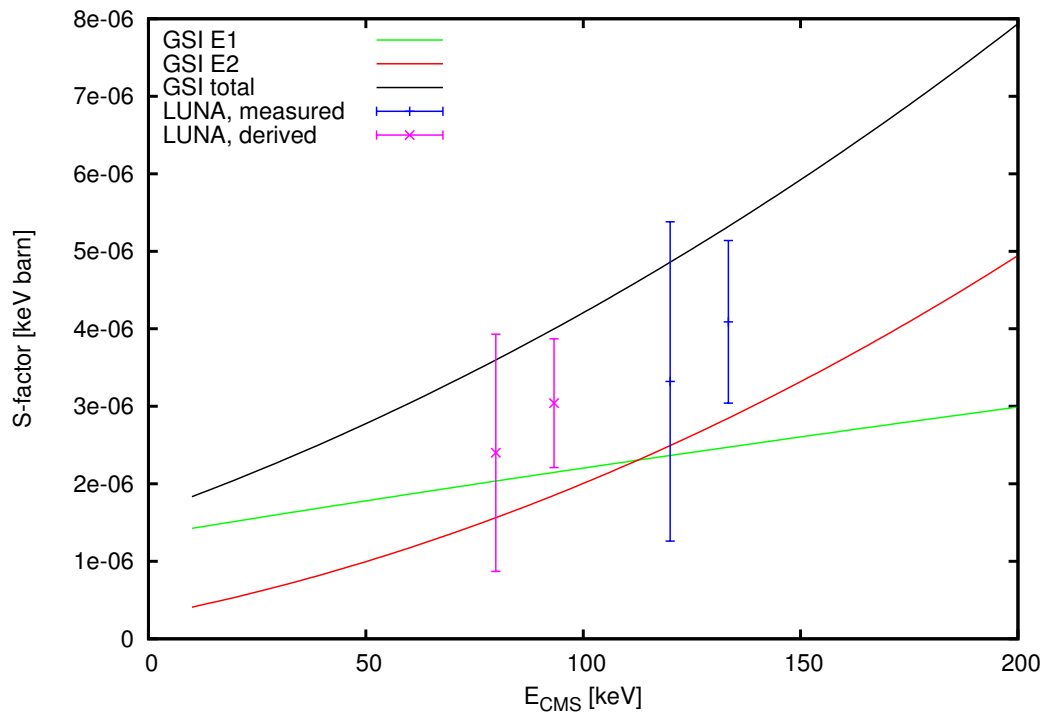
Figure 5.4.: Measured S-factor values compared to the GSI data for $\chi = \chi_{\text{GSI}}$, with combined data of the data sets 1 and 2.

6. Conclusion

6.1. The impact on Big-Bang nucleosynthesis

The data analysis yielded a positive result: For the first time ever, directly measured $^2H(\alpha,\gamma)^6Li$ cross section data are available at energies relevant for Big-Bang nucleosynthesis. The results do not place upper limits only. The data support the conclusion that by far not enough ^6Li is produced during Standard Big-Bang Nucleosynthesis to allow successful observations of primordial ^6Li abundances in metal-poor stars today. The provided total S-factors lie even below the recent GSI estimations, hence a "nuclear solution" to the ^6Li problem can be ruled out.
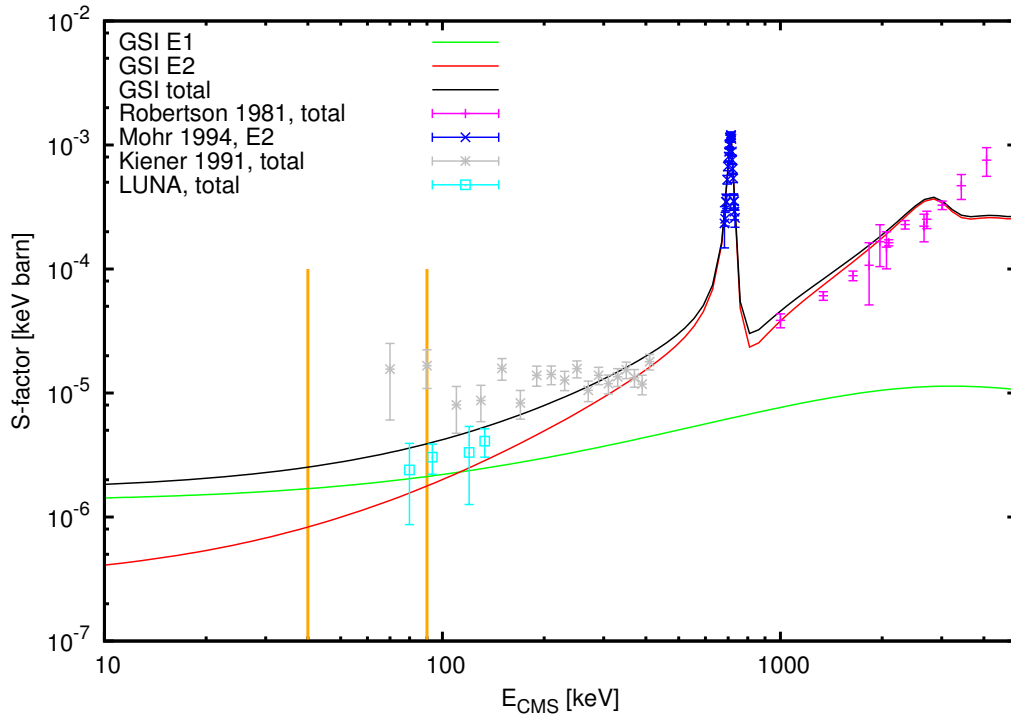
Figure 6.1.: Measured LUNA S-factor values (present data) compared to previous data [6],[16],[10],[15]. The energy range relevant for SBBN is marked by two orange lines.

The LUNA data will allow to scale and extrapolate theoretical S-factor curves to low energies with a strongly reduced uncertainty, and the error on the predicted primordial ^{6}Li abundance will decrease. As the new results are close to the theoretical curves of the GSI group, no new SBBN calculations have been carried out in this work.

The efforts to clarify whether the recent significant detections of ^{6}Li are only due to the underestimation of the lithium line asymmetry in 1D LTE atmospheric models are ongoing. If some, or at least one significant ^{6}Li detection in metal-poor stars remains, the question about its origin will emerge again. With the now well constrained SBBN production of ^{6}Li, this question can not be answered. The discussion about possible pre-galactic nucleosynthesis processes or non-standard Big-Bang nucleosynthesis including exotic scenarios could reveal exciting new insights about the early phases of our Universe and the physics behind.

6.2. Outlook

Despite the strong beam induced background, cross sections down to ten picobarns have been successfully measured at LUNA. If it turns out that more directly measured data points of the ^{2}H$(\alpha,\gamma)^6$Li S-factor at energies below the 711 keV resonance are needed, or if the angular distribution of the emitted γ-rays has to be determined to deliver the needed input for theoretical models, enhanced opportunities will be available soon.

The ^{2}H$(\alpha,\gamma)^6$Li experiment at the LUNA2 facility has suffered mainly from two obstacles that could not be overcome: The accelerator provided α-beams with a maximum energy of 400 keV, where the expected reaction rates are still very low, in the order of a few counts per hour, distributed along a broad γ-energy range. Furthermore, the gas target pressure could not be increased anymore due to the restrictions on the neutron rate. For the same reason, the duration of the measurement was limited, although the data analysis has not become difficult due to low statistics, but due to systematic errors in the subtraction of the beam induced background.

The next generation of deep-underground accelerator facilities is upcoming: The LUNA MV project is already partly funded, and the preparation of the site at Laboratori Nazionali del Gran Sasso has just begun. In the planned design, the neutron shielding will be much more effective, and the available beam energies are more than sufficient to measure the ^{2}H$(\alpha,\gamma)^6$Li S-factor in the energy range between the highest LUNA2 energy and the 711 keV resonance or even above. A complete data set over a wide energy range would become available, with a much larger scope of neutron production.

The same is true for the planned Felsenkeller facility in Dresden, where no delicate experiments are nearby. As the beam induced background is by far dominating at

lower beam energies, also a shallow-underground facility is well suitable for such a measurement. This has been discussed already [52]. Also here measurements over a wide energy range, but obtained at the same site, are possible. At both underground facilities, gas targets are in preparation. Other proposed deep underground accelerator projects are less advanced at the time.

Unless the ^{2}H$(\alpha,\gamma)^6$Li signal can be identified without subtracting the beam induced background, possible systematic errors due to the unknown normalization factor remain, although the region of interest might be shifted to γ-energy regions where less problems due to a beam energy-dependent shape of the background arise. Careful studies of the beam induced background will be anyway necessary, if the current method (a windowless gas target with a γ-detector in close geometry) is employed. The possibility of discriminating neutron-induced events by a pulse-shape analysis is currently being investigated in Dresden. For future experiments with a strong neutron-induced background, a special γ-detector suitable for pulse-shape analysis could be desirable [53], or even the possibility to discriminate neutrons online, as fast digitizers and FPGAs are state of the art.

An interesting approach is to use gas-jet targets which could significantly reduce the neutron production by the ^{2}H$(^2$H,n$)^3$He reaction. Robertson et al. used a supersonic gas-jet target in 1981 to measure the ^{2}H$(\alpha,\gamma)^6$Li cross section [6]. In future designs, where deuteron implantation has to be expected, a system to bake out affected surfaces will be helpful, as well as the choice of materials which show a high mobility of deuterons when being heated. Mohr et al. [16] used gold-plated surfaces and observed a significant reducation of the beam-induced background. It could have been also very helpful that the setup ensured a long distance between the beam stop and the γ-detector. By these means, it can be made sure that all single runs are obtained at very similar conditions, to reduce systematic errors.

Summarized, the way to vastly improved measurements is already prepared.

A. Appendix

A.1. Contents of the ^{2}H(α,γ)^{6}Li regions of interest

Measurement	400 keV ROI	360 keV ROI	280 keV ROI	240 keV ROI	Live time (s)
400 keV, 1	5615	5965	5977	7156	854633
280 keV, 1	5071	5613	5927	7075	1028652
no beam, 1	391	527	273	271	1354724
400 keV, 2	6095	6436	6646	8088	721261
280 keV, 2	6092	6615	7166	8445	738462
no beam, 2	81	118	60	56	292186
360 keV, 3	5303	5731	5814	7046	738837
240 keV, 3	4319	4747	5037	6085	783654
no beam, 3	198	311	152	149	767376

Table A.1.: Raw number of events in the ^{2}H(α,γ)^{6}Li regions of interest.

A.2. Value tables: Flat regions

Region median (keV)	Region half width (keV)	Content $N_{400\text{keV}}$	Content $N_{280\text{keV}}$	Ratio ρ_r	Error (%)
219	11	32313	32698	1.012	0.78
435	8	16468	16966	1.030	1.09
818.5	5.5	6562	6667	1.016	1.74
1027	7	6273	6180	0.985	1.79
1190	10	7207	7331	1.017	1.66
1308	8	4945	4904	0.992	2.02
1531	11	4639	4712	1.016	2.07
1631.5	4.5	1308	1324	1.013	3.90
1838	18	3718	3571	0.961	2.34
1986	18	2328	2161	0.928	2.99
2275	15	1133	893	0.788	4.48
2465	25	1122	957	0.853	4.40

Table A.2.: Flat regions parameters and values for data set 1.

Region median (keV)	Region half width (keV)	Content $N_{400\text{keV}}$	Content $N_{280\text{keV}}$	Ratio ρ_r	Error (%)
219	11	36102	38323	1.062	0.73
435	8	18695	19717	1.055	1.02
818.5	5.5	7421	7644	1.030	1.63
1027	7	7023	7370	1.049	1.67
1190	10	8247	8497	1.030	1.55
1308	8	5430	5782	1.065	1.89
1531	11	5327	5305	0.996	1.94
1631.5	4.5	1639	1643	1.002	3.49
1838	18	4193	4275	1.020	2.17
1986	18	2660	2575	0.968	2.76
2275	15	1169	1026	0.878	4.28
2465	25	1347	1128	0.837	4.04

Table A.3.: Flat regions parameters and values for data set 2.

Region median (keV)	Region half width (keV)	Content $N_{360\text{keV}}$	Content $N_{240\text{keV}}$	Ratio ρ_r	Error (%)
219	11	32561	28168	0.865	0.81
435	8	16655	14525	0.872	1.14
818.5	5.5	6484	5727	0.883	1.81
1027	7	6019	5334	0.886	1.88
1190	10	7147	6208	0.869	1.73
1308	8	4617	4115	0.891	2.14
1531	11	4720	3977	0.843	2.15
1631.5	4.5	1382	1052	0.761	4.09
1838	18	3684	2997	0.814	2.46
1986	18	2436	1831	0.752	3.09
2275	15	1019	737	0.723	4.83
2465	25	1082	807	0.746	4.65

Table A.4.: Flat regions parameters and values for data set 3.

A.3. Yield values for different η determination methods

Data set	Beam energy (keV)	corrected		sum	
		Y_{corr} (C^{-1})	Error ΔY_{corr} (C^{-1})	Yield Y_{sum} (C^{-1})	Error ΔY_{sum} (C^{-1})
1	400	1.99	0.42	1.91	0.60
1	280	-0.08	0.43		
2	400	0.28	0.47	1.92	0.67
2	280	1.64	0.47		
3	360	0.40	0.47	1.17	0.71
3	240	0.78	0.53		

Table A.5.: The same table as table 4.21, where the normalization factor calculated with method 1 is applied.

Data set	Beam energy (keV)	corrected		sum	
		Y_{corr} (C^{-1})	Error ΔY_{corr} (C^{-1})	Yield Y_{sum} (C^{-1})	Error ΔY_{sum} (C^{-1})
1	400	1.95	0.46	2.00	0.67
1	280	0.05	0.48		
2	400	0.53	0.60	1.99	0.87
2	280	1.46	0.63		
3	360	0.57	0.74	1.26	1.18
3	240	0.69	0.92		

Table A.6.: As above, but using the normalization factor of method 2.

Data set	Beam energy (keV)	corrected		sum	
		Y_{corr} (C^{-1})	Error ΔY_{corr} (C^{-1})	Yield Y_{sum} (C^{-1})	Error ΔY_{sum} (C^{-1})
1	400	2.31	0.80	1.87	1.00
1	280	-0.44	0.60		
2	400	0.03	0.95	2.19	1.16
2	280	2.16	0.67		
3	360	-1.60	1.06	-0.99	1.31
3	240	0.61	0.78		

Table A.7.: As above, but using the normalization factor of method 3.

Bibliography

[1] D.D. Clayton. *Isotopes in the Cosmos: Hydrogen to Gallium.* Cambridge University Press, Cambridge, 2003.

[2] A. Coc et al. Standard Big-Bang Nucleosynthesis up to CNO with an improved extended Nuclear Network. *The Astrophysical Journal*, 744:158–176, 2012.

[3] F. Spite and M. Spite. Abundance of Lithium in Unevolved Halo Stars and Old Disk Stars: Interpretation and Consequences. *Astronomy and Astrophysics*, 115:357–366, 1982.

[4] M. Asplund et al. Lithium isotopic abundances in metal-poor halo stars. *The Astrophysical Journal*, 644:229–259, 2006.

[5] P.D. Serpico et al. Nuclear reaction network for primordial nucleosynthesis: a detailed analysis of rates, uncertainties and light nuclei yields. *Journal of Cosmology and Astroparticle Physics*, 12:010, 2004.

[6] R.H.G. Robertson et al. Observation of the Capture Reaction ^{2}H$(\alpha,\gamma)^6$Li and Its Role in Production of ^{6}Li in the Big Bang. *Physical Review Letters*, 47:1867–1870, 1981.

[7] B.D. Fields. The Primordial Lithium Problem. *Annual Reviews of Nuclear and Particle Science*, 61:47–68, 2011.

[8] C.E. Rolfs and W.S. Rodney. *Cauldrons in the Cosmos.* The University of Chicago Press, Chicago 60637, 1988.

[9] M. Pospelov and J. Pradler. Big Bang Nucleosynthesis as a Probe of New Physics. *Annual Review of Nuclear and Particle Science*, 60:539–568, 2010.

[10] The NACRE collaboration. The NACRE database of nuclear reaction rates for charged-particle reactions and experimental S-factors. Website, 1999. Available online at `http://pntpm3.ulb.ac.be/Nacre/nacre.htm`; visited on June 23th 2013.

[11] E. Vangioni-Flam et al. Lithium–beryllium–boron: origin and evolution. *Physics Reports*, 333:365–387, 2000.

[12] D. Mercer et al. Production of A=6,7 nuclides in the $\alpha+\alpha$ reaction and cosmic ray nucleosynthesis. *Physical Review C*, 63:065805, 2001.

[13] A.H. Wapstra et al. The Ame2003 atomic mass evaluation. *Nuclear Physics A*, 729:1–676, 2003.

[14] Brookhaven National Laboratory National Nuclear Data Center. Evaluated Nuclear Structure Data File (ENSDF). Website, 2013. Available online at `http://www.nndc.bnl.gov/ensdf/`; visited on June 26th 2013.

[15] F. Hammache et al. High-energy breakup of ^{6}Li as a tool to study the Big Bang nucleosynthesis reaction ^{2}H$(\alpha,\gamma)^6$Li. *Physical Review C*, 82:065803, 2010.

[16] P. Mohr et al. Direct capture in the 3^+ resonance of ^{2}H$(\alpha,\gamma)^6$Li. *Physical Review C*, 50:1543–1549, 1994.

[17] D.D. Clayton. *Principles of stellar evolution and nucleosynthesis*. The University of Chicago Press, Chicago 60637, 1983.

[18] K.M. Nollett et al. Six-body calculation of the α-deuteron radiative capture cross section. *Physical Review C*, 63:024003, 2001.

[19] A. Kharbach and P. Descouvemont. Microscopic study of the ^{2}H$(\alpha,\gamma)^6$Li reaction in a multicluster model. *Physical Review C*, 58:1066–1072, 1998.

[20] K.M. Nollett et al. Nuclear reaction rates and primordial ^{6}Li. *Physical Review C*, 56:1144–1151, 1997.

[21] F.E. Cecil et al. Direct capture in the 3^+ resonance of ^{2}H$(\alpha,\gamma)^6$Li. *Physical Review C*, 53:1967–1970, 1996.

[22] J. Kiener et al. Measurements of the Coulomb dissociation cross section of 156 MeV ^{6}Li projectiles at extremely low relative fragment energies of astrophysical interest. *Physical Review C*, 44:2195–2208, 1991.

[23] Yi Xu et al. NACRE II: an update and extension of the NACRE compilation of charged-particle-induced thermonuclear reaction rates for astrophysics. Website, 2010. Available online at `http://www.astro.ulb.ac.be/nacreii/`; visited on June 23th 2013.

[24] Yi Xu et al. Databases and tools for nuclear astrophysics applications - BRUSsels Nuclear LIBrary (BRUSLIB), Nuclear Astrophysics Compilation of REactions II (NACRE II) and Nuclear NETwork GENerator (NETGEN). *Astronomy and Astrophysics*, 549:A106, 2013.

114

[25] V.V. Smith et al. The ^{6}Li/ ^{7}Li ratio in the metal-poor halo dwarfs HD 19445 and HD 84937. *The Astrophysical Journal*, 408:262–276, 1993.

[26] M. Steffen et al. ^{6}Li detection in metal-poor stars: can 3D model atmospheres solve the second lithium problem? *Memorie della Società Astronomica Italiana - Supplementi*, 22:152, 2012.

[27] K. Lind et al. The lithium isotopic ratio in very metal-poor stars. *Astronomy and Astrophysics*, 554:A96, 2013.

[28] R. Cayrel et al. Line shift, line asymmetry, and the ^{6}Li/ ^{7}Li isotopic ratio determination. *Astronomy and Astrophysics*, 473:L37–L40, 2007.

[29] M. Asplund and J. Melendez. Primordial and Pre-Galactic Origins of the Lithium Isotopes. *AIP Conference Proceedings*, 990:342–346, 2008.

[30] C. Broggini et al. LUNA: Nuclear Astrophysics Deep Underground. *Annual Review of Nuclear and Particle Science*, 60:53–73, 2010.

[31] A. Formicola et al. The LUNA II 400 kV accelerator. *Nuclear Instruments and Methods in Physics Research A*, 507:609–616, 2003.

[32] C. Casella et al. A new setup for the underground study of capture reactions. *Nuclear Instruments and Methods in Physics Research A*, 489:160–169, 2002.

[33] Air Liquide. Gas Encyclopaedia: Deuterium. Website, 2009. Available online at `http://encyclopedia.airliquide.com/Encyclopedia.asp?GasID=20`; visited on March 15th 2013.

[34] J. Ziegler. SRIM - The Stopping and Range of Ions in Matter. Website, 2013. Available online at `http://www.srim.org`; visited on March 15th 2013.

[35] J.L. Osborne et al. Low-energy behavior of the ^{3}He$(\alpha,\gamma)^7$Be cross section. *Nuclear Physics A*, 419:115–132, 1984.

[36] G.F. Knoll. *Radiation Detection and Measurement - Third Edition*. John Wiley and Sons, New York, 2000.

[37] J.K. Tuli. Nuclear Data Sheets for A = 60. *Nuclear Data Sheets*, 100:347–481, 2003.

[38] G. Mukherjee and A.A. Sonzogni. Nuclear Data Sheets for A = 88. *Nuclear Data Sheets*, 105:419–556, 2005.

[39] G.Gilmore. *Practical Gamma-ray Spectrometry - Second Edition*. John Wiley and Sons, Chichester, 2008.

[40] G. Heusser. Low-radioactiviy background techniques. *Annual Review of Nuclear and Particle Science*, 45:543–590, 1995.

[41] A. Caciolli et al. Ultra-sensitive in-beam γ-ray spectroscopy for nuclear astrophysics at LUNA. *European Physical Journal A*, 39:179–186, 2009.

[42] National Institute of Standards and Technology. XCOM: Photon Cross Sections Database. Website, 2011. Available online at `http://www.nist.gov/pml/data/xcom/index.cfm`; visited on March 19th 2013.

[43] A. Rindi et al. Underground neutron flux measurement. *Nuclear Instruments and Methods in Physical Research A*, 272:871–874, 1988.

[44] M. Anders et al. Neutron-induced background by an α-beam incident on a deuterium gas target and its implications for the study of the ^{2}H(α,γ)^{6}Li reaction at LUNA. *European Physical Journal A*, 49:28, 2013.

[45] International Atomic Energy Agency. Experimental Nuclear Reaction Data (EXFOR). Website, 2013. Available online at `http://www-nds.iaea.org/exfor/exfor.htm`; visited on June 23th 2013.

[46] K. Nakamura et al. (Particle Data Group). 2010 Review of Particle Physics. *Journal of Physics G: Nuclear and Particle Physics*, 37:075021, 2010.

[47] R. Vennink and J. Kopecky. Investigation of the ^{56}Fe(n,γ)^{57}Fe and ^{58}Fe(n,γ)^{59}Fe reactions. *Nuclear Physics A*, 344:421–445, 1980.

[48] The International Commission on Radiation Units and Measurements. Fundamental Quantities and Units for Ionizing Radiation (revised). *Journal of the ICRU*, 11, 2011.

[49] C.Iliadis. *Nuclear Physics of Stars*. Wiley-VCH, Weinheim, 2007.

[50] P.J. Mohr et al. CODATA recommended values of the fundamental physical constants: 2010. *Reviews of Modern Physics*, 84:1527–1605, 2012.

[51] Gy. Gyürky et al. ^{3}He(α,γ)^{7}Be cross section at low energies. *Physical Review C*, 75:035808, 2007.

[52] D. Bemmerer. *Precise nuclear physics for the Sun (Habilitationsschrift)*. Helmholtz-Zentrum Dresden-Rossendorf, Dresden, 2011.

[53] M. Agostini et al. Signal modeling of high-purity Ge detectors with a small read-out electrode and application to neutrinoless double beta decay search in Ge-76. *Journal of Instrumentation*, 6:P03005, 2011.

Erklärungen

Hiermit versichere ich, dass ich die vorliegende Arbeit ohne unzulässige Hilfe Dritter und ohne Benutzung anderer als der angegebenen Hilfsmittel angefertigt habe. Die aus fremden Quellen direkt oder indirekt übernommenen Gedanken sind als solche kenntlich gemacht. Die Arbeit wurde bisher weder im Inland noch im Ausland in gleicher oder ähnlicher Form einer anderen Prüfungsbehörde vorgelegt.

Michael Anders
Dresden, 28. Juni 2013

Diese Dissertation wurde im Zeitraum zwischen Dezember 2009 bis zum Juni 2013 am Institut für Kern- und Teilchenphysik der Technischen Universität Dresden unter der Betreuung von Prof. Dr. Kai Zuber sowie am Institut für Strahlenphysik des Helmholtz-Zentrums Dresden-Rossendorf unter der Betreuung von PD Dr. Daniel Bemmerer angefertigt.

Ich erkenne die Promotionsordnung der Fakultät Mathematik und Naturwissenschaften der Technischen Universität Dresden in der Fassung vom 23.02.2011 an.

Michael Anders
Dresden, 28. Juni 2013